FACULTY OF MATHEMATICS AND PHYSICS
CHARLES UNIVERSITY IN PRAGUE

CHAOS IN THERMAL CONVECTION AND THE WAVELET ANALYSIS OF GEOPHYSICAL FIELDS

PH.D. THESIS

LUDĚK VECSEY

PRAGUE 2002

Supervisor: Doc. RNDr. Ctirad Matyska, DrSc.

Consultant: Prof. Dr. David A. Yuen

Author's address: Department of Geophysics
Faculty of Mathematics and Physics
Charles University
V Holešovičkách 2
180 00 Praha 8 – Libeň
Czech Republic

e-mail: vecsey@karel.troja.mff.cuni.cz

V zajetí termálních vět
brní a vrní se hlavy
plumí
poslední Newtonův květ vyroste
na podzim spletené barvy
ztlumí
znavená Země v závitech sténá
do vlnek obléct ji
ať si jde
tiše já zapomněl že existuje
asi i normální svět

Té, která odsunula madam Fyziku
až na druhé místo ...

Lence

Contents

1 Introduction **1**

1.1 Wavelet transform 1

1.2 Thermal convection 2

1.3 Scope of this thesis 3

1.4 Acknowledgments 4

2 Continuous wavelet transform **7**

2.1 Introduction 7

2.2 Continuous wavelet transform 8

2.3 Kinds of wavelets 12

2.4 Morlet wavelet, Gaussian wavelets 13

2.5 Scalograms 16

2.6 $E_{\max}$ and $k_{\max}$ 17

2.7 What next? 20

3 Thermal Convection & Chaos **21**

3.1 Introduction 21

3.2 Governing equations 22

3.2.1 The conservation laws and boundary conditions 22

3.2.2 Boussinesq approximation 23

3.2.3 Nondimensionalization 24

3.2.4 Axisymmetrical shell geometry 25

3.3 Computational aspects 28

3.4 Deterministic chaos 30

3.4.1 What is chaos? 30

3.4.2 Routes to chaos . . . 31
3.4.3 The attractor dimension . . . 33
3.5 Thermal convection for different Rayleigh numbers . . . 37
3.5.1 Low Rayleigh number convection . . . 37
3.5.2 Intermediate Rayleigh number convection . . . 46
3.5.3 High Rayleigh number convection . . . 50
3.5.4 Ultra-high Rayleigh number convection . . . 54
3.5.5 Whitehead instabilities . . . 57
3.5.6 Vertical temperature profiles for high Rayleigh numbers . . . 59
3.5.7 Power laws for the kinetic energy and the Nusselt number . . . 60
3.6 Discussion & concluding remarks . . . 62

4 Results of Wavelet Analysis **67**
4.1 Geoid . . . 68
4.1.1 Introduction . . . 68
4.1.2 The wavelet featured geoid . . . 68
4.1.3 The $E_{\max}$-$k_{\max}$ maps . . . 69
4.1.4 Advantages of wavelets over spherical harmonics . . . 70
4.1.5 Regional studies . . . 70
4.1.6 Discussion and concluding remarks . . . 73
4.2 Mixing . . . 81
4.2.1 Introduction . . . 81
4.2.2 Wavelet transform of the mixed field . . . 82
4.2.3 Results of the wavelet transform for the mixed field . . . 83
4.2.4 Discussion and concluding remarks . . . 94
4.3 Spherical shell convection wavelet analysis . . . 95
4.3.1 Introduction . . . 95
4.3.2 Convection for $Ra = 10^6$ . . . 95
4.3.3 Convection for $Ra = 10^7$ . . . 96
4.3.4 Convection for $Ra = 10^8$ . . . 96
4.3.5 Convection for $Ra = 10^{10}$ . . . 97
4.3.6 Convection for $Ra = 10^{11}$ . . . 97

4.3.7 Discussion and concluding remarks 98

5 Conclusions **107**

5.1 Thermal convection modelling 107

5.2 The power of wavelet analysis 109

References **111**

Summary

This thesis consists of two major parts: the examination of the power of the continuous wavelet transform (CWT) followed by its application to geophysical fields and the modelling of convection in the Earth's mantle with main focus on the nonlinear behavior of the system.

The wavelet theory arose from the need of a good time-frequency representation of a signal, or a field. As there exist a number of different wavelets which could be, in principle, employed, we discuss properties of the CWT for a particular choice of the wavelet function. The Morlet wavelet used in the 1-D wavelet transform is found satisfactory for the time-frequency analysis of long signals, and the Mexican-hat wavelet used in the isotropic 2-D wavelet transform works well for finding structures of different scales in an analyzed field. The new method of $E_{\max}/k_{\max}$ maps (Bergeron et al., 1999) is applied to increase the detection ability of the wavelets at small-scales.

The power of the 2-D wavelet transform is demonstrated by analysizing the non-hydrostatic geoid in the Mercator projection with a resolution of 4 degrees. The small-scale wavelet spectrum of the geoid reveals features created by lithospheric processes. The strongest signal originates from subduction zones (e.g., the "Ring of Fire"), and weaker signals are detected along several mountain belts (the Himalayas, the Andes, and the Atlas Mts.), oceanic rifts (the Mid-Atlantic Ridge), and hotspots (Hawaii). The wavelet analysis of the second field, the mixed medium, helps to monitor the mixing progress. We can take advantage of the sensitivity of the isotropic wavelet transform to unmixed anisotropic structures in the field to detect the degree of the mixing. The last case to which we applied the 2-D CWT is the temperature and vorticity fields from our thermal convection model. Here the wavelets prove their ability for both small-scale and large-scale detection. Small-scale wavelet analysis of the temperature reveals the complex structure of plumes in the ultra-high Ra convection as well as helps to find areas with numerical instabilities. Large-scale analysis of the vorticity determines the number of convection cells.

The second part of the thesis contains numerical studies of the nonlinear system of thermal convection in the classical Boussinesq approximation for infinite Prandtl number and axisymmetrical geometry. Complexity of the behavior of the nonlinear system results in different convection regimes dependending on the Rayleigh number (Ra), which was the only control parameter in the model. We classified the convection systems for Rayleigh numbers between $Ra = 1.7 \cdot 10^4 - 10^{11}$ into four basic regimes. The low Rayleigh number convection (for Ra varying from $1.7 \cdot 10^4$ to 10^5) reaches simple attractors (steady or periodic ones) of a two-cell structure. Intermediate Ra convection ($Ra = 10^5 - 10^6$) still has a two-cell structure, but secondary plumes begin to appear. The correlation dimension for $Ra = 10^5$ reveals the complex temporal evolution of the system. High Ra runs with Ra between 10^6 and 10^{10} exhibit complex structure with waning large-scale motion and prevailing plume-plume interactions. Secondary (Whitehead) instabilities occur. Finally, ultra-high Ra convection ($Ra \geq 10^{10}$) has a very turbulent behavior with powerful mixing; no whole-mantle plumes exist.

In the convection part of the thesis we depict the main characteristics of basic thermal convection regimes as they move from a calm, steady state to turbulent chaos with increasing Ra. These characteristics can help to substantially unify convection modelling with other fields of geodynamics. There is no doubt that without the excellent wavelet transform tool the analysis of convection systems (and many other geophysical fields) could not be satisfactorily completed.

Chapter 1

Introduction

Theoretical geodynamicists cannot survive today only with their brain, paper and pencil but they also need to use helpful abilities of the computer world, either for creating and solving corresponding equations or for visualizing physically measured fields or computed results. Our work consists of two major parts: the first one is the examination of the power of a mathematical tool - the wavelet transform - which allows us to decompose and view geophysical signals over different length scales, and the second part consists of modelling convection in the Earth's mantle. In the second part we use tools helpful to understanding the nonlinear behavior of the system, such as wavelet analysis and analytical tools of deterministic chaos.

We would like to mention that each chapter has its own introduction and conclusions since we deal with related but clearly distinct topics. Therefore, we focus only on the main ideas in this chapter to provide a brief overview of the studied problems.

1.1 Wavelet transform

The wavelet theory arose from the need for a good time-frequency representation of a signal, or field. Conventional transforms, such as the standard Fourier transform or the windowed Fourier transform, do not suit the requirement for a fast but precise and easy-to-use tool for decomposition of signals or fields into different frequency components, which are well localized in time (or space). The idea of filtering the signal with a wavelet basis (called the mother wavelet) which is translated in space together with dilation or contraction to achieve the desired frequency resolution was invented independently in pure mathematics, physics and engineering during 1960-80's (for references see, e.g., Daubechies, 1992, p. 1).

In the past few years, wavelet analysis has emerged as a very powerful tool in various applications, such as signal processing, image coding, detection of coherent structures, data filtering and reconstruction of a signal. In geophysics, we can mention seismic data analysis (Morlet, 1983), coherent structures in turbulent flows (Farge, 1992), the dispersion of ocean waves (Meyers et al., 1993), thermal convection modelling (Vecsey and Matyska, 2001), detection of structures in seismic tomography (Bergeron et al., 1999, 2000a, 2000b), wavelet cross-spectra of seismic tomography (Piromallo et al., 2001), etc. The wavelet analysis itself is based on the mathematical theory of

frames and can be split into two major types (e.g., Daubechies, 1992; Farge, 1992): the continuous wavelet transform and the discrete wavelet transform (which can be further distinguished between redundant discrete systems (frames) and orthonormal bases of wavelets). In this thesis, we consider only the continuous wavelet transform, which is better suited for analyzis as it is able to find the wavelet spectrum in arbitrary a time-frequency location and thus enables better graphical visualization of the energy distribution. Moreover, it offers a large degree of freedom in the choice of the wavelet basis, with properties suited for an individual analysis.

As there is a number of different wavelets which could be, in principle, employed, the question arises what are the reasons for a particular choice of the wavelet function. This is discussed in detail in Farge (1992) and Torrence and Compo (1998). We can only remark that one should consider the character of the signal (periodic or discontinuous) and aspects of the signal which should be retrieved. The wavelets properties - such as complex or real, even or odd characters of the function, wavelet width and shape, and vanishing moments (regularity) - then determine the kind of information which will be preferentially extracted from the signal.

It is very natural to extend the 1-D wavelet analysis into a 2-D or more dimensions. The wavelet bases are created by translation, dilation and rotation of the original wavelet (Farge, 1992; Antoine et al., 1993). Unfortunately, analysis of an N-dimensional system leads to $2N$-dimensional wavelet power spectrum. Although the fast Fourier transform routine is usually employed for fast computations of the continuous wavelet transform, the computations themselves still have large computer memory requirements. To reduce the computational requirements, the anisotropy of the structures in the signal is often omitted and an isotropic wavelet transform, which reduces the number of wavelet spectrum dimensions to $N + 1$, is considered. In such a case the wavelets are enhanced by the peripheral vision ability.

Visualization problems occur with multidimensional wavelet analysis. Graphical visualization of high-dimensional wavelet spectra is needed to easily detect the appropriate structures. The usual techniques which include low-dimensional cuts of the scalograms or animations are complemented by advanced methods which help to detect meaningful structures in a field. The readability of the time-frequency representation can be improved by the reassignment method (Auger and Flandrin, 1995), and detection of the structures can be aided with the help of low-dimensional maps (Bergeron et al., 1999).

The wavelet transform is still evolving. Wavelet constructions on a sphere have been developed (Holschneider, 1996; Antoine and Vandergheynst, 1998), and wavelet-based methods (cross-correlation or similarity of the wavelet spectra) allow enhanced comparison of two signals.

1.2 Thermal convection

There has been great progress in understanding mantle processes during the last 20 years. New developments in mineral physics, seismic tomography, geochemistry and increasing computer power have led to better and more complex models of the dynamics of the Earth's interior. The advection of heat is one of the fundamental modes of heat transfer in the Earth, and thus is important to the both thermal history of the Earth and Earth's mantle dynamics.

Modelling the thermal convection in the mantle relies on the accuracy of knowledge of pa-

rameters in the Earth interior. Models can be validate qualitatively (or even quantitatively) by the agreement between the output of the numerical model and the physically measured data (e.g. seismic tomography or mineral physics). A fundamental question is the applicability of the model output to present-time data observed on the Earth's surface or determined from seismic tomography. For the most part we only have present-day 'snapshots' of Earth's state. Looking at the partial differential equations describing thermal convection we see that, even in the most simple approximation, the dynamical system is nonlinear (since the nonlinear advection of heat must be considered).

It is well known (e.g., Nese, 1987; Drazin, 1992; Marek and Schreiber, 1991) that nonlinear systems can yield different regimes varying from stationary states to periodic behavior of solutions and, finally, to chaotic states. When the chaoticity is strong, a comparison between the numerical model and the present-day measured data cannot be made. In such a case a tool for quantifying chaos is needed, in orders to substantially unify convection modelling with other fields of geodynamics. One possibile way how to quantify chaoticity is to evaluate the dimension of the attractor. Fractal dimension for 2-D convection in Cartesian geometry was estimated, e.g., by Vincent and Yuen (1989), for measured data and for higher dimensional systems the correlation dimension is more suitable (e.g., Nese, 1987).

When the control parameters of the convection system are changed, sudden jumps (so-called bifurcations) of the system regimes can occur. To reveal the internal dynamics of the convection system in a given regime, the advanced technique of the wavelet transform can be used to recognize behavior of the system at different scales. We used the 1-D wavelet transform to investigate the time-evolution of time-series of global and semi-global quantities, such as the Nusselt number, which measures the efficiency of the heat flow through the surface, or the kinetic energy. To recognize and understand the structure of temperature and vorticity fields, the 2-D wavelet transform was employed.

There is no doubt that there are other nonlinearities in the real Earth, which influence the behavior of the convection system. We can mention, for example, the temperature and pressure dependence of viscosity (Karato, 1993) and thermal conductivity (Hofmeister, 1999), the stress dependence of viscosity (Van den Berg et al., 1993), the radiation of heat (Matyska et al., 1994), dissipation and adiabatic heating or cooling (Hansen et al., 1993; Velímský and Matyska, 2000). It is not the purpose of this thesis to cover all aspects of the real Earth mantle convection in our model, on the contrary, we adopted only a simple model of an incompressible fluid for the classical Boussinesq approximation in a 2-D spherical shell heated from bellow (Moser, 1994) to depict the main characteristics of basic regimes along the route of the thermal convection from a calm, steady state to turbulent chaos.

1.3 Scope of this thesis

This thesis is divided into five chapters. The introduction in Chapter 1 is followed by the presentation of the fundamental ideas of the wavelet transform in Chapter 2. Chapter 3 deals with thermal convection modelling; in Chapter 4 the wavelet analysis of 2-D images from three different geophysical fields is demonstrated. The thesis finishes with the conclusions presented in Chapter 5.

In Chapter 2, we introduce the continuous wavelet transform (CWT) to the reader. We start

with the definition of the CWT and methods enabling its easy computation, followed by a discussion of the criteria for a suitable choice of the wavelet basis. We continue with a presentation of the two mother wavelets used in this thesis, the Morlet wavelet for the time-frequency analysis of a 1-D time-series and the Mexican-hat wavelet for detecting structures of different scales in 2-D geophysical images. Methods of visualization of the results of the wavelet analysis are discussed in the second part of the chapter. We point to problems with visualization of large grid size datasets and their wavelet spectra. Several solutions are presented, especially the new method of $E_{\max}/k_{\max}$ maps for enhancing the readability of high-dimensional CWT data. We finish the wavelet chapter with an outline of methods for future progress.

Thermal convection for different Rayleigh numbers (Ra) is analyzed in Chapter 3. First, we discuss basic assumptions and equations, which lead to the nondimensional model of the thermal convection in the classical Boussinesq approximation. To compute this model, we adopted code developed by Moser (1994). The computational aspects and our strategy used during mapping the convection for different Rayleigh numbers closes the first theoretical part in Chapter 3. In the second theoretical part, various aspects of deterministic chaos studies are introduced. We present several routes to chaos under changes of the controlling parameter Ra; the correlation dimension of the attractor, which is the quantity characterizing the chaoticity of the system, is chosen to help with classification of convection regimes for different Rayleigh numbers.

The second half of Chapter 3 is devoted to the examination of different regimes of thermal convection with the help of the correlation dimension and 1-D wavelet analysis of time-series. As there exists qualitative changes in the styles of convection, we divided the computed runs into four sections: low, intermediate, high and ultra-high Ra convection. The character of each group is explored with different tools: the correlation dimension and 1-D wavelet analysis are suitable for long time-series, and thus also for low and intermediate Ra numbers, higher Ra runs and their complicated spatial structure with evolution and collisions of the plumes are investigated in several time snapshots of the related temperature fields. The chapter finalizes the convection regime research by finding features common for either wide range of Rayleigh numbers (such as Whitehead instabilities) or by relationships valid for all Rayleigh numbers (such as power laws of the kinetic energy or the Nusselt number).

Chapter 4 exhibits the power of 2-D wavelet analysis applied to the three geophysical fields: the geoid, mixing, and thermal convection. Each problem requires specific detection tasks of the wavelet. The geoid field hides small-scale structures, which can be distinctly revealed by the CWT; the mixed medium contains anisotropic unmixed formations to which the continuous wavelet analysis is very sensitive. Finally, the vorticity images obtained from the high Rayleigh number thermal convection hide large-scale motion related to different convection regimes.

1.4 Acknowledgments

I greatfully thank Prof. Dr. David A. Yuen for his broad help, amazing enthusiasm with which he dragged me into the wavelet kingdom, for his neverending interest in my work and for a lot of references to brand-new topics in geophysics. I am indebted to him for providing me with the facilities at the Minnesota Supercomputing Institute, University of Minnesota, especially for computing time on the IBM SP Supercomputers, and for support during my stays in Minnesota.

And I must not forget to thank him my second name, "Luke".

I also wish to thank Catherine ("Cathy") Hier Majumder for helping me to assimilate in the U.S.A., for her assistance during the writing of my thesis and her English language 'debugging' of the work. No less thanks belongs to Dr. Stephen Y. Bergeron, Erik O. Sevre, Arkady A. Ten and also to all the people from the Professor David Yuen's research group for supporting me in different ways, and also for the friendly environment during my stays at the Minnesota Supercomputing Institute. I would like to acknowledge the hospitality and support provided by Prof. Alain Vincent during my visit to the University of Montreal.

I thank Doc. RNDr. Ctirad Matyska, DrSc., very much for his valuable suggestions, constructive comments, and English corrections. I would like to express my appreciation to RNDr. Jaroslava Plomerová, DrSc., for her understanding during my thesis writing, and RNDr. Vladislav Babuška, DrSc., for his comments, constructive discussions, and for polishing my English in several parts of the thesis.

I am greatful to my family and all my friends for keeping my morale up, and I apologize for neglecting them during my thesis writing ...

Chapter 2

Continuous wavelet transform

2.1 Introduction

We often need to localize variations of power within geophysical data files such as time-series, temperature fields, or geoid anomalies. The most common tool used in geophysics for signal analysis is the Fourier transform (FT), e.g., Cartwright (1990). The FT only provides information about global behavior and is only suitable for signals that vary periodically without any sudden or unpredictable changes (Hubbard, 1998).

The windowed Fourier transform (WFT) provides a method for extracting local frequency information from a signal. However, the WFT is inaccurate for aliasing high- and low-frequency components that do not fall within the range of the window (Torrence and Compo, 1998; Kaiser, 1994), see Figure 2.2. Other large groups of time-frequency representations of non-stationary signals has been proposed among the Cohen's class (Cohen, 1966) of bilinear time-frequency energy distributions, such as the Wigner-Ville distribution (Wigner, 1932), the Margenau-Hill distribution (Margenau and Hill, 1961), their smoothed versions and many others with reduced cross terms. These approaches and their theoretical properties can be found, e.g., in Claasen and Mecklenbräuker (1980) or Cohen (1989).

A relatively new and powerful technique for signal processing which overcomes the main problems with the FT and WFT is the wavelet transform (WT). Jean Morlet and Alex Grossman are credited with the development of the wavelet transform (Hubbard, 1998). In 1975 Morlet was working for the French oil company Elf-Aquitaine on using the WFT to analyze seismic reflection data. Morlet developed a multiresolution technique in which he took a wave pulse with a number of oscillations (Hubbard, 1998). This pulse became known as a 'wavelet'. His technique begins with a wavelet formed by a pulse of low frequency oscillations. This is compared to the signal to obtain an overall picture of the signal at coarse resolution. Then the wavelet is compressed so that the pulse still contains the same number of oscillations, but the oscillations are now at a higher frequency (pressing or dilation of the wavelet pulse see in Figure 2.1). As the wavelet is compressed, one can examine the signal at higher resolutions to look at finer details. In the early 1980's Morlet and Alex Grossman, a quantum mechanicist in Marseille, developed the WT, which allows one to transform the signal into a wavelet representation as well as the backward reconstruction of the original signal (Hubbard, 1998).

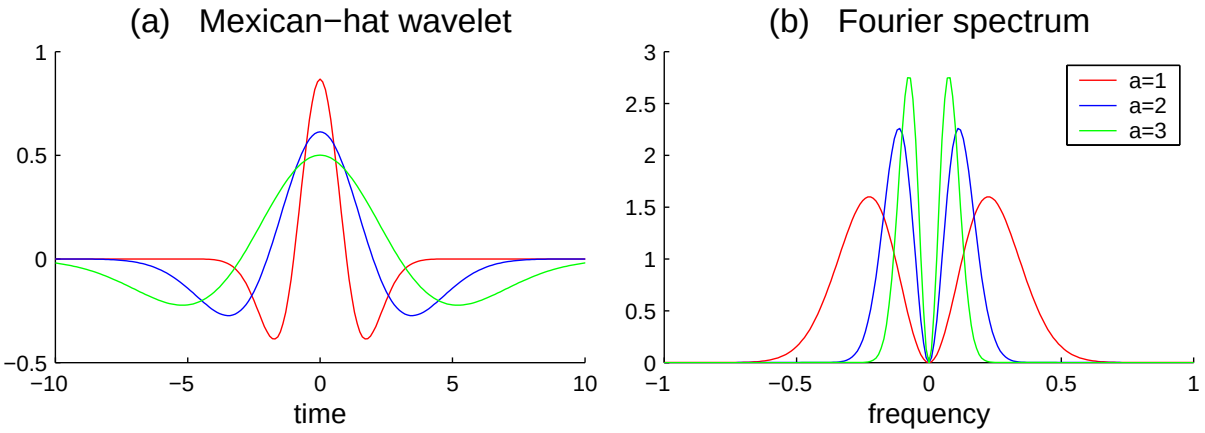

Figure 2.1. The wavelet pulse for three different scales a. (a) All pulses have unit L_2-norm. (b) Only real parts of the Fourier spectra of the Mexican-hat pulses are nonzero (see Figure 2.5). The better time resolution (a) of the wavelet, the worse its frequency resolution (b), and vice-versa.

2.2 Continuous wavelet transform

There are two wavelet transforms, the continuous wavelet transform (CWT) and the discrete wavelet transform (DWT) (Daubechies, 1992). We used the CWT which requires more computation time. However, it analyzes the signal at all possible resolutions so that one can examine any scale. The DWT only allows analysis for a discrete number of scales.

The CWT, $\Psi_{\mathrm{f}}(a,b)$, for a 1-D signal $f(t)$ is a filter of the signal with a wavelet function ψ_{o} which is shifted in time by a shift b and dilated by a scale a:

$$\Psi_{\mathrm{f}}(a,b) = a^{-\frac{1}{2}} \int_{-\infty}^{+\infty} f(t)\psi_{\mathrm{o}}^{*}\left(\frac{t-b}{a}\right) dt\,, \tag{2.1}$$

where ψ_{o}^{*} is the conjugation of the complex function ψ_{o}.
The wavelet transform (2.1) can be rewritten in the Fourier space ($\hat{f}(\omega)$ means the FT of $f(t)$):

$$\hat{\Psi}_{\mathrm{f}}(a,\omega) = a^{\frac{1}{2}}\hat{f}(\omega)\hat{\psi}_{\mathrm{o}}^{*}(a\omega)\,. \tag{2.2}$$

Therefore, the fast Fourier transform (FFT) is a very efficient way of computing (2.1).

The wavelet function ψ_{o} must be well-localized in both physical and Fourier space and should satisfy the 'wave' condition which results from the admissibility condition (Daubechies, 1992):

$$\int_{-\infty}^{+\infty} \psi_{\mathrm{o}}(\eta)d\eta = 0\,. \tag{2.3}$$

The consequence of the admissibility condition is that the wavelet transform is not affected by the mean of the analysed function. Moreover, because the wavelet 'support' is compact (we consider

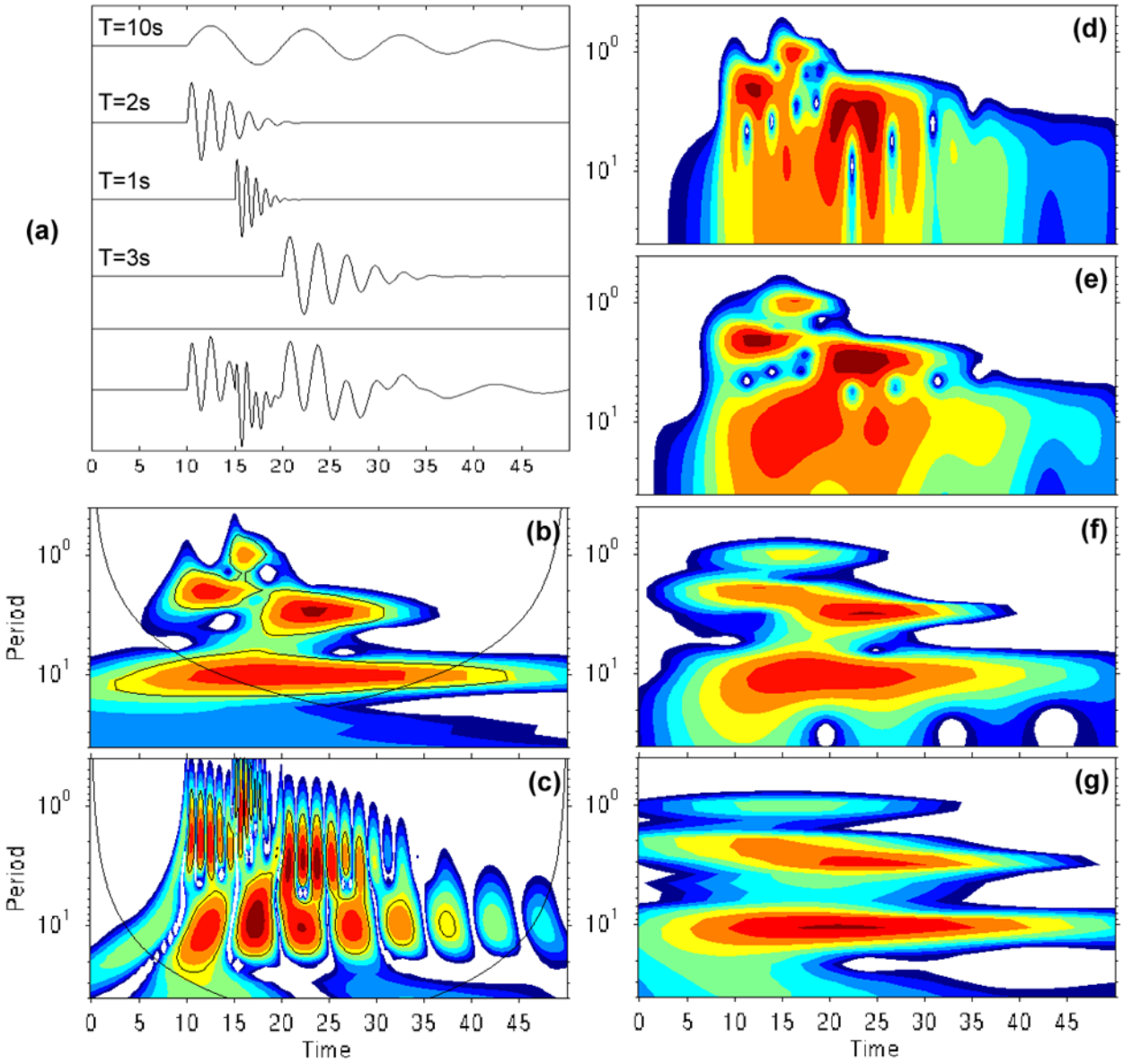

Figure 2.2. Comparison of the scalograms from the wavelet transforms (b)-(c) and the windowed Fourier transform (d)-(g). (a) Analytical signal composed from the damped sine waves of four different periods was used. (b) Morlet wavelet (2.9) embodies fine frequency resolution but worse temporal one, (c) real Mexican-hat wavelet ((2.11) for $m = 2$) is able to detect all the sinus peaks but with a certain frequency uncertainty. (d)-(g) Windowed Fourier transforms with the Gabor window $\exp(-\frac{1}{2}\left(\frac{t}{\sigma}\right)^2)$, window widths $\sigma = 1, 2, 5, 10$ used in scalograms (d)-(g), respectively. The resolution of the Morlet-like windowed Fourier transform depends on the width of its window. The colorscales in the scalograms (b)-(g) go from white (minimum), blue, green and yellow to red (maximum). The wavelet scalograms (b)-(c) include cone-of-influence lines, below which the spectra are dubious due to edge effects, and 95% significance levels which bound the peaks of significant wavelet powers. Description of the method used for computation of the cone-of-influence and significance levels is given in Torrence and Compo, 1998.

'support' here as a range of values for which the wavelet function is not negligible), the wavelet transform yields information about variations over this area, without any influence from the global trend of the filtered function.

To ensure that the wavelet transforms (2.1) at different scales a are directly comparable to each other and to the transforms of other time-series, the wavelet function at each scale a is normalized to have unit energy. Then the second condition on the wavelet function ψ_0 is:

$$\int_{-\infty}^{+\infty} |\psi_0(\eta)|^2 d\eta = 1\,. \tag{2.4}$$

One of the CWT's advantages is that the relationship between Fourier frequency and wavelet scale is known. Since we know the wavelet function ψ_0 analytically, we can simply substitute an exponential wave $\exp(i\omega_T t)$ of known period T for the signal $f(t)$ in (2.1) (it is the same as the substitution of the delta-function $2\pi\delta(\omega - \omega_T)$ for the $\hat{f}(\omega)$ in (2.2)) to find the scale a that maximizes the amplitude power of the magnitude of the wavelet spectrum Ψ_f; the scale a is given by the condition:

$$\left[|\hat{\psi_0}(\omega)| + 2\omega \frac{\partial|\hat{\psi_0}(\omega)|}{\partial\omega}\right]_{\omega=a\omega_T} = 0\,. \tag{2.5}$$

The relationship between Fourier period T and corresponding wavelet scale a is always linear, the only quantity which depends on the kind of the wavelet is the coefficient of the linearity.

The CWT can be generalized for multidimensional signals. In a 2-D CWT, the analyzing wavelet is translated by $\boldsymbol{b}$, dilated by a and rotated by an angle θ (e.g., Antoine et al., 1993). To reduce the number of parameters, we set $\theta = 0$. This is referred to as an isotropic 2-D CWT. We use a 2-D isotropic CWT of the signal $f(\boldsymbol{x})$ on a periodic box of size $L_x \times L_y$ in Cartesian space (Bergeron et al., 2000b):

$$\Psi_f(a, \boldsymbol{b}) = a^{-1} \int_0^{L_x}\int_0^{L_y} f(\boldsymbol{x})\psi_0^*\left(\frac{\boldsymbol{x}-\boldsymbol{b}}{a}\right) d^2\boldsymbol{x}\,. \tag{2.6}$$

The Fourier transform is:

$$\hat{\Psi}_f(a, \boldsymbol{k}) = a\hat{f}(\boldsymbol{k})\hat{\psi_0^*}(a\boldsymbol{k})\,, \tag{2.7}$$

where $\boldsymbol{k}$ is the Fourier wavenumber. As with the 1-D CWT, computation is realized with the help of the FFT.

The use of the isotropic CWT reduces the number of parameters that need to be analyzed from four (a, b_x, b_y, θ) to three (a, b_x, b_y). This reduces the amount of computation required and makes the visualization of the results simpler. The disadvantage is that we lose information about the anisotropic nature of structures.

The problem caused by periodic extension of the analyzed signal during the FFT procedure can be solved in different ways. The wavelet spectra close to the edges of the signal are distorted (see large-scale spectrum in Figure 2.3b); one possibility is to not use them, we only consider the area where the wavelet spectrum is not influenced by the periodic extension (see the cone-of-influence lines in the scalograms in Figures 2.2b-c, 2.4; everything below these lines is dubious). We often need information from the edge areas; moreover, these distorted areas are large in case of large-scale wavelet analysis. In such cases we add zero layers around the signal, together with subtracting of the mean from the signal over the analyzed area. (Note that although the wavelets are local bases and any subtraction of the mean is not needed, the edge effects change this condition). Nevertheless even zero layering does not solve all the edge problems.

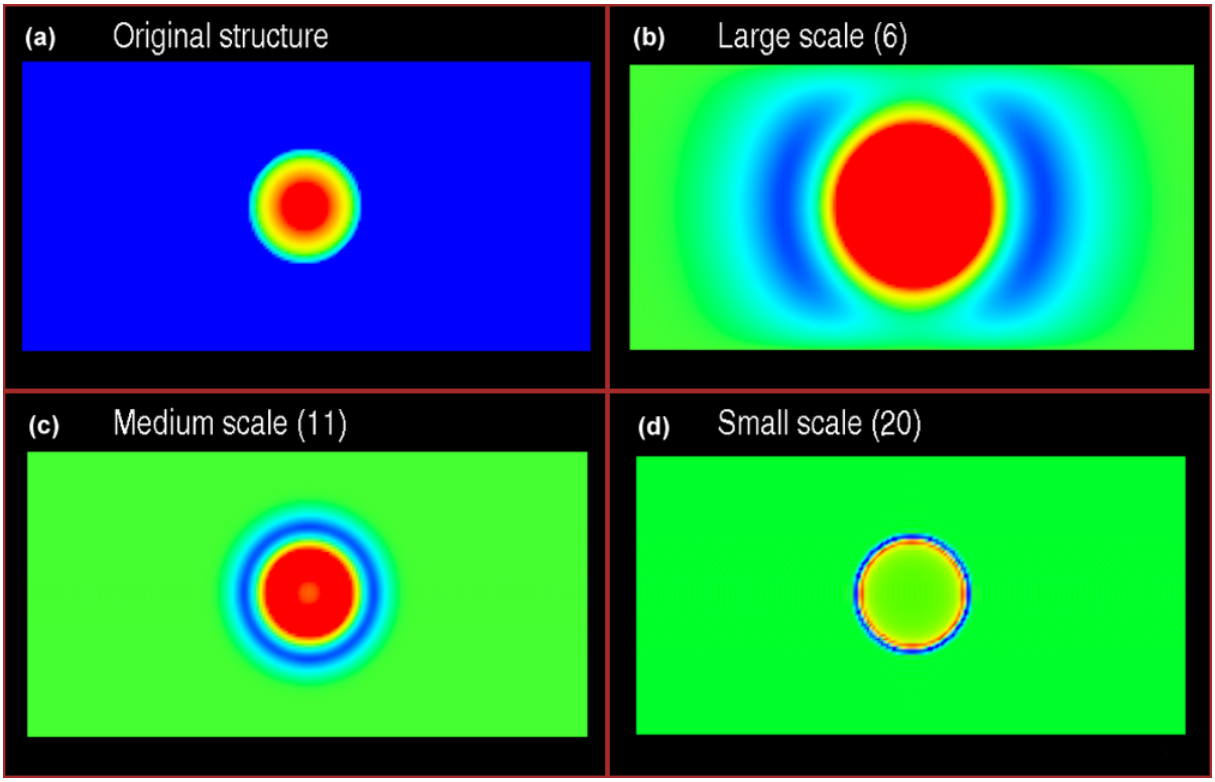

Figure 2.3. Example of the 2-D continuous wavelet transform. (a) Half-sphere $x^2+y^2+z^2=1$, $z \geq 0$ was analyzed. Colorscales change from blue ($z=0$) to red ($z=1$). The 2-D Mexican-hat wavelet (2.14) was used, scalograms at three different scales are shown in panels (b)-(d). The numbers in parenthesis are wavelet modes, corresponding resolutions of the wavelets are given in Table 4.1, page 67. Colorscales in the scalograms go from blue (minimum) to green (zero) and red (maximum). (b) Wavelet 'support' bigger than the size of the sphere. The effect of the edges occurs (see blue minima). (c) Wavelet 'support' smaller than the sphere. The Mexican hat detects shape of the sphere, as the wavelet is even, the sphere's edge is situated between blue and yellow rings. (d) Wavelet 'support' much smaller than the sphere. The local nature of the wavelets together with the first vanishing moment of the Mexican-hat wavelet cause very weak signal inside the sphere.

2.3 Kinds of wavelets

A suitable wavelet function ψ_0 can be chosen from the wide wavelet family. Aspects which should be considered are the structure of the signal to be analyzed, i.e. periodic or discontinuous, and the aspects of the signal which one wants to focus on. There is a wide variety of factors to consider (see, e.g., Torrence and Compo, 1998; Van den Berg, 1999; Hubbard, 1998):

Orthogonality or nonorthogonality. Orthogonal wavelet functions, also called orthogonal wavelet bases, use a DWT and are more appropriate for data compression and signal reconstruction. Nonorthogonal wavelet functions use a CWT and are better suited for feature detection in signals.

Complex or real. A complex wavelet function gives us information about both amplitude and phase and is well suited for oscillating signals. A real wavelet function returns only information about the amplitude of the signal and is better suited for capturing discontinuities or peaks (compare Figures 2.2b-c).

Width. There is a relationship between the width of the wavelet function in real space and the width in Fourier space (Heisenberg-Gabor inequality). A wavelet function that is narrow in real space is broad in spectral space. It has better space resolution and worse frequency resolution (see comparison of the wavelet bases in Figure 2.5).

Shape. The wavelet function's shape should be similar to the features of the signal one wishes to analyze. To detect sharp discontinuities, a box-like wavelet function, such as the Haar, is better.

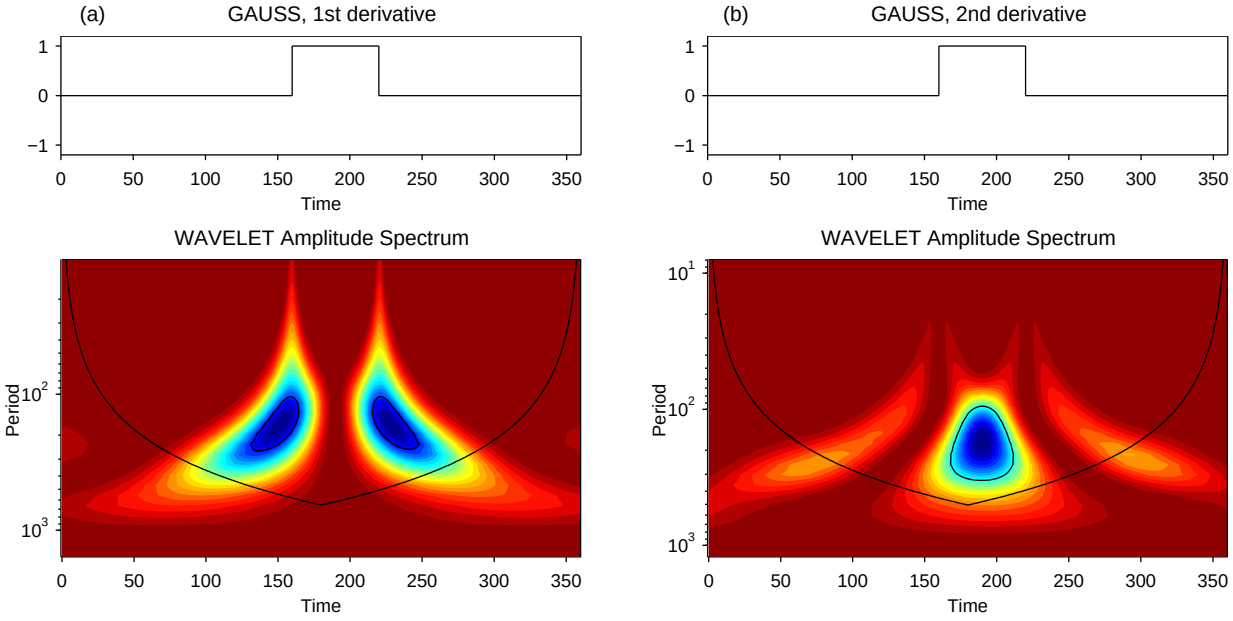

Figure 2.4. Wavelet transforms of the box-like function. (a) The first derivative of the Gaussian (see (2.11) for $m = 1$) and the second derivative of the Gaussian ((2.11), $m = 2$) are used. Colorscales change from red (minimum) to blue (maximum). Cone-of-influence and 95%-significance lines were added to the scalograms (their description same as in Figure 2.2). Large-scale spectra (periods 100-300s) are related to the width of the box, small-scale spectra (periods 10-50s) detect edges of the box. As the first derivative of the Gaussian is odd function, it shows directly the locations of the edges, while the even second derivative of the Gaussian is better for the peak localization.

For smooth features a cosine based function, such as the Morlet, is preferred.

Even or odd. When using real wavelet functions one must choose whether to use an even or odd function. One would use an odd wavelet function to determine exactly where a feature begins and ends. An even wavelet is used to determine the location of peaks (see Figure 2.4).

Vanishing moments. A function $f(x)$ has a m-vanishing moment when:

$$\int_{-\infty}^{+\infty} x^m f(x) dx = 0\,. \tag{2.8}$$

A wavelet transformation which uses a wavelet function with one or more vanishing moments is not affected by linear trends of the analysed function on the wavelet 'support' area (Figure 2.3d). A wavelet with many vanishing moments gives a small coefficient when used for low frequency analysis; however it is better for high frequency analysis. Since the number of oscillations of the wavelet function is proportional to the number of vanishing moments, wavelets with too many vanishing moments can result in low-valued false maxima in the signal.

2.4 Morlet wavelet, Gaussian wavelets

For the time-series analysis (see Chapter 3 dealing with the analysis of thermal convection) we have chosen the Morlet wavelet (Figure 2.5a):

$$\psi_0(\eta) = \pi^{-\frac{1}{4}} e^{i\omega_0\eta} e^{-\frac{1}{2}\eta^2}\,, \tag{2.9}$$

where ω_0 is a nondimensional frequency (usually taken to be 6). We discarded the correction term which is necessary to enforce the admissibility condition (2.3) because it is numerically negligible for $\omega_0 \geq 5.6$ (Van den Berg, 1999) and longer time-series. The wavelet function is complex, oscillating and thin in Fourier space, and that is why it is a powerful tool for detecting frequency behavior of an oscillating signal.
The relationship between the Fourier period T and the Morlet wavelet scale a is (Torrence and Compo, 1998):

$$T = \frac{4\pi a}{\omega_0 + \sqrt{2 + \omega_0^2}}\,. \tag{2.10}$$

The Gaussian (DOG) wavelets are more suitable for detection of the structure and behavior of multi-dimensional geophysical fields such as gravity or temperature fields. They have good space resolution because they are real and relatively thin in physical space (see Figure 2.5b-d).
The m-derivative of the Gaussian is defined (in 1-D) as follows (Torrence and Compo, 1998) :

$$\psi_0(\eta) = \frac{(-1)^{\mathrm{m}+1}}{\sqrt{\Gamma(m+\frac{1}{2})}} \frac{d^{\mathrm{m}}}{d\eta^{\mathrm{m}}}(e^{-\frac{1}{2}\eta^2})\,, \tag{2.11}$$

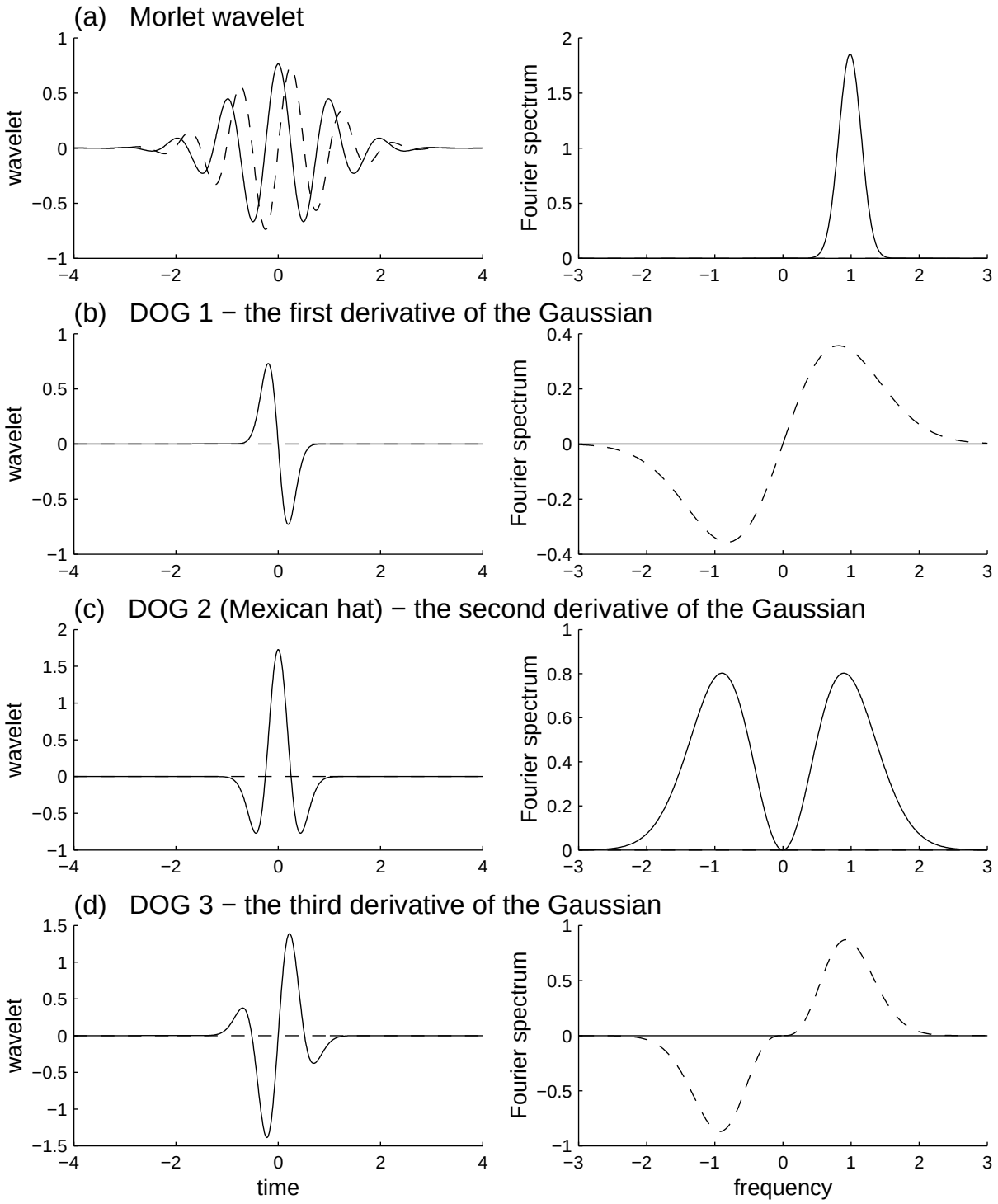

Figure 2.5. (a) Morlet wavelet (2.9) and (b)-(d) DOG (derivatives of the Gaussian) wavelets (2.11). The left panels present time behaviors of the wavelet functions, the right panels show the Fourier spectra of the wavelets. The solid lines indicate real parts of the functions or the Fourier spectra, the dash lines indicate their imaginary parts. All presented wavelets have the same spatial resolution $T = 1s$, the different width of the temporal or spectrum curves illustrate better or worse temporal or frequency resolution of the wavelets.

where Γ is the gamma function :

$$\Gamma(x) = \int_0^\infty t^{x-1} e^{-t} dt \tag{2.12}$$

The relationship between the Fourier period T and the DOG wavelet scale a is (Torrence and Compo, 1998):

$$T = \frac{2\pi a}{\sqrt{m + \frac{1}{2}}}. \tag{2.13}$$

Each m-derivative of the Gaussian has m vanishing moments. For our analysis we prefer DOG wavelets of low m which have less oscillation peaks. Commonly, we use the Mexican-hat wavelet (also called the Merr wavelet) which is the second derivative of the Gaussian. It is good for determining peaks in the analysed field because it is even. Moreover, it is also isotropic in direction.

The definition of the 2-D Mexican-hat wavelet function is:

$$\psi_0(\boldsymbol{\eta}) = (2\pi)^{-\frac{1}{2}} \left(\frac{\partial^2}{\partial \eta_1^2} + \frac{\partial^2}{\partial \eta_2^2}\right) e^{-\frac{1}{2}|\boldsymbol{\eta}|^2} = (2\pi)^{-\frac{1}{2}} (2 - |\boldsymbol{\eta}|^2) e^{-\frac{1}{2}|\boldsymbol{\eta}|^2}. \tag{2.14}$$

The 2-D second derivative of the Gaussian is isotropic in direction (Figure 2.6) whereas the first and third derivatives are not.

The 2-D isotropic CWT analyzes an area that has the same width in 2 directions (e.g. a square or a circle). For anisotropic structures the wavelet scale a is able to 'see' an average of the size of the feature in the x-direction and the size in the y-direction. For a circular structure where the width in the both directions equals the $\lambda/2$, we have an input signal $f(x, y) = e^{i\frac{2\pi}{\lambda}(x+y)}$ instead of

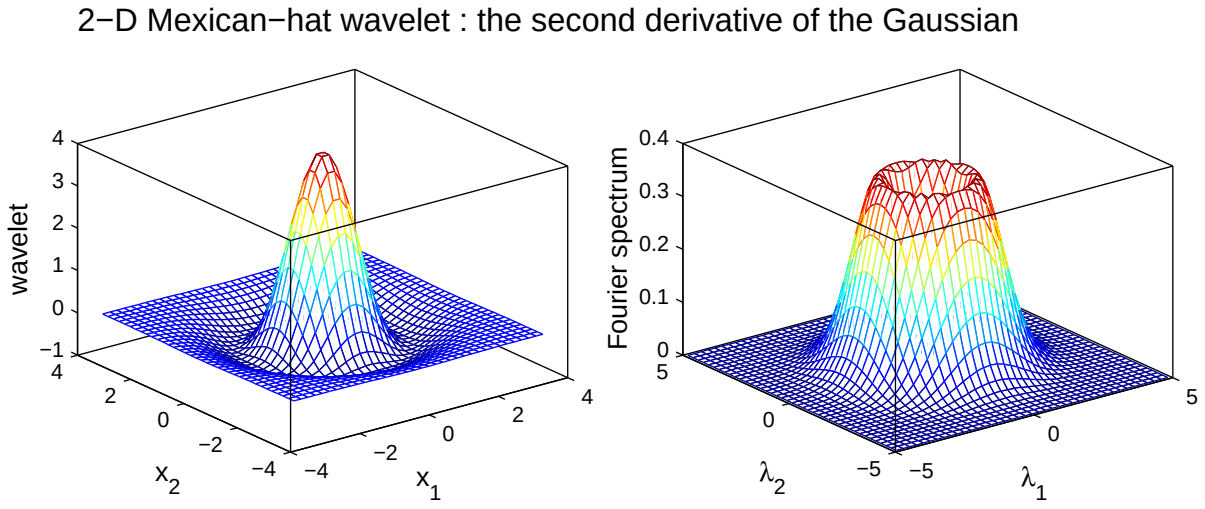

Figure 2.6. 2-D Mexican-hat wavelet, definition (2.14).

the 1-D input $f(x) = e^{i\omega_T t}$ which leads to the condition (2.5). Then the relationship between the wavelet scale a and λ is:

$$\lambda = \sqrt{\frac{2}{3}} 2\pi a \,. \tag{2.15}$$

For a oval structure where the width equals to $\lambda/2$ and the length goes to $+\infty$, the input signal is $f(x, y) = e^{i\frac{2\pi}{\lambda}x}$ and the relationship between the wavelet scale a and λ is:

$$\lambda = \frac{1}{\sqrt{3}} 2\pi a \,. \tag{2.16}$$

These different scale-wavelength relationships originate from the isotropic requirement on the wavelet transform. When we will speak about resolution of the 2-D wavelets in the following chapters, the expression (2.15) will be considered.

2.5 Scalograms

Scalograms represent the portrayal of a wavelet-transformed quantity over the scale a and the position $\boldsymbol{b}$ (e.g. Figure 2.4). The wavelet-transformed quantity is usually the local power spectrum of the signal given by the n-norm:

$$E_{\mathrm{n}}(a, \boldsymbol{b}) = |\Psi_{\mathrm{f}}(a, \boldsymbol{b})|_{\mathrm{L_n}} \,. \tag{2.17}$$

We can include the sign of the local anomaly at location $\boldsymbol{b}$:

$$\tilde{E}_{\mathrm{n}}(a, \boldsymbol{b}) = \mathrm{sign}(f(\boldsymbol{b})) \cdot |\Psi_{\mathrm{f}}(a, \boldsymbol{b})|_{\mathrm{L_n}} \,. \tag{2.18}$$

If the wavelet function is real, such as the Mexican hat, and $n = 1$, then the quantity $\tilde{E}_{\mathrm{n}}$ in equation (2.18) is equal to the wavelet transform Ψ_{f}.

We use a 1-D wavelet transform for time-series analysis. The scalogram of a 1-D wavelet transform is the 2-D function, see Figures 2.2 and 2.4. The horizontal axis is time, and the vertical axis is the wavelet scale a or the corresponding Fourier period T. It is possible to separate values of 95% significance level from white or red noise (Torrence and Compo, 1998).

In order to study 2-D data such as geoid anomalies one can take a 1-D slice of the data and study features along this line with a 1-D wavelet transform (Simons and Hager, 1997; Simons et al., 1997). This, however, does not allow one to examine the data in its true 2-D state.

We used a 2-D CWT to study 2-D fields including geoid anomalies, convection simulations and mixing models. The computation itself is extremely short, about 10 minutes of CPU time on a R4000 SGI for the largest fields analyzed. The 2-D CWT results in a 3-D scalogram with the original two dimensions, b_{x} x b_{y}, plus the dimension of scale a. Visualization and storage of these scalograms is difficult. A scalogram with 20 scales from a 2-D dataset with grid size 5100 x 1100

results in a binary file of 45 MB. Visualization of these scalograms requires large memory (5 - 10 GB) and a high definition monitor (200 pixels/inch) or a wall with 10 million pixels.

The scalograms contain a large amount of complicated data. Presenting the information in a way that can be easily digested by the human eye is daunting. One solution is to make a movie in which the 3-D scalogram is rotated so that all sides of the box can be viewed. This does not solve the problem of the amount of memory needed to visualize the box. It also does not allow unobscured study of intermediate scales which are in the center of the box. Another way to make the information in the box easier to digest is to use a priori knowledge. For example, if you are looking for plumes in tomographic data of the Earth's mantle, you could dampen the signal from scales on the order of 1000s of kms so that it would be easier to view regional, smaller scale features.

One can also use 2-D cross-sections of the scalogram. We can take a cross-section of $b_x \times b_y$ at a fixed scale a, or we can take a cut $a \times b_x$ or $a \times b_y$ at a fixed b_y or b_x. The second cuts emphasize the peripheral vision of the scalogram which is due to the fact that the 2-D wavelet transform analyzes an area around each grid point. It can happen that, e.g., the signature of the plume will appear on the scalogram even though the cut through the scalogram was taken slightly off the plume. One can still detect interesting features even if their exact location was not chosen correctly.

We have found that the cross-section of $b_x \times b_y$ at a fixed scale a was the most sensible way to present our data. We took cross-sections of the data at large, medium, and small scales to emphasize the different features that were visible at these scales (see Figure 2.3). Examples of scalograms from the results of the 2-D wavelet analysis will be presented in Chapter 4.

Many geophysical datasets such as tomographic signals are really 3-D in physical space. A 3-D isotropic CWT results in a 4-D scalogram which presents not only even greater visualization problems but also storage problems since they require a large amount of disk space (Bergeron et al., 2000a). New methods for extracting features from high-dimensional datasets are required. One of such method is $E_{\max}/k_{\max}$ analysis (Bergeron et al., 1999).

2.6 $E_{\max}$ and $k_{\max}$

As mentioned in the preceding section, the information produced by the 2-D local CWT is difficult to visualize because a whole spectrum is rendered at each grid point. In order to synthesize and assimilate this large amount of information efficiently, we will extract the two proxy quantities, $E_{\max}$ and $k_{\max}$ (Bergeron et al., 1999).

The maximum of the local energy $E_{\max}$ is defined as the maximum of the wavelet spectrum energy over a specific range of wavenumbers (wavenumber k is the inverse of the wavelet scale a, $k = \frac{1}{a}$):

$$E_{\max}(\boldsymbol{b}) = \max_{<k_1,k_2>} |\Psi_f(\frac{1}{k}, \boldsymbol{b})|^2 . \tag{2.19}$$

$E_{\max}$ is calculated for each grid point in the dataset. The $E_{\max}$ distribution is then shown on an $E_{\max}$ map (see Figure 2.7). The sign of $E_{\max}$ can be preserved in the same way as done in (2.18):

$$\tilde{E}_{\max}(\boldsymbol{b}) = \text{sign}(f(\boldsymbol{b})) \cdot \max_{<k_1,k_2>} |\Psi_f(\frac{1}{k}, \boldsymbol{b})|^2 . \tag{2.20}$$

The local wavenumber at which $E_{\max}$ occurs is $k_{\max}$ (method of determination of these two proxies is shown in Figure 2.7).

The main power of the $E_{\max}/k_{\max}$ analysis consists primarily in the detection of small-scale structure. In general, the energy decreases with increasing wavenumber. Therefore, in most cases the smallest wavenumbers k prevail in the $k_{\max}$ maps (see Figure 2.8a). When there is an energy peak, the higher wavenumbers pop in the $k_{\max}$ map. Therefore, variations of k occur along boundaries where there are sharp gradients in $E_{\max}$ map. A $k_{\max}$ map will consist of flat plateaus in small k outlined by areas of high $E_{\max}$ gradient (e.g. Figure 4.2, page 74). This makes k_{max} a strong proxy for detecting boundaries between features.

Usually we normalize Ψ_f in (2.19) at each grid point by the areal average of Ψ_f for the associated scale (Figure 2.8). When studying a specific region of the data we can normalize Ψ_f with the regional average of Ψ_f rather than the global average. This allows us to better analyze local features that may be dampened by very high values of Ψ_f in the global average. This technique was used to study regional signals of the Earth's geoid in Chapter 4.

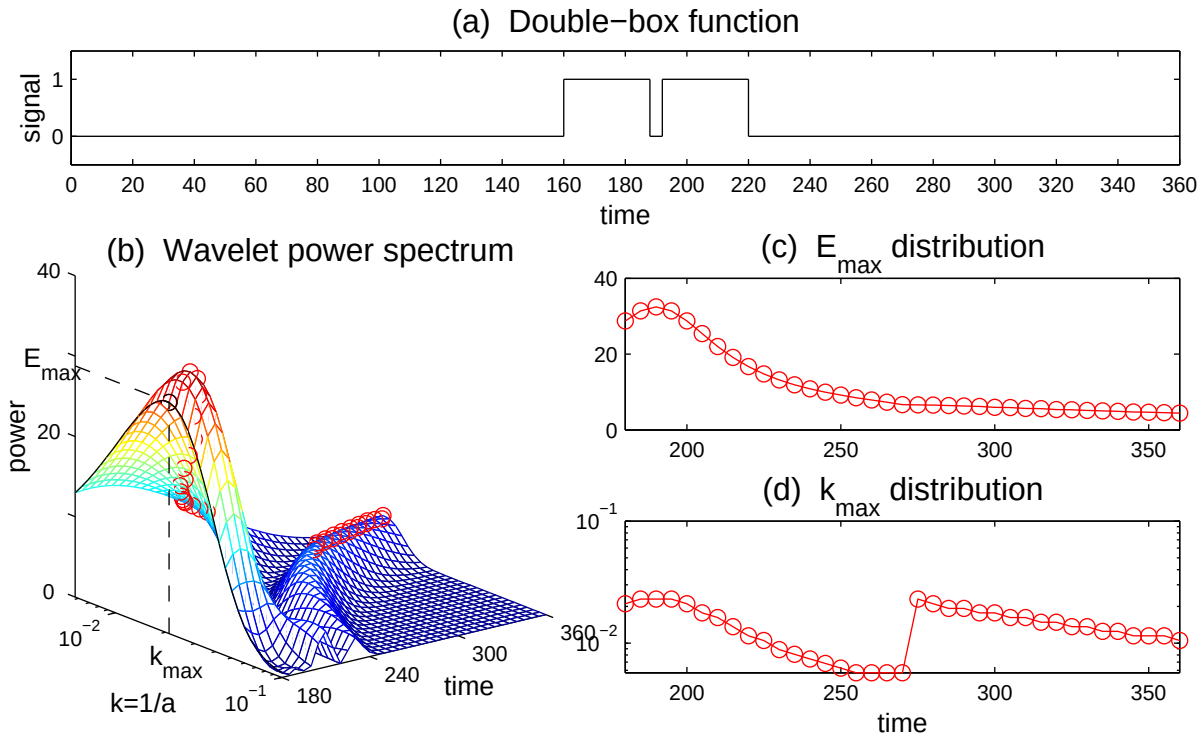

Figure 2.7. Algorithm for $E_{\max}/k_{\max}$ determination. (a) As an example a 1-D step function is analyzed. (b) We compute wavelet power spectrum. For each time the maximum energy $E_{\max}$ and the corresponding wavenumber $k_{\max}$ are found (see the red circles). Then the $E_{\max}$ and $k_{\max}$ distributions are put into separate graphs (c) and (d).

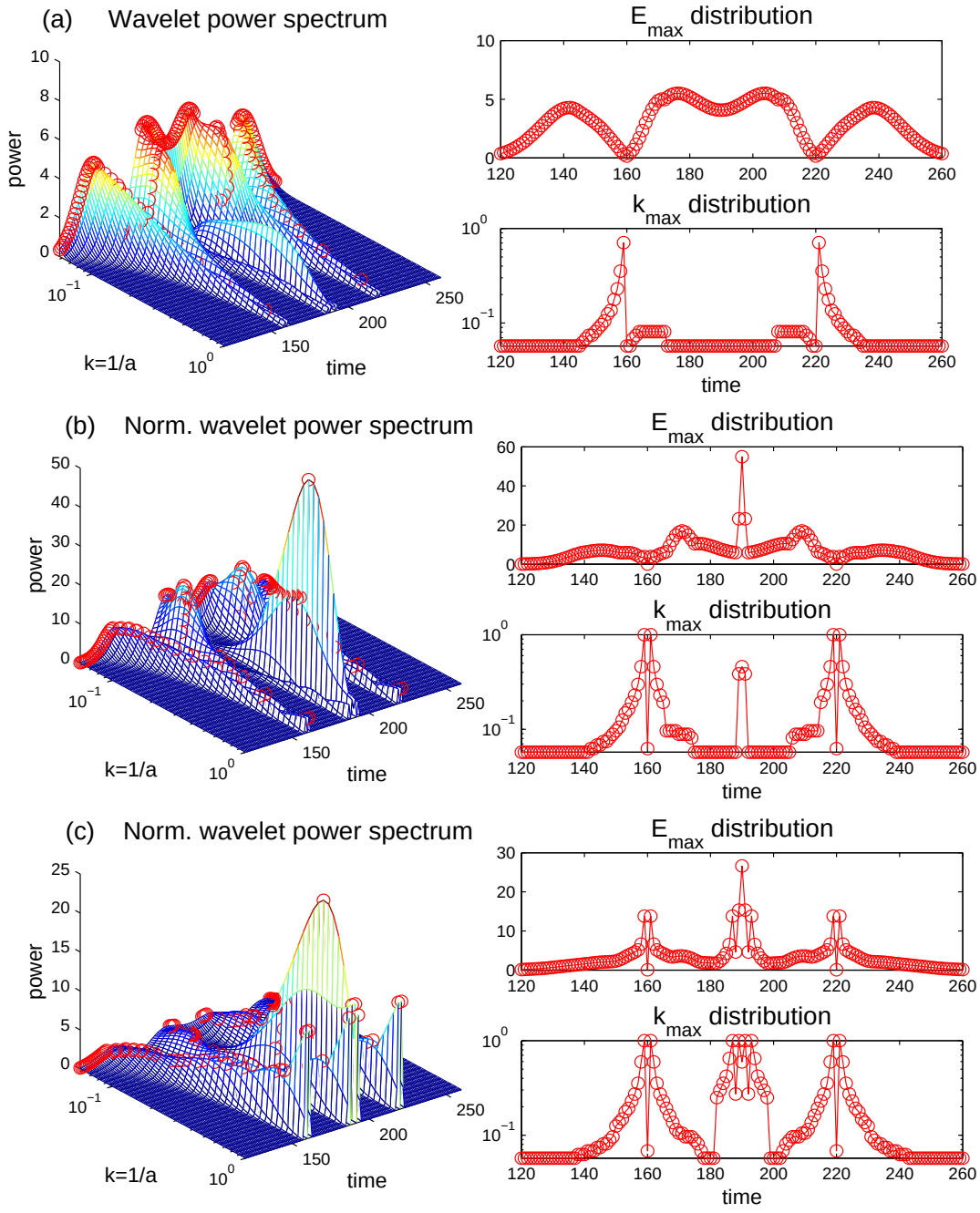

Figure 2.8. $E_{\max}/k_{\max}$ distributions for the small-scale range of wavenumbers k, other the same as in Figure 2.7. Different kinds of normalization of the wavelet power spectra were used. (a) The $E_{\max}/k_{\max}$ proxies without any normalization are influenced by global decreasing trend of the power spectrum when k increases. Thus the gap between two boxes (see Figure 2.7a) is not detected. (b) The second square of the wavelet power spectrum Ψ_f was normalized by an areal average power. $k_{\max}$ map is able to distinguish both sides of the two boxes. (c) The wavelet power spectrum was normalized by only an areal average power. The trend of the wavelet power became inverse from the original one, now it is increasing with the wavelength k. For following $E_{\max}/k_{\max}$ computation we use (b) normalization which is sensitive to the whole considered range of wavelengths k.

The reduction of the wavelet spectra into the two proxy quantities $E_{\max}$ and $k_{\max}$ can be viewed at as a low-parameterization. In analyzing higher dimensional data such as 3-D tomography datasets 4-D scalograms will be generated. These will require a huge amount of storage space and will be impossible to visualize. Proxy quantities will become more important as the dimension of the system we are analyzing increases.

2.7 What next?

In this chapter, we have presented basic theory about the continuous wavelet transform used for time-frequency analysis of 1-D time signals or 2-D geophysical fields. We demonstrated the good ability of the wavelet transform to detect structures of different scales in the given field, together with the ease computation of the wavelet spectra. We draw our attention to necessity of careful selection of the wavelet base function, depending both on the nature of the analyzed signal and on the phenomena we are looking for in the signal.

Anybody who would like to use a method should also know its handicaps. As the wavelet transform is usually computed with the help of the fast Fourier transform, inaccurate wavelet spectrum in the edge areas of the signal (or field) can occur. The advantage of the continuous wavelet transform in continuous output spectra brings together disadvantages in high computer memory requirements, especially in the case of the higher-dimensional wavelet transform. Visualization of scalograms from 2-D (and more dimensional) wavelet analysis needs advanced visualization softwares. We presented several ideas in this chapter of how these difficulties can be overcome.

There are plenty of possible trends where one can continue her or his wavelet studies. The readability of the time-scale wavelet representation can be improved by the reassignment method (Auger and Flandrin, 1995). Distortion of the signal on the sphere due to its Mercator projection to a Cartesian box will be eliminated by using the continuous wavelet transform directly on a sphere (Torresani, 1995; Holschneider, 1996; Antoine and Vandergheynst, 1998; Li, 1999). Searching objects of similar shapes in the signals enhanced by applying the cross-correlations to the wavelet spectra of these signals. Extraction of the object with certain properties from the signal can be realized with help of inverse continuous wavelet transform (Daubechies, 1992). The anisotropic wavelet transform is waiting for its application.

To conclude, there is no doubt that the wavelet transform realized great progression during last 20 years, and its efficiency and power are confirmed by the large number of articles from a variety of scientific fields published each year.

Chapter 3

Thermal Convection & Chaos

3.1 Introduction

The study of thermal convection is of crucial importance for understanding the dynamics of the Earth's interior since the advection of heat is one of the fundamental modes of heat transfer in the Earth. The other mode is the conduction of heat caused by an interchange of kinetic energy among oscillating molecules in the crystal lattices of minerals. Models of the Earth's cooling without advection are unstable (see the stability analysis by, e.g., Chandrasekhar, 1961) due to the inefficiency of conduction. The Earth's mantle dynamics, which is, in principle, induced by thermal convection, is chaotic on geological time-scales (Turcotte, 1992; Yuen, 1992) as well as on short time-scales (Li and Nyland, 1994). The reason is that the partial differential equations describing thermal convection represent a nonlinear dynamical system, which can yield different regimes varying from stationary states, to periodic behavior of solutions and, finally to chaotic states. The fundamental nonlinearity is the advection of heat which is present in all models of thermal convection. This chapter is devoted to a detailed study of this nonlinearity. In the real Earth, there are other nonlinearities that influence the behavior of the studied system such as the temperature and pressure dependence of viscosity (Karato, 1993) as well as of the thermal conductivity (Hofmeister, 1999), the stress dependence of viscosity (Van den Berg et al., 1993), the radiation of heat (Matyska et al., 1994), and dissipation and adiabatic heating/cooling (Hansen et al., 1993; Velímský and Matyska, 2000). Moreover, convection patterns can also be influenced by the presence of phase changes (Tackley et al., 1993).

Here we have adopted a simple model of an incompressible fluid in the classical Boussinesq approximation in a 2-D spherical shell heated from below with the axisymmetry with respect to the z-axis of the coordinate system. Such a system is controlled by only one parameter—the Rayleigh number Ra. This enables us to concentrate on a detailed study of physical behavior of changes in the system due to changes of the controlling parameter.

A fundamental question is the applicability of thermal convection models to present-time data measured on the Earth's surface. For example, a comparison of thermal anomalies obtained from convection models with seismic tomography models obtained from inversions of time arrivals of seismic wave phases, whole waveforms, and/or free oscillations is questionable since seismic tomography yields only a present 'snapshot' of the state of the Earth. Without a tool for quantifying chaos, we

cannot determine when the chaoticity is so strong that such a comparison cannot be made. This is the reason why quantitative measures of chaoticity could substantially unify convection modelling with other fields of geodynamics.

One way how to quantify chaoticity is by the dimension of the attractor. Fractal dimensions for 2-D convection in Cartesian geometry was estimated, e.g., by Vincent and Yuen (1989), another possible quantity is the correlation dimension (e.g. Nese, 1987; Raidl, 1995), which is useful both for measured data and for higher dimensional systems. To reveal the internal dynamics of convection systems, we used the attractor dimension and the modern technique of the wavelet transform to investigate the time-evolution of time-series of global and semi-global quantities (the total heat flow through the surface or kinetic energy). We also employed the 2-D wavelet transform of temperature and vorticity fields to better understand their structure on different scales.

3.2 Governing equations

In this section we transfer the fundamental laws of conservation into the form used in our mantle convection model. We begin with the conservation laws. Then we simplify the system with the Boussinesq approximation of equations, nondimensionalize the system, and, finally, express it in spherical coordinates.

3.2.1 The conservation laws and boundary conditions

A full description of thermal convection is given by the laws of mass, momentum, and energy conservation:

$$\frac{\partial \varrho}{\partial t} + \nabla \cdot (\varrho \boldsymbol{v}) = 0\,, \tag{3.1}$$

$$\nabla \cdot \boldsymbol{\tau} + \varrho\, \boldsymbol{g} = \varrho \left(\frac{\partial \boldsymbol{v}}{\partial t} + (\boldsymbol{v} \cdot \nabla)\boldsymbol{v} \right)\,, \tag{3.2}$$

$$\varrho\, c_\mathrm{p} \frac{\partial T}{\partial t} = -\varrho\, c_\mathrm{p}\, (\boldsymbol{v} \cdot \nabla)\, T + \nabla \cdot (\boldsymbol{k} \cdot \nabla T) + \sigma : \nabla \boldsymbol{v} + \varrho\, \alpha T\, \boldsymbol{g} \cdot \boldsymbol{v} + Q\,, \tag{3.3}$$

with the rheological relationship

$$\boldsymbol{\tau} = -p\, \boldsymbol{I} + \boldsymbol{\sigma}(\boldsymbol{v})\,, \quad \lim_{\boldsymbol{v} \to 0} \boldsymbol{\sigma}(\boldsymbol{v}) = 0 \tag{3.4}$$

and the equation of state

$$f(T, \varrho, p) = 0\,, \tag{3.5}$$

where $\boldsymbol{v}$ is the velocity, T is the temperature, ϱ is the density, $\boldsymbol{\tau}$ is the stress tensor with its deviation part $\boldsymbol{\sigma}$, $\boldsymbol{g}$ is the gravity acceleration, c_p is the isobaric specific heat, $\boldsymbol{k}$ is the thermal conductivity, α is the thermal expansion coefficient, p is the pressure, and Q is the internal heat source.

The free surface and core-mantle boundary (CMB) are free-slip boundaries with no mass flux passing through them, i.e.,

$$\boldsymbol{v} \cdot \boldsymbol{n} = 0\,, \tag{3.6}$$

and

$$\boldsymbol{\tau} \cdot \boldsymbol{n} - ((\boldsymbol{\tau} \cdot \boldsymbol{n}) \cdot \boldsymbol{n})\boldsymbol{n} = 0\,. \tag{3.7}$$

The boundary conditions for temperature can be chosen by either prescribing its magnitude directly (the Dirichlet condition) or keeping the value of heat flow passing through the boundary (the Neumann condition). We have chosen the former one for our mantle convection modelling:

$$\begin{array}{ll} T = T_{\mathrm{s}} & \text{at the surface} \\ T = T_{\mathrm{b}} & \text{at the CMB} \end{array}\,. \tag{3.8}$$

3.2.2 Boussinesq approximation

From the momentum equation (3.2) and the rheology relation (3.4) we can easily obtain the equation of equilibrium characterizing the hydrostatic state,

$$\nabla p_{\mathrm{o}} = \varrho_{\mathrm{o}}\, \boldsymbol{g}_{\mathrm{o}}\,, \tag{3.9}$$

where p_{o} is the hydrostatic pressure and ϱ_{o} and $\boldsymbol{g}_{\mathrm{o}}$ are density and the acceleration due to gravity in the reference state.

We neglect density changes caused by the pressure deviations $\Pi = p - p_{\mathrm{o}}$ in the equation of state (3.5) and consider only the linear term in dependence of density ϱ on temperature deviations $T - T_{\mathrm{o}}$:

$$\varrho = \varrho_{\mathrm{o}}(1 - \alpha(T - T_{\mathrm{o}}))\,. \tag{3.10}$$

In the mass conservation law (3.1) we consider only absolute term in the linearization, i.e. $\varrho \doteq \varrho_{\mathrm{o}}$ where the reference density ϱ_{o} is time-independent. Equation (3.1) becomes

$$\nabla \cdot (\varrho_{\mathrm{o}} \boldsymbol{v}) = 0\,. \tag{3.11}$$

In the momentum conservation law (3.2) we use (3.9) and (3.10) and neglect all the quadratic terms on the left-hand side and the thermal expansion on the right-hand side:

$$-\nabla\Pi + \nabla \cdot \sigma - \varrho_{\mathrm{o}}\alpha(T - T_{\mathrm{o}})\boldsymbol{g}_{\mathrm{o}} + \varrho_{\mathrm{o}}(\boldsymbol{g} - \boldsymbol{g}_{\mathrm{o}}) = \varrho_{\mathrm{o}} \left(\frac{\partial \boldsymbol{v}}{\partial t} + \boldsymbol{v} \cdot \nabla \boldsymbol{v} \right)\,. \tag{3.12}$$

The same procedure is used for the energy conservation law (3.3):

$$\varrho_{\mathrm{o}}\, c_{\mathrm{p}} \frac{\partial T}{\partial t} = \nabla \cdot (\boldsymbol{k} \cdot \nabla T) - \varrho_{\mathrm{o}} c_{\mathrm{p}}\, \boldsymbol{v} \cdot \nabla T - \varrho_{\mathrm{o}} v_{\mathrm{r}} \alpha\, T g_{\mathrm{o}} + \sigma : \nabla \boldsymbol{v} + Q\,. \tag{3.13}$$

The system (3.11)-(3.13) is referred to as the compressible extended Boussinesq approximation. If we neglect compressibility (we replace (3.11) by $\nabla \cdot \boldsymbol{v} = 0$), we obtain the system of equations

known as the incompressible extended Boussinesq approximation. The Boussinesq approximation thus consists of neglecting all density deviations from the reference state with the exception of the buoyancy force, where the thermal expansion is taken into account.

The classical Boussinesq approximation represents a subsequent simplification of the studied system of equations. The reference density ϱ_o, the reference gravity acceleration $\boldsymbol{g}_\mathrm{o}$, the thermal expansion coefficient α, the isobaric specific heat c_p, the thermal conductivity $\boldsymbol{k}$ and the internal heat source Q are constant, and the rheology is taken to be that of a Newtonian fluid:

$$\boldsymbol{\sigma} = \eta(\nabla \boldsymbol{v} + (\nabla \boldsymbol{v})^T) \tag{3.14}$$

with a constant dynamic viscosity η. Moreover, both dissipation $\boldsymbol{\sigma} : \nabla \boldsymbol{v}$ and adiabatic heating $-\varrho_\mathrm{o} v_\mathrm{r} \alpha_\mathrm{p} T g_\mathrm{o}$ are not considered in the thermal equation. The magnitude of the self-gravitation term $\varrho_\mathrm{o}(\boldsymbol{g} - \boldsymbol{g}_\mathrm{o})$ in the equation (3.12) is one order lower than the buoyancy term $-\varrho_\mathrm{o}\alpha(T - T_\mathrm{o})\boldsymbol{g}_\mathrm{o}$; therefore, it does not substantially influence the basic physics of the thermal convection and can be omitted.

Thus, we finally get the simplified system

$$\nabla \cdot \boldsymbol{v} = 0\,, \tag{3.15}$$

$$-\nabla \Pi + \eta \nabla^2 \boldsymbol{v} - \varrho_\mathrm{o}\alpha(T - T_\mathrm{o})\boldsymbol{g_o} = \varrho_\mathrm{o}\left(\frac{\partial \boldsymbol{v}}{\partial t} + \boldsymbol{v} \cdot \nabla \boldsymbol{v}\right)\,, \tag{3.16}$$

$$\frac{\partial T}{\partial t} = \kappa \nabla^2 T - \boldsymbol{v} \cdot \nabla T + \frac{Q}{\varrho_\mathrm{o} c_\mathrm{p}}\,, \tag{3.17}$$

where $\kappa = \frac{k}{\varrho c_\mathrm{p}}$.

3.2.3 Nondimensionalization

The system in the classical Boussinesq approximation (3.15)-(3.17) can be further simplified by introducing new dimensionless variables, denoted by primes:

$$\boldsymbol{r} = d\boldsymbol{r}'\,,\quad t = \frac{d^2}{\kappa}t'\,,\quad \boldsymbol{v} = \frac{\kappa}{d}\boldsymbol{v}'\,,\quad \Pi = \frac{\eta\kappa}{d^2}\Pi'\,,\quad T = T_\mathrm{s} + (T_\mathrm{b} - T_\mathrm{s})T'\,, \tag{3.18}$$

where $\boldsymbol{r}$ is the position vector and d is the characteristic measure of the system (usually the thickness of the convection box)

The system (3.15)-(3.17), rewritten in dimensionless variables, is

$$\nabla' \cdot \boldsymbol{v}' = 0\,, \tag{3.19}$$

$$-\nabla'\Pi' + \nabla'^2 \boldsymbol{v}' + Ra\,(T' - T'_\mathrm{o})\boldsymbol{e}_\mathrm{r} = \frac{1}{Pr}\left(\frac{\partial \boldsymbol{v}'}{\partial t'} + \boldsymbol{v}' \cdot \nabla' \boldsymbol{v}'\right)\,, \tag{3.20}$$

$$\frac{\partial T'}{\partial t'} = \nabla'^2 T' - \boldsymbol{v}' \cdot \nabla' T' + \frac{Raq}{Ra}\,, \tag{3.21}$$

where

$$Pr = \frac{\nu}{\kappa} \qquad \text{is the Prandtl number,} \tag{3.22}$$

$$\nu = \frac{\eta}{\varrho_o} \qquad \text{is the kinematic viscosity,} \tag{3.23}$$

$$Ra = \frac{\alpha d^3 g_o (T_b - T_s)}{\nu\kappa} \qquad \text{is the Rayleigh number, and} \tag{3.24}$$

$$Raq = \frac{\alpha g_o Q d^5}{\nu\kappa k} \qquad \text{is the Rayleigh number for heat sources.} \tag{3.25}$$

Since the Prandtl number of the real Earth is about 10^{24}, we consider it to be infinite. We also neglect the internal heat sources. Then the simplified system in dimensionless variables takes the form

$$\nabla \cdot \boldsymbol{v} = 0\,, \tag{3.26}$$

$$-\nabla\Pi + \nabla^2\boldsymbol{v} + Ra\Theta\boldsymbol{e}_r = 0\,, \tag{3.27}$$

$$\frac{\partial\Theta}{\partial t} = \nabla^2\Theta - \boldsymbol{v}\cdot\nabla\Theta - \boldsymbol{v}\cdot\nabla T_o\,, \tag{3.28}$$

where we omitted the primes and applied the temperature deviation $\Theta = T - T_o$ with the conductive (dimensionless) temperature T_o.

The equations (3.26) and (3.27) together with (3.6) and (3.7) represent an equilibrium system, which yields the mapping $\Theta \longmapsto \boldsymbol{v}$. The only independent variable of the nonlinear equation (3.28) is the temperature deviation Θ. Moreover, the behavior and chaoticity of the system (3.26)-(3.28) depends only on one parameter, the Rayleigh number Ra, defined in (3.24).

3.2.4 Axisymmetrical shell geometry

In the previous subsection we introduced the classical Boussinesq approximation of the thermal convection of an incompressible fluid. Here we use a 2-D geometrical approximation for computational purposes. We chose a spherical geometry, which breaks the symmetry between upwellings and downwellings that is typical of Cartesian convection models with constant parameters.

Let us consider a spherical coordinate system (r,θ,ϕ). Axisymmetrical flow is then characterized by zero value of the ϕ-component of velocity. Moreover, no state variable and no physical parameter depends on ϕ; so that velocity

$$\boldsymbol{v} \equiv (v_r, v_\theta, v_\phi) = (v_r(r,\theta), v_\theta(r,\theta), 0) \tag{3.29}$$

is confined between two spherical surfaces with radii r_1 and r_2.

If we introduce the stream function ψ:

$$\boldsymbol{v} = (v_r, v_\theta, 0) = \left(\frac{1}{r^2\sin\theta}\frac{\partial\psi}{\partial\theta}, -\frac{1}{r\sin\theta}\frac{\partial\psi}{\partial r}, 0\right), \tag{3.30}$$

the equation of continuity (3.26) is satisfied. The vorticity ω is defined by means of the ϕ-component of the rotation of velocity:

$$\nabla \times \boldsymbol{v} = (0, 0, \frac{\omega}{r \sin\theta}) \,. \tag{3.31}$$

By comparing the definitions (3.30) and (3.31) one can obtain the relation between the stream function and the vorticity:

$$-\omega = \mathcal{D}(\psi) \,, \tag{3.32}$$

where $\mathcal{D}$ is the Laplacian-like operator,

$$\mathcal{D} \equiv \frac{\partial^2}{\partial r^2} + \frac{1}{r^2}\frac{\partial^2}{\partial \theta^2} - \frac{cotg\theta}{r^2}\frac{\partial}{\partial \theta} \,. \tag{3.33}$$

In the momentum equation (3.27) we use (together with the equation of continuity (3.26)) the identity $\nabla^2 \cdot \boldsymbol{v} = \nabla(\nabla \cdot \boldsymbol{v}) - \nabla \times (\nabla \times \boldsymbol{v}) = -\nabla \times (\nabla \times \boldsymbol{v})$. Then we apply rotation $\nabla\times$ and the identity $\nabla \times (\nabla\Pi) = 0$:

$$\mathcal{D}(\omega) = Ra \sin\theta \frac{\partial \Theta}{\partial \theta} \,. \tag{3.34}$$

The energy conservation (3.28) is of the same form except that the stream function ψ (3.30) is used instead of velocity $\boldsymbol{v}$.

From the computational point of view there are two kinds of boundary conditions around the spherical shell, free-slip and temperature. The free-slip boundaries are on the shell bottom top, where we require conditions (3.6) and (3.7). Equation (3.6), $v_r = 0$, is satisfied when

$$\frac{\partial \psi}{\partial \theta} = 0 \,. \tag{3.35}$$

Equation (3.7), $\sigma_{r\theta} = 0$, together with (3.14) yields (with help of (3.30) and (3.32)):

$$\omega = -\frac{2}{r}\frac{\partial \psi}{\partial r} \,. \tag{3.36}$$

Temperature condition on the boundaries was chosen in the form of the Dirichlet condition (3.8); for temperature deviation $\Theta = T - T_o$ where T_o is the conductive temperature it gives

$$\Theta = 0 \,. \tag{3.37}$$

From the vorticity definition (3.31) we can see that the velocity $\boldsymbol{v}$ at $\theta = 0$ and $\theta = \pi$ can be finite only if the vorticity is going to zero on the boundaries:

$$\omega = 0 \,. \tag{3.38}$$

The stress condition (3.7) also applies to the boundaries at $\theta = 0$ and $\theta = \pi$ so that:

$$\frac{\partial \psi}{\partial r} = 0\,. \tag{3.39}$$

Since the conditions specified by (3.35) and (3.39) are along continuous boundaries, $\psi = constant$ along entire shell boundary. Because the magnitude of this constant is not constrained we can assign

$$\psi = 0 \tag{3.40}$$

at all boundaries in place of (3.35) and (3.39).
At $\theta = 0$ and $\theta = \pi$ we require zero heat flow, $\boldsymbol{n} \cdot \nabla T = 0$, through the boundary, which gives

$$\frac{\partial \Theta}{\partial \theta} = 0\,. \tag{3.41}$$

The following summarizes the boundary conditions for spherical shell geometry (see (3.36), (3.37), (3.38), (3.40), (3.41)):

$$\begin{aligned}
\psi\,(r{=}r_1, r_2) &= 0\,, && (3.42)\\
\omega\,(r{=}r_1, r_2) &= -\frac{2}{r}\frac{\partial \psi}{\partial r}\,, && (3.43)\\
\Theta\,(r{=}r_1, r_2) &= 0\,, && (3.44)
\end{aligned}$$

$$\begin{aligned}
\psi\,(\theta{=}0, \pi) &= 0\,, && (3.45)\\
\omega\,(\theta{=}0, \pi) &= 0\,, && (3.46)\\
\frac{\partial \Theta}{\partial \theta}\,(\theta{=}0, \pi) &= 0\,. && (3.47)
\end{aligned}$$

We complete equations and boundary conditions for axisymmetrical geometry by an expression of the conductive temperature T_o for this geometry. No motion characterizes the conductive state, and T_o satisfies equation $\nabla^2 T_o = 0$ together with boundary conditions $T_o(r_1) = 1$, $T_o(r_2) = 0$, where r_1, r_2 are radii of the bottom and top boundaries of the shell. Thus we get

$$T_o(r) = a + \frac{b}{r}\,, \tag{3.48}$$

where $a = -r_1/(r_2 - r_1)$, $b = r_1 r_2/(r_2 - r_1)$.

3.3 Computational aspects

We have used the code developed by Moser (1994) for computing the thermal convection described by the system of equations (3.26)-(3.28) (modified for the spherical shell geometry to the form (3.32), (3.34)), with the boundary conditions (3.42)-(3.47). The spatial derivatives were performed by a 4th-order finite-difference scheme (Fornberg, 1996). The linear system corresponding to the discretized version of the system (3.32) and (3.34) was solved by the ADI method with the time-stepping in (3.28) carried out by a fourth-order explicit Runge-Kutta scheme. Such an algorithm combines extreme simplicity in programming with a very high degree of accuracy. Moreover, memory requirements are low and increase nearly linearly with the total number of grid points (Larsen et al., 1997).

As it was mentioned in Subsection 3.2.3, the only parameter which controls the thermal convection in the classical Boussinesq approximation with no internal heating is the Rayleigh number Ra (3.24). In the real Earth, the Ra corresponding to whole mantle convection is about $10^6 - 10^7$ (Jarvis and Peltier, 1989), as we can see from the following mantle parameters and their characteristic values :

Quantity	**value**
d	$2.9 \times 10^6\ m$
g_o	$9.8\ ms^{-2}$
α	$1.4 \times 10^{-5}\ K^{-1}$
κ	$2.5 \times 10^{-6}\ m^2 s^{-1}$
ν	$4.3 \times 10^{17} m^2 s^{-1}$
$T_b - T_s$	$3500\ K$

Table 3.1. Representative values of parameters for whole mantle convection (source Jarvis and Peltier, 1989, except for the temperature: Boehler et al., 1995). For description of the quantities see Subsection 3.2.3. Some other representative values for the kinematic viskosity: $3 \cdot 10^{18}$ to $3 \cdot 10^{19}\ m^2 s^{-1}$ for the lower mantle (Turcotte and Schubert, 1982), $3 \cdot 10^{13}$ to $3 \cdot 10^{14}\ m^2 s^{-1}$ for the low viscosity zone (Turcotte and Schubert, 1982; Whitehead, 1982).

We suggest that different definitions of the Rayleigh number Ra from the definition (3.24) can exist (e.g., without including the viscosity η). Here we call attention to characteristic measure d of the system (see (3.18)) which is usually equal to the thickness of the convective box. As we continued the work of Moser (1994), we left an original parametrization with nondimensional radii of the bottom and top boundaries r_1, r_2 equal to 1, 1.83, respectivaly. Thus the measure d corresponds to the radius of the CMB (core-mantle boundary). To proceed to the Rayleigh number in which the measure d is the thickness of the spherical shell, we recommend to multiply our values of Ra by coefficient 0.57 (or divide by 1.75).

In our work we mapped the behavior not only for Ra numbers close to that of the real Earth but also for a wide range of Ra numbers in order to find the characteristic features of each convection mode. The lower Ra modes ($Ra = 1.7 \cdot 10^4$ to $Ra = 10^6$) were run on Hewllet-Packard machines with 128 MB RAM and CPU 75 MHz. To save computational time on computers we used an irregular grid in the tangential direction, which was finer near the boundaries $\theta = 0$, $\theta = \pi$. Complications

were raised at these boundaries due to the axisymmetrical geometry, which creates singular points at the poles $\theta = 0$ and $\theta = \pi$. The solution is to take $\theta = (\epsilon, \pi - \epsilon)$, where ϵ is a small positive number ($\epsilon = \pi/3600$ in our case), and to evaluate a fine grid near the $\theta = 0, \pi$ boundaries.

Even with the irregular grid, the computation of the time evolution of the low-Ra systems required months to reach their attractors, and higher Ra could not carried out past the initial state at all. A breakthrough has come from the use of supercomputers with 375 MHz processors and 391 GB of RAM. This allowed us to acquire large datasets for lower Ra numbers and compute runs with Ra numbers as high as $Ra = 10^{11}$. All the computed runs are shown in Table 3.2.

Rayleigh number	**Grid size**	**θ-grid**	**Sym.i.s.**	**Timesteps**	**Regime**
$1.7 \cdot 10^4$	50×100	irreg	yes	100.000	steady
$1.7 \cdot 10^4$	50×100	irreg	no	80.000	steady
$1.0 \cdot 10^5$	100×300	irreg	yes	300.000	periodic
$1.0 \cdot 10^5$	100×300	irreg	no	3,200.000	chaotic
$5.0 \cdot 10^5$	150×350	irreg	no	2,150.000	chaotic
$1.0 \cdot 10^6$	150×400	irreg	no	2,150.000	chaotic
$1.0 \cdot 10^6$	200×1000	reg	no	270.000	chaotic
$3.0 \cdot 10^6$	270×1300	reg	no	47.000	chaotic
$1.0 \cdot 10^7$	250×1200	reg	no	200.000	chaotic
$1.0 \cdot 10^8$	300×1500	reg	no	220.000	chaotic
$1.0 \cdot 10^9$	400×2500	reg	no	66.000	chaotic
$3.0 \cdot 10^9$	400×2500	reg	no	46.800	chaotic
$5.0 \cdot 10^9$	400×2500	reg	no	10.000	chaotic
$1.0 \cdot 10^{10}$	500×3400	reg	no	41.500	turbulent
$1.0 \cdot 10^{11}$	1100×5100	reg	no	22.500	turbulent

Table 3.2. Attributes for different Ra number runs. The computations were performed on the grid of given size (radial times tangential). θ-grid tells whether the grid in the tangential direction is regular or irregular. Sym.i.s. describes whether initial state is symmetrical or asymmetrical. Timesteps reports the total number of steps for each run, and regime describes the behavior of the system after it leaves its initial state (see Section 3.4.2).

In the case of low Ra number runs we have used two kinds of the initial states, the symmetrical one is :

$$\Theta(r,\theta) = 0.01 \left(\frac{3}{2}\cos^2(\theta) - \frac{1}{2}\right) \sin\left(-\frac{\pi}{\ln(r_n)} \ln(\frac{1-r_n}{r_n r})\right) , \tag{3.49}$$

where $\Theta = T - T_o$ is the temperature deviation from the conductive state (3.48), $r_n = \frac{r_1}{r_2}$, and r_1, r_2 are the radii of the bottom and top boundaries of the shell. We chose $r_1 = 1.00$ and $r_2 = 1.83$.

The second, asymmetrical initial state, has the form

$$\Theta(r,\theta) = 0.01 \left[\frac{3}{2}\cos^2\theta - \frac{1}{2} + \frac{1}{2}\exp\left(-\frac{(\theta-\frac{3}{4}\pi)^2}{4}\right)\right]\left[\sin^2\left(2\pi\frac{r-r_1}{r_2-r_1}\right) + \sin\left(2\pi\frac{r-r_1}{r_2-r_1}\right)\right]. \tag{3.50}$$

The symmetrical initial state was used only in $Ra = 1.7 \cdot 10^4$ and $Ra = 1 \cdot 10^5$ runs. Tests of $Ra = 5 \cdot 10^5$ and $Ra = 1 \cdot 10^6$ indicate that the symmetry was soon broken due to computation errors and the chaotic nature of the system. Therefore, we used the asymmetrical initial state for higher Ra runs.

Relatively few timesteps were sufficient for the first three Ra number runs. The behavior of these systems soon became stable in either a steady or periodic state. Since the convection becomes more complicated for $Ra \geq 10^5$, we needed many more timesteps to study the evolution of the system. The grid size can be chosen small for $Ra \leq 10^6$ so it was possible to compute long time-series. The runs were thus used for investigation the long time evolution of these nonlinear systems with emphasis on finding the attractor attributes of these systems.

Higher Ra number modes require more computational time; from $Ra = 10^6$ we were only able just to leave the initial state. Our main interest was concentrated on the structure of the computed fields (temperature and vorticity); therefore we changed to a regular tangential grid (with higher grid size) in order to have the same spatial resolution in all areas. The regime for these runs (as we can see in Table 3.2) is still chaotic, but there is a qualitative change of the system structure. For example, the high Ra number runs show plumes throughout the computed area, whereas the ultra-high Ra convections result in a kind of layered convection, with very small plumes and a high degree of mixing.

3.4 Deterministic chaos

In Section 3.2.2 we described the system (3.15)-(3.17) of equations which approximates the Earth's thermal convection. Although the equations are relatively simple, with one controlling parameter, the nonlinear advection term $\boldsymbol{v} \cdot \nabla T$ puts them into the fascinating kingdom of nonlinear systems (also called dynamical systems). The erratic behavior of such systems, sometimes extremely simple, sometimes complex and chaotic, has led to the theories of attractors, bifurcation, chaos, and fractals, also known as a theory of deterministic chaos. In the following subsections we will focus on how deterministic chaos methodology can be applied to our thermal convection model. The section will finish with a description of a method for evaluation of the correlation dimension of the attractor which provides qualitative information about the chaoticity of the system.

3.4.1 What is chaos?

Let us consider a system described by a set of nonlinear equations. The variables form a phase (state) space and the time evolution of the system can be described as a trajectory (or a flow line) in this phase space. There can exist points in the phase space that are asymptotically approached by all trajectories from a given neighbourhood. Such stable solutions are called stable nodes (or

point attractors) and the corresponding neighbourhood is called an attracting basin. The opposite to the stable node is a point from whose neighbourhood all the trajectories are repelled. This is an unstable node (or a sink). The third type of a point is called a saddle point, with two manifolds (in 2-D) which divide the area around the saddle point into an attracting domain and a repelling one. Naturally we can find other equilibria, such as circles. In the case of 3-D (or higher) spaces, complex equilibria can be defined. For higher dimensions the attracting basin is simply referred to as the attractor.

One of the most important features of nonlinear systems is their sensitive dependence on the initial condition. Two flows which start from close points can depart exponentially from each other. Small disturbances may have large effects. Therefore we get seemingly random solutions with stationary statistical (stochastic) properties although the system is governed by deterministic laws. For this reason the chaotic behavior of nonlinear systems is often called the deterministic chaos. In systems with high sensitivity to initial values there can exist attractors called strange attractors. We are not able to predict the position of the trajectory on the strange attractor at a given time but we can determine some characteristic structures, which are the same for all points on the attractor. The most common quantity used is the dimension of the attractor.

In dynamical systems the behavior of the system will usually change slightly with a slight change of a controlling parameter. When a qualitative change (jump) in the solution character occurs with a small change in the parameter, we call it a bifurcation. For example, by increasing a parameter a stable node can convert to an unstable one from which two new stable nodes arise (this bifurcation is known as a pitchfork bifurcation), or a stable node can change to a stable circle (Hopf bifurcation).

3.4.2 Routes to chaos

The evolution of a dynamical system with respect to changes of its controlling parameters can pass through a number of different regimes, varying from simple (unique) attractors, strange attractors, or even combinations of both. Here we will consider the characteristic bifurcation sequences which lead to chaos (see, e.g., Drazin, 1992) in many dynamical systems.

Subcritical instability. With a small change of parameter a through a critical value a_c, a simple attractor (such as a point, periodic or quasi-periodic attractor) becomes unstable and the system 'jumps' to a stable strange attractor which is not a continuous extension of the simple attractor. This bifurcation is called subcritical.

A sequence of bifurcations. Transition to turbulence in hydrodynamic systems can occur after an infinite number of bifurcations in complicated quasi-periodic flows as parameter a changes. Moreover, Ruelle and Takens (1971) and Newhouse et al. (1978) conjectured that turbulence would occur after only a few bifurcations, for a quasi-periodic solution with more than three fundamental frequencies. This route to the chaos can be described by:

$$\text{steady} \overset{Hopf}{\longrightarrow} \underset{f_1}{\text{periodic}} \rightarrow \underset{f_1,f_2}{\text{quasi-periodic}} \rightarrow \underset{f_1,f_2,f_3}{\text{quasi-periodic}} \rightarrow \text{chaos}\,,$$

if parameter a varies monotonically.

Period doubling. Period doubling bifurcations occur when an attractor with a closed curve shape changes to two closed curves. Chaos appears after an infinite succession of such period doubling bifurcations.

Intermittent transition. After parameter a passes a critical value a_c, the limit cycle becomes unstable and a new attractor which looks very similar forms. The new attractor has occasional disturbances. With increasing $a - a_c$ the disturbances occur more and more frequently although their magnitudes remains similar.

Some of the above routes to chaos are found in the Lorenz system (Drazin, 1992). Lorenz (1963) studied a model of 2-D convection in a horizontal layer of fluid heated from below. He considered only the three most important terms in the Fourier expansion and obtained a simple nonlinear system of the three variables x,y,z with the three controlling parameters r,b,σ:

$$\frac{dx}{dt} = -\sigma x + \sigma y\,, \tag{3.51}$$

$$\frac{dy}{dt} = rx - y - zx\,, \tag{3.52}$$

$$\frac{dz}{dt} = -bz + xy\,, \tag{3.53}$$

which had complicated and unexpected behavior (Drazin, 1992). For fixed $\sigma = 10$, $b = \frac{8}{3}$ and varying r the Lorenz system embodies a very complicated sequence of bifurcations and attractors. For $0 \le r \le 1$ it has the trivial solution $x = y = z = 0$, and for $1 \le r \le r_o$, $r_o \doteq 24.06$, there are two stable points, $x = y = \pm\left(b(r-1)\right)^{\frac{1}{2}}, z = r - 1$. For $r_o \le r \le r_c$, $r_c \doteq 24.74$ there exist two stable points and a strange attractor. For $r > r_c$ there is only one strange attractor (see Figure 3.1), followed by a sequence of stable limit cycles with or without strange attractors.

Similar complicated sequences can be found in cases of higher dimensional approximations of thermal convection as shown in Figure 3.2. As these approximations were considered only for

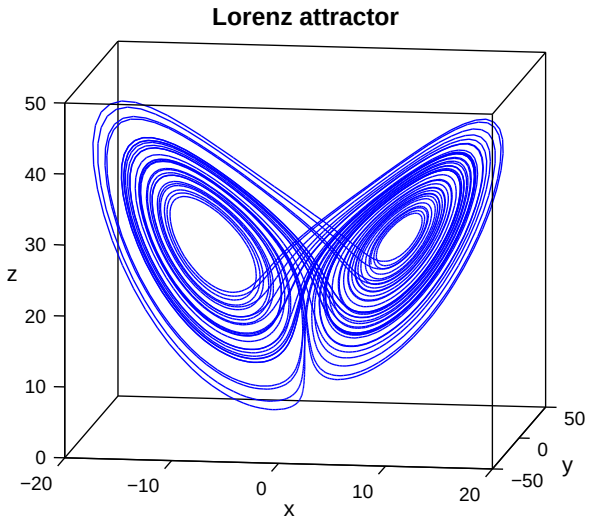

Figure 3.1. A numerical solution of the Lorenz equations (3.51)-(3.53) with $\sigma = 10$, $b = \frac{8}{3}$, $r = 28$.

finite Prandtl number, we can ask what happen if the limit of infinite Prandtl number is taken in the equations describing the thermal convection. In the case of the Lorenz system only stable fixed points are obtained. Stewart and Turcotte (1989) showed that such steady states of Lorenz convection are only artifacts of a too severe truncation, the 12-mode expansion of the equations valid for infinite Prandtl number convection exhibits chaotic solutions for higher Rayleigh numbers. Thus we can also expect a non-trivial evolution of our thermal convection model.

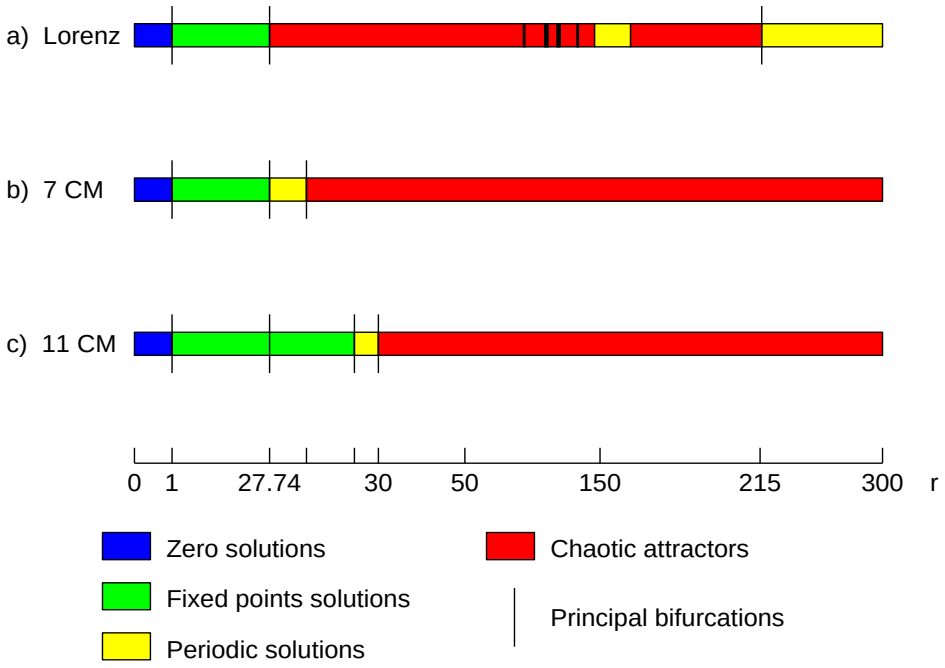

Figure 3.2. Set of schematics illustrating the solution regimes and transitions between solutions in (a) the Lorenz (1963) model, (b) the seven-coefficient Chang and Shirer (1984) model, and (c) the eleven-coefficient model, as the controlling parameter r is varied (source Nese, 1987).

3.4.3 The attractor dimension

As mentioned in Subsection 3.4.1, it is not possible to predict the location on a strange attractor. However, we can determine characteristics of the attractor; the most commonly used is the attractor dimension, which reflects the attractor's complexity and degree of strangeness. The dimension of simple attractors is an integer (zero for points, one for curves etc.), strange attractors have nonintegral dimensions. Roughly speaking, the attractor dimension corresponds to the minimum number of independent variables needed for a full description of the dynamical system.

There exists a variety of dimension definitions (e.g., Nese, 1987; Marek and Schreiber, 1991; Raidl, 1995), based on the metric properties of the attractor (fractal dimension), on the frequency of visits of individual parts of the attractor (information dimension), dimension computed from the Lyapunov exponents (Lyapunov dimension) or based on correlation integral (correlation dimension). For simple attractors all dimensions yield the same value, for strange attractor they can vary in

the nonintegral part of their value.

The correlation dimension has one important advantage in comparison with the other dimensions. It does not require analysis of either the governing equations (which can be rather complex), nor the dataset describing the trajectory in the phase space. We just need a time-series of the phase variable or some combination of several phase variables. This is the reason why we have chosen the correlation dimension in the case of our thermal convection modelling.

The computation of the correlation dimension is based on the reconstruction of the phase space (e.g. Marek and Schreiber, 1991).
Take a time-series $x(t_\mathrm{i})$. Create a new m-dimensional signal $\boldsymbol{X}^\mathrm{m}(t_i)$ from the time-series,

$$\boldsymbol{X}^\mathrm{m}(t_\mathrm{i}) = x(t_\mathrm{i}), x(t_\mathrm{i}+\tau), \ldots, x(t_\mathrm{i}+(m-1)\tau)\,, \tag{3.54}$$

where τ is an appropriate time delay and m is an embedding dimension. The correlation integral is then computed as follows:

$$C^\mathrm{m}(r) = \lim_{n\to\infty} \frac{1}{n(n-1)} \sum_{\substack{i,j=1 \\ i\neq j}}^{n} H\left(r - ||\boldsymbol{X}_\mathrm{i}^\mathrm{m} - \boldsymbol{X}_\mathrm{j}^\mathrm{m}||_{L_2}\right)\,, \tag{3.55}$$

where $||\,.\,||_{L_2}$ means L_2 norm, and $H(r)$ is the Heaviside function, $H(r)=0$ for $r<0$ and $H(r)=1$ for $r\geq 1$.
Continue the procedure with increasing embedding dimension m until the correlation integral (3.55) is almost constant for increasing m (so called reconstruction of the phase space). The dimension of the reconstructed attractor is the same as that of the original attractor.

The definition (3.55) counts the points close (in sense of radius r) to a given point in the reconstructed space and then averages over all these points. If the attractor is a simple curve, then $C^\mathrm{m}(r)\sim r^1$, if it is a surface, $C^\mathrm{m}(r)\sim r^2$, etc. We thus consider the correlation dimension ν as the slope of the log-log graph of $C(r)$ versus r, or

$$\log C^\mathrm{m}(r) = \nu \log r + \mathrm{const}\,, \qquad r\to 0\,. \tag{3.56}$$

In the next paragraphs we would like to mention some problems when computing the correlation dimension. More complex information (with references) can be found in, e.g., Raidl (1995).

Time delay τ, see (3.54). In the case of infinite noise-free time-series the time delay may be chosen arbitrarily. When using finite time-series, the time delay cannot be too small (otherwise we get attractor states very close to a diagonal in the reconstructed phase space, which reflects in under-dimensioned estimation of the correlation dimension). On the second hand, the time delay cannot be chosen too high to preserve the large influence of noise in the signal. Also high time delay automatically means lower size of the new created signal (3.54). The usual choice of the time delay τ is the time when the autocorrelation function of the time-series first becomes zero.

Elimination of too close points in the reconstructed phase space. Time correlation of temporally close points causes anomaly structure of the correlation integral (3.55). Thus in the sum

in the definition (3.55) only points with temporal differences larger then τ_0 are allowed. Condition for τ_0 (Raidl, 1995):

$$\tau_0 \geq \tau \left(\frac{2}{N}\right)^{\frac{2}{m}} , \tag{3.57}$$

where τ is the time delay, N is the number of data points in the original one-dimensional signal and m is the embedding dimension.

Determination of the slope of the $\log C(r)$ versus $\log r$ curve. The correlation dimension ν is in practice obtained as the slope in the $\log C(r)$ versus $\log r$ graph (see (3.55)) for r from some interval $< r_{\min}, r_{\max} >$. For r less than $r_{\min}$ there is a lack of the points and for r greater than $r_{\max}$ we count also points from nearby folds of the attractor. There is no theoretical prescription how to determine the bounds $r_{\min}$ and $r_{\max}$. Frequent method is a computation of the local slope

$$\nu_1(r) = \frac{d \ln C(r)}{d \ln r} \tag{3.58}$$

or the slope given by Theiler (1990)

$$\nu_2(r) = \frac{C(r)}{\int_0^r [C(\tilde{r})/\tilde{r}] d\tilde{r}} , \tag{3.59}$$

and finding the correlation dimension ν as a minimum of $\nu_1(r)$ or $\nu_2(r)$ on some meaningful interval.

The length of the signal. Many formulae determining a minimal number of data points $N_{\min}$ for a reliable estimate have been established. Some of them are very strict or erroneous, the $N_{\min}$ can be often smaller for a good estimation of the attractor dimension, it depends on signal noise, type of the attractor, complexity of the signal and others.
Thelier (1990) gives estimates of the minimal length of the signal with an error less than 5% for determination of the correlation dimension. If the local slope method (3.58) is used, the estimate is

$$N_{\min} \geq 5^m \tag{3.60}$$

and for dimension determined from (3.59), the minimal length of the signal is :

$$N_{\min} \geq (1.25)^m , \tag{3.61}$$

where m is the embedding dimension.

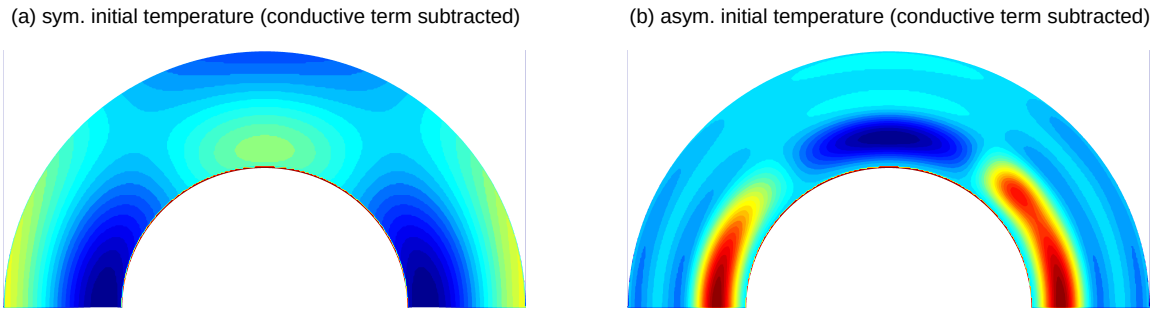

Figure 3.3. Initial temperature deviation, (a) is symmetrical case, see the definition (3.49), (b) slightly asymmetrical case, see (3.50). The blue color in the colormap has a temperature deviation $-1 \cdot 10^{-2}$, the red color has a value of $2 \cdot 10^{-2}$.

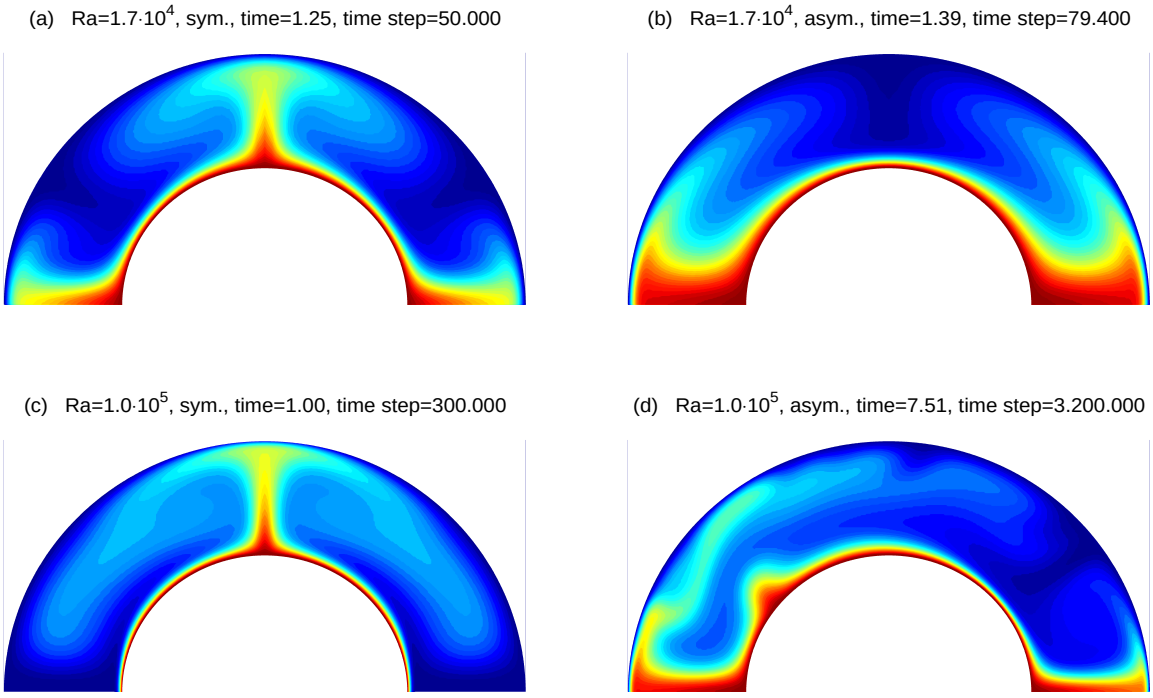

Figure 3.4. Absolute temperature (with conductive term) for low Rayleigh numbers. (a) $Ra = 1.7 \cdot 10^4$ started with symmetrical initial temperature, (b) $Ra = 1.7 \cdot 10^4$ started with asymmetrical initial temperature, (c) $Ra = 10^5$ started with symmetrical initial temperature and (d) $Ra = 10^5$ started with asymmetrical initial temperature.

3.5 Thermal convection for different Rayleigh numbers

We have divided convection runs with different Ra numbers (see Table 3.2) into the four main parts: low Ra runs with Ra varying from $1.7 \cdot 10^4$ to 10^5, intermediate Ra runs with Ra ranging from 10^5 to 10^6, high Ra runs with Ra between 10^6 to 10^{10} and ultra-high Ra runs for $Ra = 10^{10}$ and higher. The low Ra convection runs have very simple structure in physical space (see temperature in Figures 3.4), characterized by a few convection cells, with wide and stable upwellings and downwellings; the runs reach simple attractors. The intermediate Ra runs still have simple physical structure but their time evolution is chaotic. The high Ra runs (Figures 3.17a-c) have more complex structure in physical space. Their plumes are layered and elongated, and secondary instabilities appear. However, the mixing is not powerful enough to destroy mantle plumes (up- and downwellings) before they pass through the whole mantle. The last section, ultra-high Ra convection (Figure 3.17e), contains the runs with very turbulent behavior, powerful mixing and very complex small-scale structures.

3.5.1 Low Rayleigh number convection

The $Ra = 1.7 \cdot 10^4$ run

The system with low Rayleigh number is simple and requires only a small grid size (see Table 3.2). The runs computed on the supercomputers (see Subsection 3.3) did not need long computational times, and the systems reached simple attractors. In this case we focused on finding attractors for different initial conditions. We have chosen two initial temperature states, one tangential symmetrical (Figure 3.3a) and one tangential asymmetrical (Figure 3.3b). The temperatures in the figures are the temperature deviation with conductive profile (3.48) subtracted from the total temperature.

For low Ra number, such as $Ra = 1.7 \cdot 10^4$, convection for both initial states reached a simple steady attractor (Figures 3.4a-b). There are four convection cells (see Figure 3.4a) in the case of the symmetrical initial temperature and two convection cells (see Figure 3.4b) in the case of asymmetrical one. We had expected that the simplicity of the low parameter system should reflect in a small number of convective cells. We tested this by preparing a third run, with the symmetrical initial temperature perturbed by a weak plume on the right side. The amplitude of the perturbation was about 1% of the symmetrical initial temperature. This run evolved into a two convection cell system as expected from the asymmetrical runs.

We compare the evolution of these three systems by studying global (or semi-global) quantities, such as the (total) kinetic energy defined as

$$W = \int_{r_1}^{r_2} \int_{0}^{\pi} \boldsymbol{v} \cdot \boldsymbol{v}\, r^2 \sin\theta \, d\theta \, dr \tag{3.62}$$

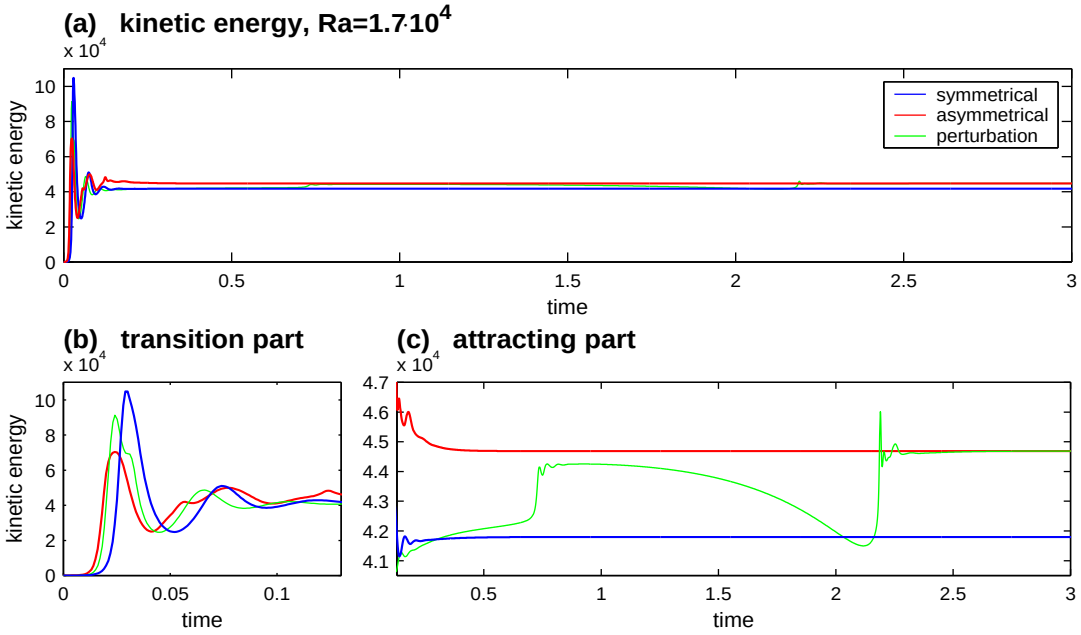

Figure 3.5. Kinetic energy for $Ra = 1.7 \cdot 10^4$. There are three initial temperature conditions: symmetrical, asymmetrical and symmetrical with a weak perturbation. Panel (a) shows the time-dependent kinetic energy, (b) the first timesteps where transition occurs, and (c) the attracting section where the kinetic energy is relatively constant.

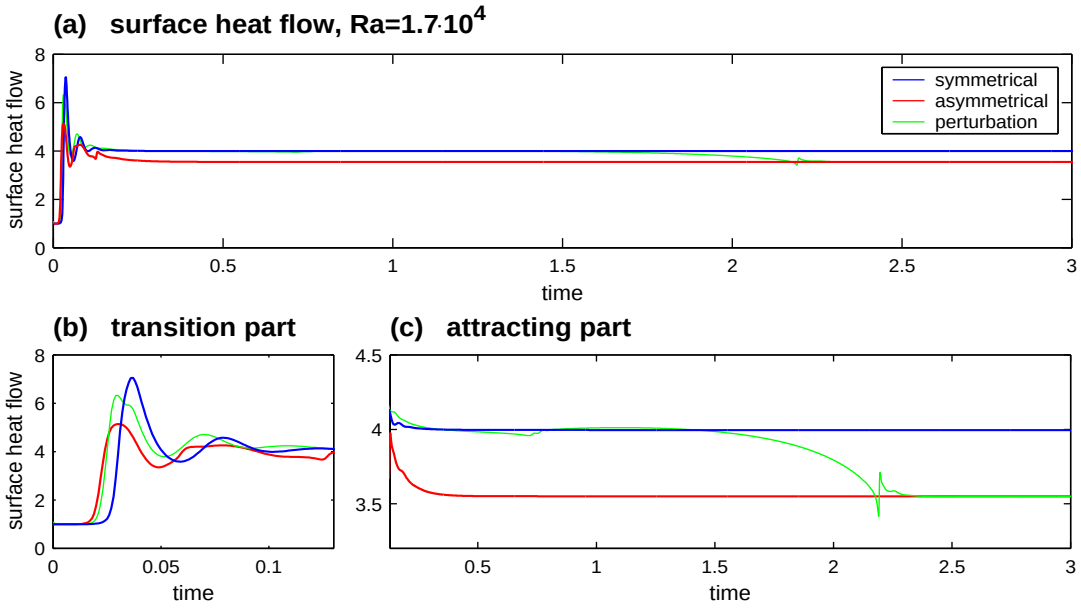

Figure 3.6. Surface heat flow for $Ra = 1.7 \cdot 10^4$, the panels are the same as for the kinetic energy (Figure 3.5).

and the Nusselt number,

$$Nu = -\frac{(r_2 - r_1)r_2}{2r_1} \int_0^{\pi} \frac{\partial T}{\partial r}\Big|_{(r=r_2)} \sin\theta \, d\theta, \tag{3.63}$$

where r_1 and r_2 are radii of the shell bottom and top.
The Nusselt number measures the efficiency of the convection over conduction in the heat transform across the mantle, $Nu(r) = \int_0^{\pi} \frac{\partial T}{\partial r} \sin\theta d\theta / \int_0^{\pi} \frac{\partial T_o}{\partial r} \sin\theta d\theta$, where T_o is the conductive temperature (3.48). We will deal only with $Nu(r_2)$ (often called shortly the surface heat flow), so we expect higher influence of the Nusselt number from the events close to the surface; while deeper events will influence this quantity less and with some time delay.

Time dependencies of the kinetic energy and the surface heat flow are shown in Figure 3.5 and Figure 3.6, which depict the two steady-state attractors of the low Rayleigh number systems. The system, which started from the symmetrical initial temperature (blue line), finished with lower kinetic energy and higher surface heat flow than the system which started from the asymmetrical initial temperature (red line). Note that differences between the symmetrical and asymmetrical value are not that large in comparison with values obtained from systems with higher Rayleigh number (see Table 3.4, page 61).

To study the perturbed symmetrical run we zoomed-in on the transition and attracting section of the time-series of the kinetic energy (Figures 3.5b-c) and the surface heat flow (Figures 3.6b-c). We can see in the transition panels (Figure 3.5b, Figure 3.6b) that the perturbation time-series (green) has similar behavior as the symmetrical time-series (blue) except that they are out of phase. The attracting section (Figure 3.5c, Figure 3.6c) shows slow convergence of the perturbation time-series. The convergence is associated with sudden jumps (two in the case of the kinetic energy and one in the case of the surface heat flow), and it takes a relatively long time to reach the true attractor. Hence, we can see two major trends specific to low Rayleigh number convection. First, although the low Rayleigh number system looks simple in the physical space, the mixing is not powerful, and one must be aware that a long time may be needed to reach the final attractor. Second, the surface heat flow, which is only a semi-global quantity, is not as sensitive to the behavior of the system as the kinetic energy. The first jump seen in the kinetic energy time-series is not visible at all in the case of the surface heat flow.

The $Ra = 10^5$ run

The system, which started from the symmetrical initial temperature, results in two convection cells with the major upwelling plume in the center of the shell (Figure 3.4c). However, the convection is not steady any more and the central hot plume periodically changes its strength, which is reflected in the periodic character of the kinetic energy (Figure 3.7a) and the surface heat flow (Figure 3.7b) time-series.

The behavior of the system, which started from the asymmetrical initial temperature, is, surprisingly, much more complicated. In principle, there are still two convection cells in the shell (see Figure 3.4d). The aspect ratio of the left cell is about four, which leads to the periodic generation of instabilities in the lower and upper boundary layers. The hot (red) instabilities are then attracted

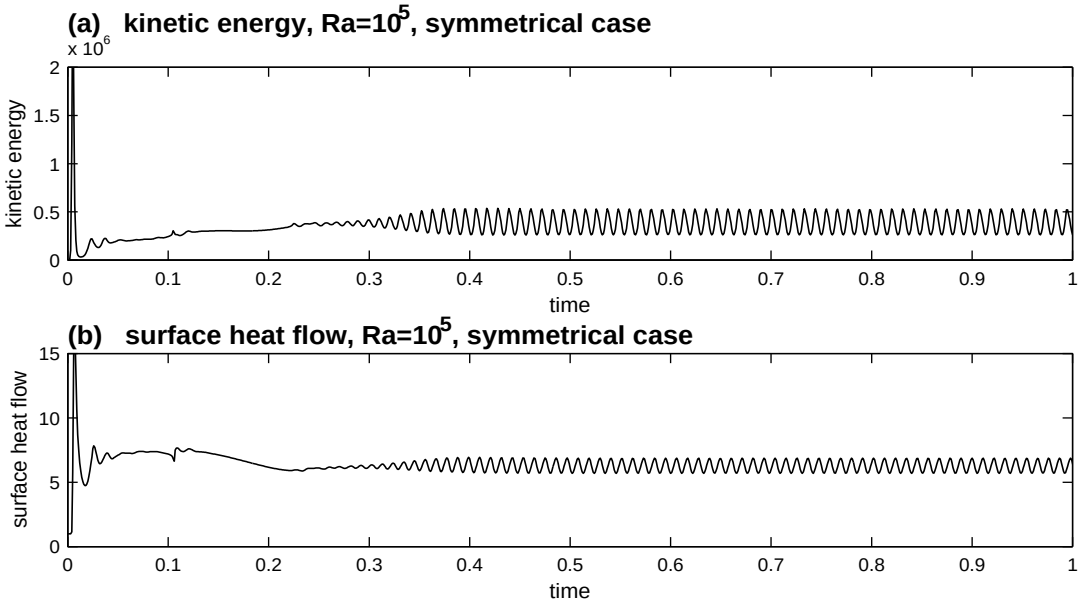

Figure 3.7. Time-dependent kinetic energy (a) and surface heat flow (b) for $Ra = 10^5$ and symmetrical initial temperature.

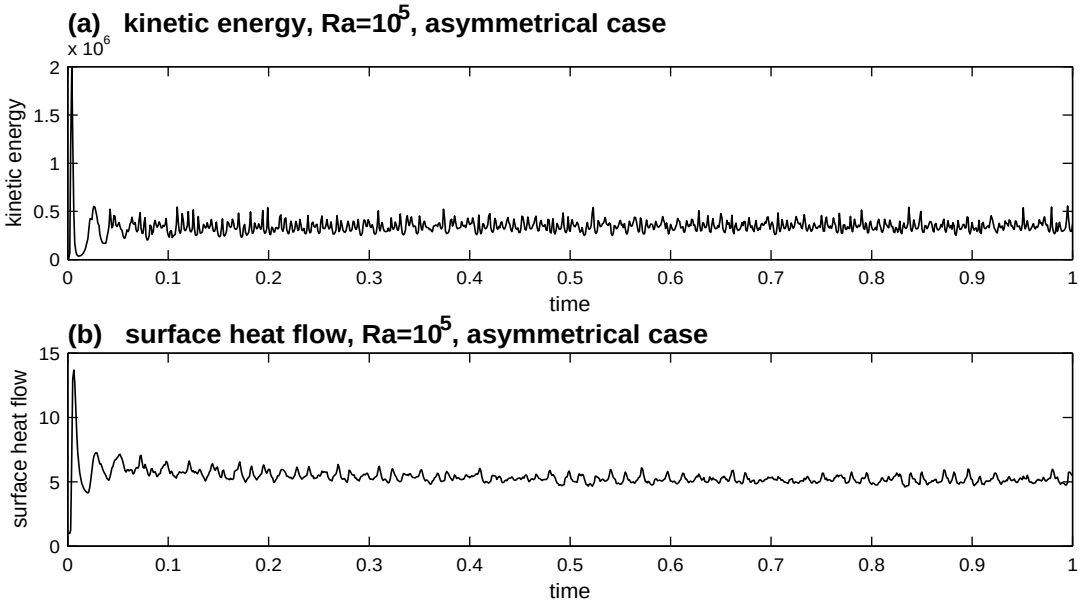

Figure 3.8. Time-dependent kinetic energy (a) and surface heat flow (b) for $Ra = 10^5$ and asymmetrical initial temperature.

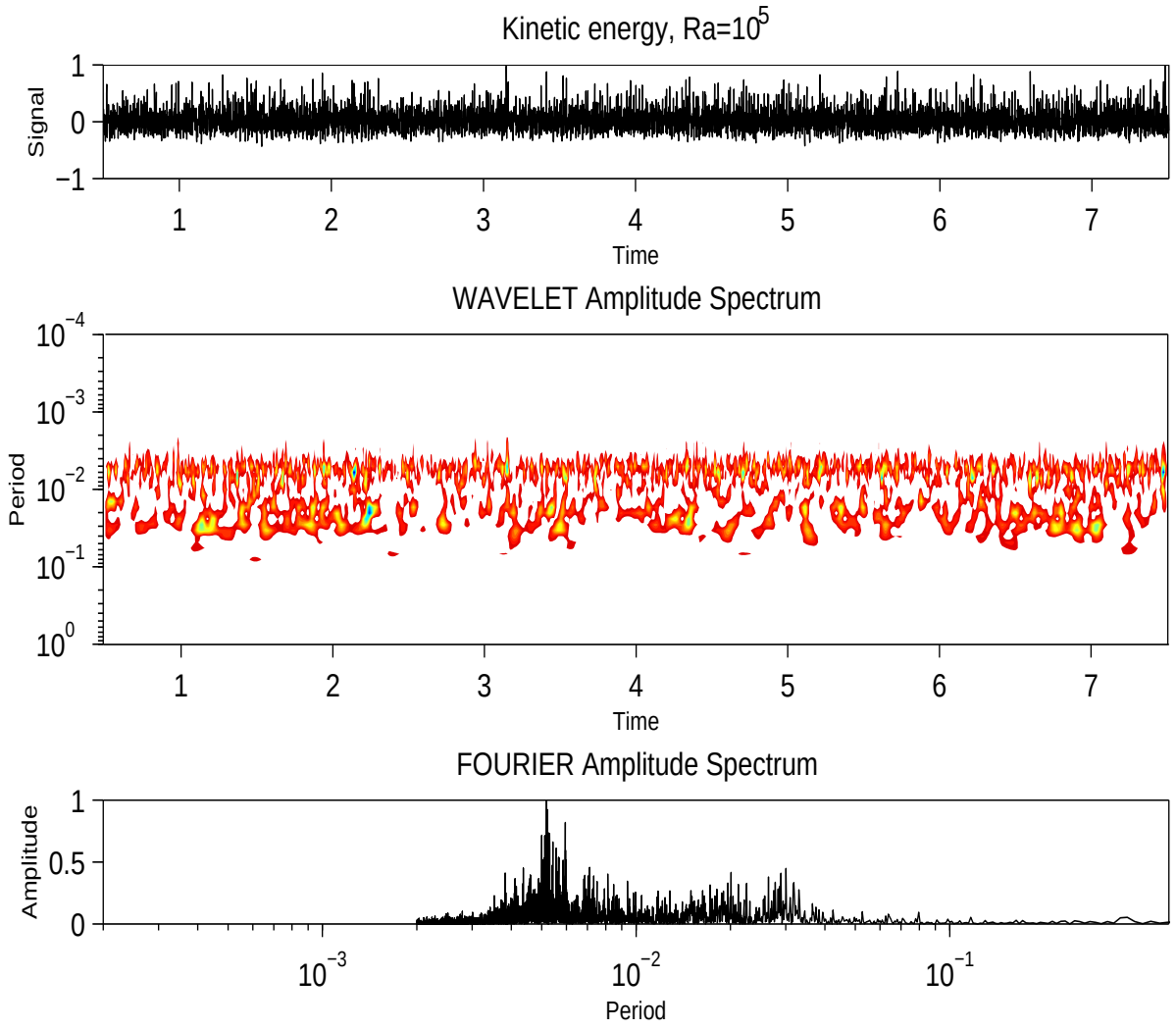

Figure 3.9. Kinetic energy fluctuations for $Ra = 10^5$, asymmetrical run. The top panel shows the studied time-series. Zero corresponds to its average value (see Table 3.4, page 61); the series is normalized by its maximum value. The time-series for $t < 0.5$ was excluded from the analysis to eliminate the influence of the transition state. The middle panel shows the wavelet spectrum of the series, the horizontal axis is the time and the vertical axis is the Fourier period recomputed from the wavelet scale (formula (2.10)). Colormap varies from red, which corresponds to 1/16 of the wavelet spectra maximum, through yellow and green to blue, belonging to the maximum value of the wavelet amplitude scale. The last panel displays the amplitude of the Fourier spectrum of the signal.

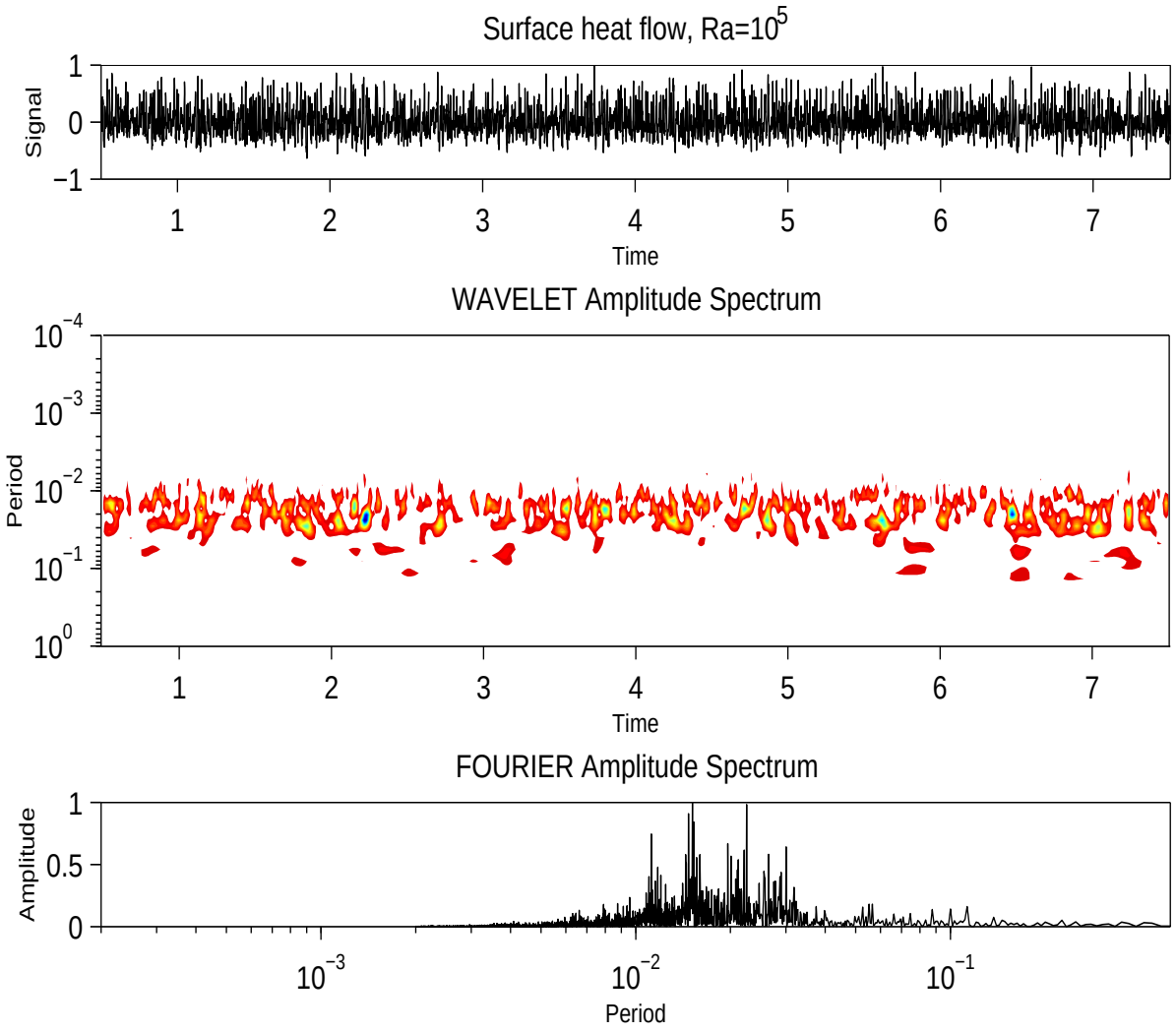

Figure 3.10. Surface heat flow for $Ra = 10^5$, asymmetrical run. The top panel shows the studied time-series. Zero corresponds to its average value (see Table 3.4, page 61); the series is normalized by its maximum value. The time-series for $t < 0.5$ was excluded from the analysis to eliminate the influence of the transition state. The middle panel shows the wavelet spectrum of the series, the horizontal axis is the time and the vertical axis is the Fourier period recomputed from the wavelet scale (formula (2.10)). Colormap varies from red, which corresponds to 1/16 of the wavelet spectra maximum, through yellow and green to blue, belonging to the maximum value of the wavelet amplitude scale. The last panel displays the amplitude of the Fourier spectrum of the signal.

to the major plume and the cold (blue) instabilities end their lives by merging with the major downwelling.

We have just described short-time events in this convective system. Long-time events also exist here, mostly connected with motion of the major downwelling, which separates the shell into the two cells. After the time of about 0.05, when the strongest changes of the system are over, the downwelling plume slowly shifts from about 110 degrees in tangential direction (measured from the left pole) to an angle of about 150 degrees. The dimensionless time related to the plumes right-hand motion is about 0.5. This transition can be also seen in Figure 3.8b, where the surface heat flow exhibits descending values till the time of 0.5. We remark that the time-dependent kinetic energy (Figure 3.8a) is not as suitable for finding this long-time behavior as the surface heat flow since the major downwelling shift is connected mostly with the top part of the shell, and the kinetic energy is not as sensitive to this process as the surface heat flow.

We consider 0.5 as the overall time at which the systems reach their attractor. As we can see from Figure 3.7, the symmetrical system of $Ra = 10^5$ reaches its attractor at a time of about 0.4. In the asymmetrical system, two convection cells persist from a time of about 0.5, the larger left one with downwelling and upwelling instabilities, the smaller right one with simple round motion and with intermittent major downwelling at the tangential position of 150 degrees (see Figure 3.4d). The kinetic energy and the surface heat flow time-series (Figure 3.8) vary only in the small-scale; the mean values are mentioned in Table 3.4, page 61. We have used a 1-D wavelet transform (2.1) with the Morlet mother wavelet (2.9) for the time-frequency analysis of the time-series.

One can see in Figure 3.9 that the kinetic energy of the flow is very sensitive to the behavior of the boundary layer instabilities with short characteristic time-scales. We expect that the small-period layer (with main period of about 0.005) in the wavelet spectrum corresponds to these boundary layer instabilities; whereas the large-period layer (periods 0.02-0.03) is connected with major downwelling motion. Comparing the wavelet spectrum with the Fourier spectrum we are able to reveal not only prevailing periods of the kinetic energy time-series but also its strongly fluctuating time-dependent character with places of intensive oscillations and places with weak or no oscillations. One of the first areas of calm occurs for times 2.3-3.2. The same calm area is also seen in the surface heat flow wavelet spectrum. Both the wavelet spectrum and the Fourier spectrum of the surface heat flow fluctuations (Figure 3.10) show an interesting feature: the shortest time-scales, with periods lower then 0.01, are not significant. This probably corresponds to the diffusion character of heat transfer at the surface were damping of the surface heat fluctuations generated by oscillatory behavior inside the convecting layer increases with decreasing characteristic times of the processes. Therefore the wavelet spectrum shows only one layer of dominant periods.

We emphasize that the prevailing characteristic times in Figure 3.9 and Figure 3.10 are associated with strongly fluctuating quantities throughout the evolution of the system, which points to the existence of complicated dynamics in the boundary layers. To get more information about this system, we computed the correlation dimension of the system attractor.

The correlation dimension for $Ra = 10^5$, asymmetrical case

We used the reconstruction of the phase space to find the correlation dimension as described in Subsection 3.4.3. The code which computes the correlation integral $C^{\mathrm{m}}(r)$ (3.55) and the correlation dimension ν (3.56) as the slope of the log-log graph of $C^{\mathrm{m}}(r)$ was successfully tested on the Lorenz time-series (see the Lorenz attractor in Figure 3.1, page 32); the dimension agreed with the Lyapunov dimension of 2.06 published by Nese (1987).

The correlation integral $C^{\mathrm{m}}(r)$ was computed from the time-series of the two quantities: total kinetic energy (Figure 3.8a) and the surface heat flow (Figure 3.8b). We removed the initial part (times 0-0.5) from the time-series so that only the stages on the attractor were considered. The time delay τ used in the m-dimensional signal $\boldsymbol{X}^{\mathrm{m}}$ (see (3.54)) was chosen as the first time when the autocorrelation function of the given time-series reaches zero. To eliminate points too close in the reconstructed phase we excluded points with time delays less than τ_0, see equation (3.57). The correlation integrals are plotted on log-log graphs in Figure 3.11. As we mentioned in Subsection 3.4.3, the correlation dimension is determined from the middle (low-slope) part of the curve, which is not influenced by a lack of points (for low r) or by a nearby folds of the attractor (for high r). While the correlation integral computed from the kinetic energy (Figure 3.11a) preserves middle low-slope part of the curve (marked by the red circle in Figure 3.11a) for increasing embedding dimension m, this low-slope part dissipates in the case of the correlation integral computed from the surface heat flow (see the blue circle in Figure 3.11b).

The correlation dimensions ν determined from the correlation integral $C^{\mathrm{m}}(r)$ are shown in Figure 3.12. We have used two methods: the local slope (3.58) marked by the solid line and the Theiler formula (3.59) marked by the dash line. Both methods give similar values. During the computation of the correlation dimensions there occured problems with insufficient length of the signal. We did not have an estimation of the dimension before doing the computation, so we could

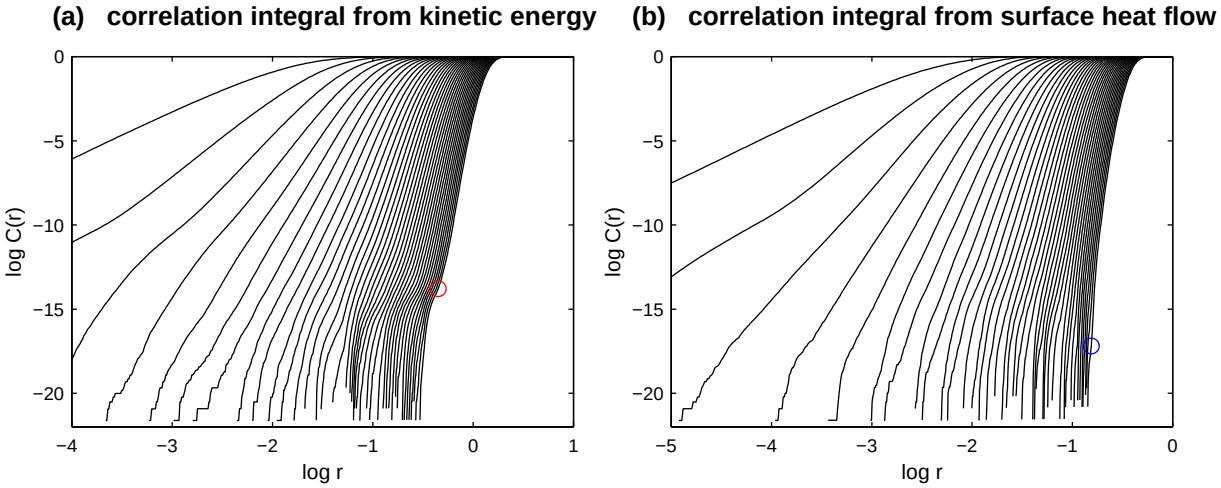

Figure 3.11. Correlation integral $C^{\mathrm{m}}(r)$ (3.55) computed from (a) the kinetic energy and (b) the surface heat flow time-series. Time-series are taken from the time 0.5 to 7.5 and the length of the signal is 70,000 points. There is a difference of 3 embedding dimensions between each curve, the extreme right one was computed for the embedding dimension $m = 120$. The red and blue circles indicate the low-slope part of the curve from which the correlation dimension was computed.

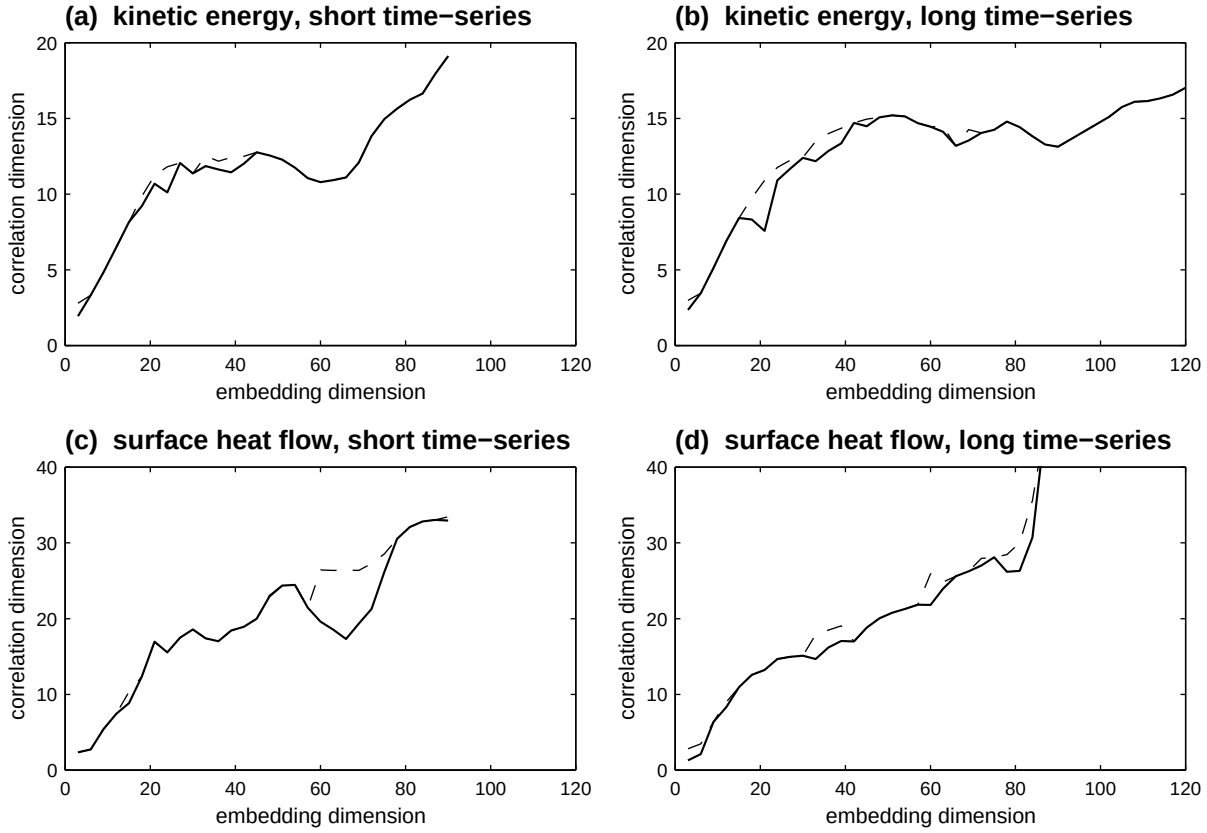

Figure 3.12. Correlation dimensions ν determined from the kinetic energy time-series (a)-(b) and the surface heat flow (c)-(d). The solid line corresponds to the correlation dimension computed from the the local slope (3.58), and the dashed line was computed from the Theiler formula (3.59). Short time-series (time 0.5-3.9) were used in panels (a) and (c), and long time-series (time 0.5-7.5) were used in panels (b) and (d)

not use formulae (3.60) or (3.61). Moreover, with resampling of the original time-series we could create signals of arbitrary length. In the first attempt to compute correlation dimension we used time-series from time 0.5 to 3.9. The length of the signal after resampling was 69,160 timesteps. Neither the dimension computed from the kinetic energy (Figure 3.12a), nor the dimension from the surface heat flow (Figure 3.12c) emboded a visible saturation. The second computation of the correlation dimension was performed with time-series to the time 7.5. The correlation dimension obtained from the kinetic energy (Figure 3.12b) saturated at approximately 14 but the dimension from the surface heat flow was still not saturated. We assume that we have used a time-series long enough for the kinetic energy (which is a global quantity); while the semi-global quantity, surface heat flow, still needs longer signal for a good estimation of the correlation dimension.

The extracted correlation dimension for $Ra = 10^5$ is surprisingly high if we take into account that the system has a relatively simple structure (two convection cells with local up- and down-wellings in the left cell) but the time behavior of flow intensities is close to the chaotic.

3.5.2 Intermediate Rayleigh number convection

In the previous subsection, we have shown that while the $Ra = 1.7 \cdot 10^4$ runs and the run $Ra = 10^5$ with symmetrical initial temperature reached simple attractors (steady or periodic ones), the 1-D wavelet analysis of the time-series and the correlation dimension of the attractor of the $Ra = 10^5$ system with asymmetrical initial temperature indicate rather complex time evolution of the system. We will concentrate on systems with relatively simple physical structure but complex time evolution in this section.

The systems which started from symmetrical initial temperature conditions with Rayleigh numbers higher than 10^5 are too unstable to keep their symmetry; the symmetry is lost due to numerical errors during computation. We consider only the asymmetrical initial case in the next sections.

The $Ra = 5 \cdot 10^5$ and $Ra = 10^6$ runs

These systems still embody two cell convection (compare Figure 3.4d and Figure 3.17a). The aspect ratio of the bigger cell (left one) decreases with higher Ra, for example, it is about 3 in the case of $Ra = 10^6$ convection. Secondary up- and downwellings arise in both cells.

We can expect more powerful mixing for higher Ra numbers, the kinetic energy and the surface heat flow time-series (Figure 3.13 and Figure 3.14) pass through the transition state faster and faster. The mean values (see Table 3.4, page 61) of the both quantities increase with higher Ra, but there is also an increase of the mean kinetic energy deviations, from 14% for $Ra = 10^5$ to 31% for $Ra = 10^6$. However in the case of the surface heat flow the deviations are only 8% and 9%, respectively.

The wavelet spectra of the kinetic energy and the surface heat flow time-series for $Ra = 5 \cdot 10^5$ (Figure 3.15) and $Ra = 10^6$ (Figure 3.16) have the same global versus semi-global quantity pattern as in the case of $Ra = 10^5$ (Figures 3.9-3.10). While the global kinetic energy also has significant short-period components, the semi-global surface heat flow preserves most of the power in the large-scale part of the spectrum. The time behavior of the large-scale wavelet spectra of the kinetic energy and the surface heat flow are similar in the shape but different in the magnitudes of the wavelet spectrum peaks.

The wavelet and Fourier spectra for all three Ra numbers: 10^5, $5 \cdot 10^5$ and 10^6 exhibit a very similar range of significant periods. The first spectrum maximum peak appears in the range of the periods $2 - 8 \cdot 10^{-3}$; the second one, which is higher in the case of the surface heat flow, appears approximately between the periods of $2 - 13 \cdot 10^{-2}$. Moreover, an investigation of the Fourier spectra for our three Ra numbers reveals transfer of the power, from small scales ($Ra = 10^5$) to large scales ($Ra = 10^6$).

We would like to note that the time-series for $Ra = 5 \cdot 10^6$ is shorter than that for $Ra = 10^5$, so the correlation dimension method, which was described in Section 3.4.3 and used for $Ra = 10^5$, is not applicable. Also the large-scale part of the wavelet and Fourier spectra may be influenced by the inadequate length of the time-series.

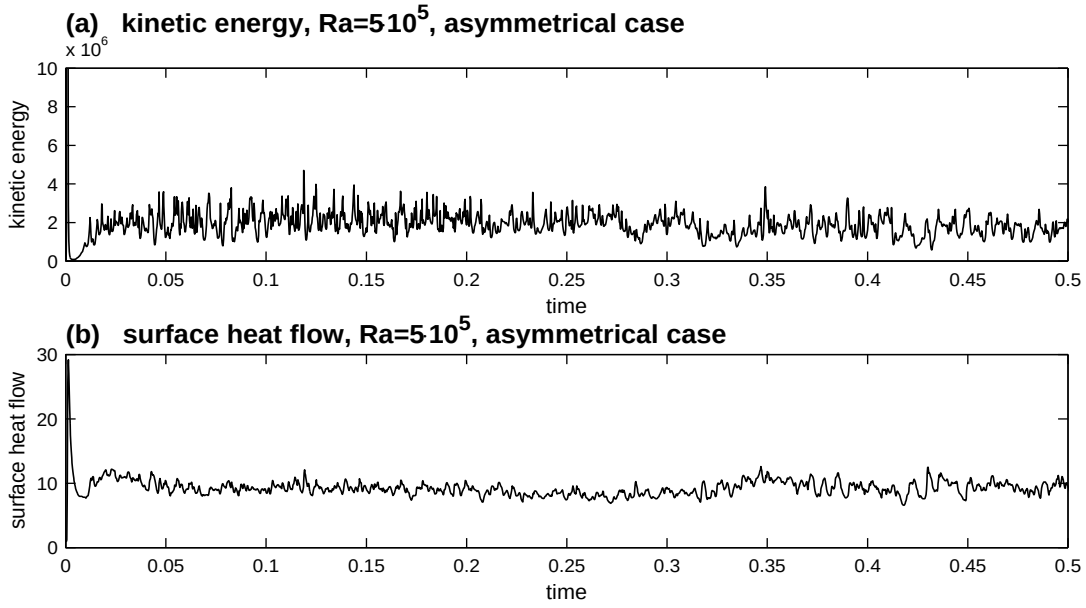

Figure 3.13. Time-dependent kinetic energy (a) and surface heat flow (b) for $Ra = 5 \cdot 10^5$ and asymmetrical initial temperature.

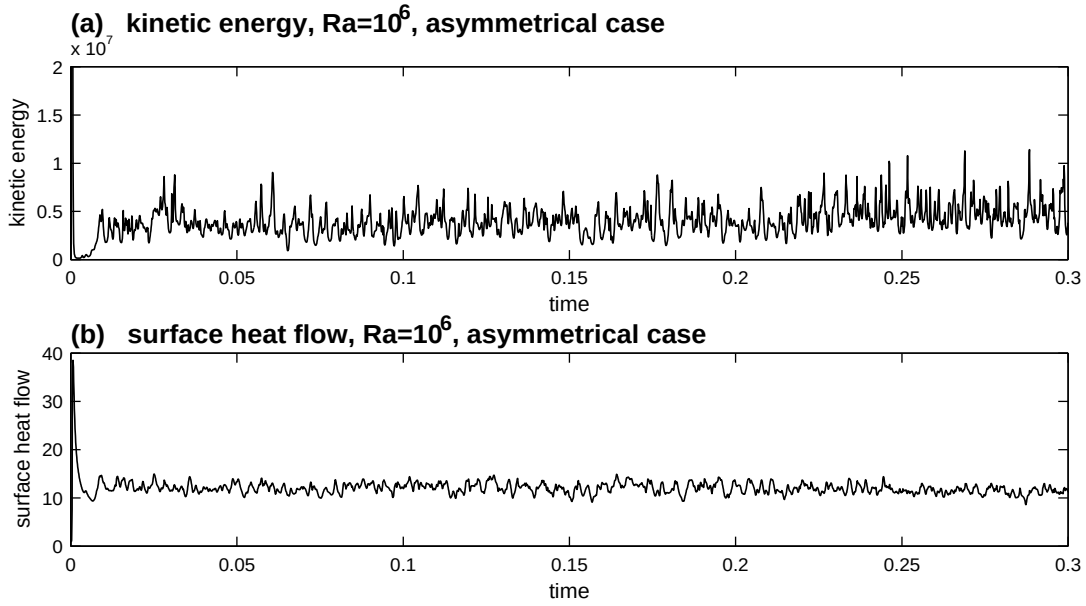

Figure 3.14. Time-dependent kinetic energy (a) and surface heat flow (b) for $Ra = 10^6$ and asymmetrical initial temperature.

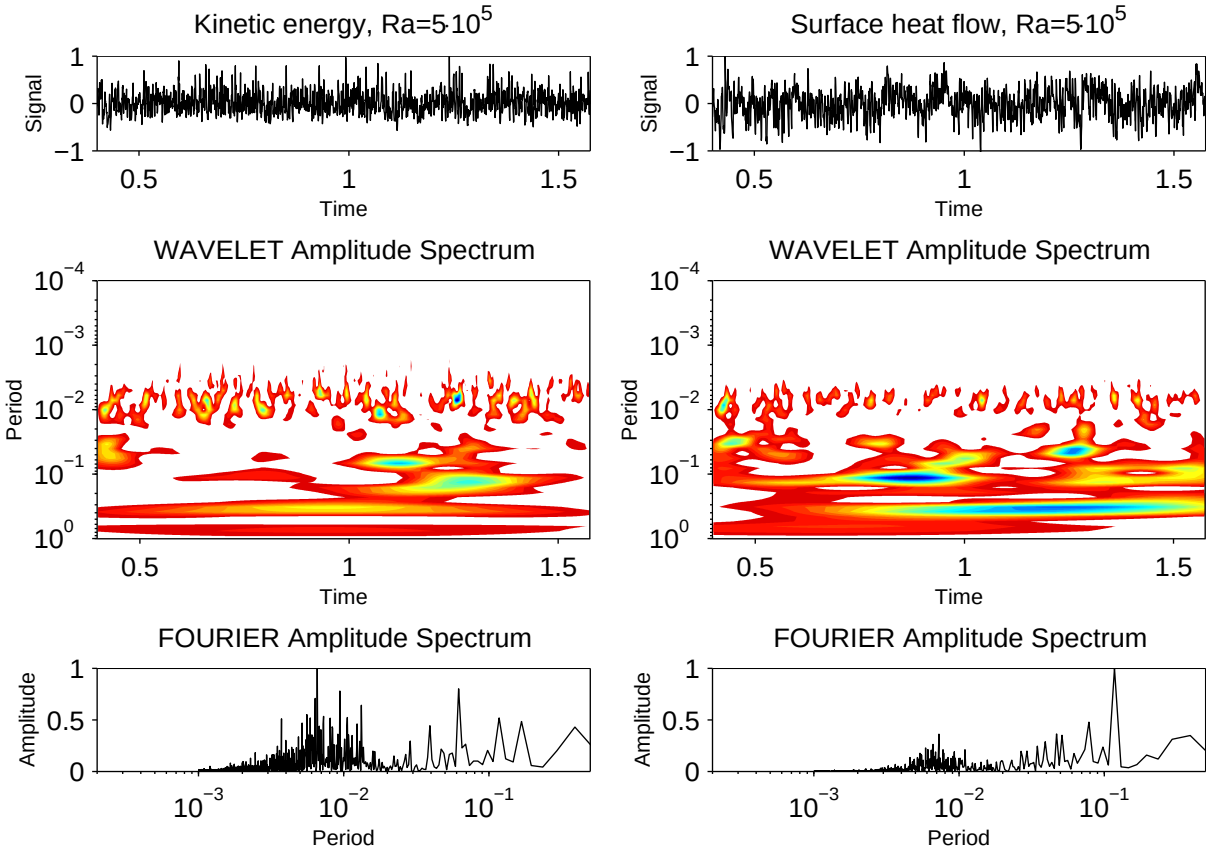

Figure 3.15. Kinetic energy fluctuations and surface heat flow for $Ra = 5 \cdot 10^5$, asymmetrical run. The top panels show the studied time-series. Zeros correspond to their average values (see Table 3.4, page 61); the series are normalized by their maximum values. The time-series for $t < 0.4$ were excluded from the analysis to eliminate the influence of the transition state. The middle panels show the wavelet spectra of the series, the horizontal axes are time and the vertical axes are the Fourier periods recomputed from the wavelet scales (formula (2.10)). Colormap varies from red, which corresponds to 1/16 of the wavelet spectra maximum, through yellow and green to blue, belonging to the maximum value of the wavelet amplitude scale. The last panels show the amplitudes of the Fourier spectra of the signals.

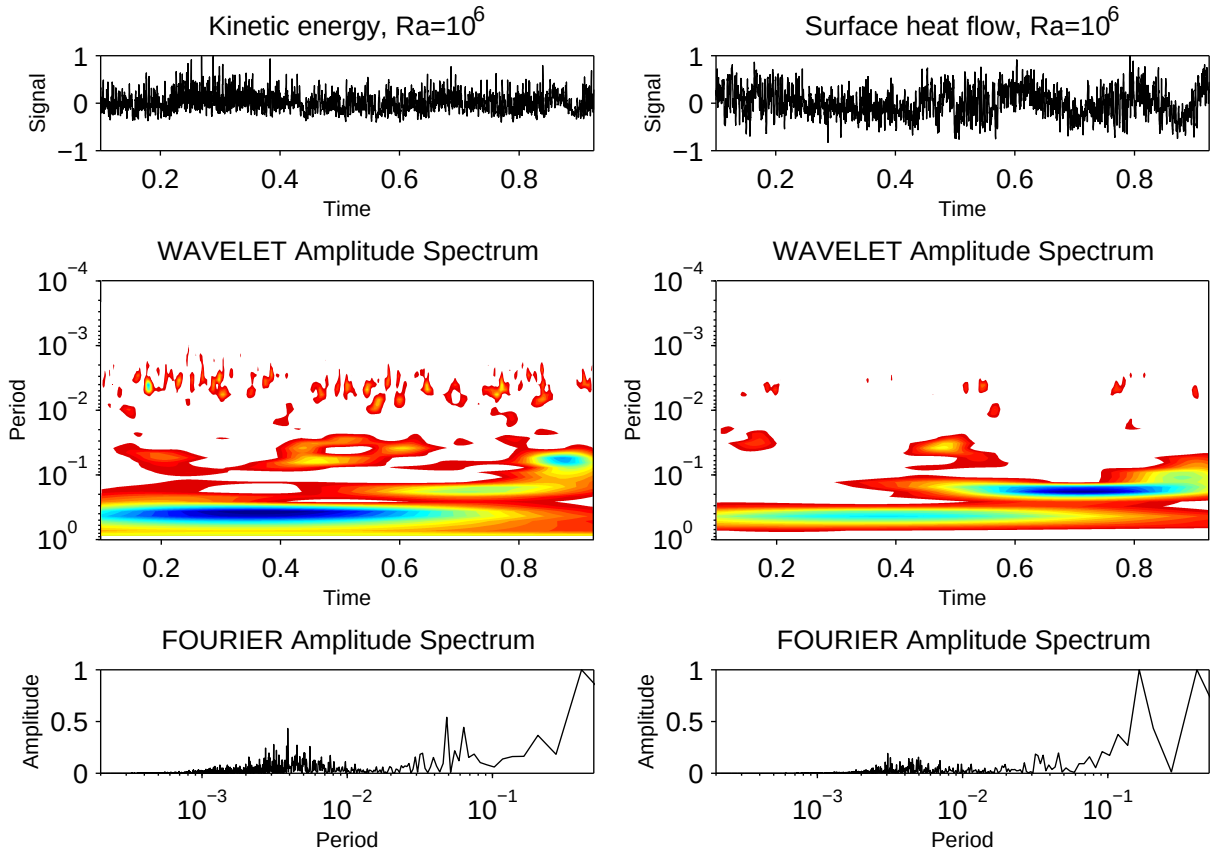

Figure 3.16. Kinetic energy fluctuations and surface heat flow for $Ra = 10^6$, asymmetrical run. The top panels show the studied time-series. Zeros correspond to their average values (see Table 3.4, page 61); the series are normalized by their maximum values. The time-series for $t < 0.1$ were excluded from the analysis to eliminate the influence of the transition state. The middle panels show the wavelet spectra of the series, the horizontal axes are time and the vertical axes are the Fourier periods recomputed from the wavelet scales (formula (2.10)). Colormap varies from red, which corresponds to 1/16 of the wavelet spectra maximum, through yellow and green to blue, belonging to the maximum value of the wavelet amplitude scale. The last panels display the amplitudes of the Fourier spectra of the signals.

3.5.3 High Rayleigh number convection

As the Rayleigh number is increasing further, the systems show increasingly complex behavior in both their time evolution and spatial structure of the temperature and vorticity fields (see temperature pictures in Figure 3.17). The wavelet analysis of the fields for different scales is described in Section 4.3. Here we focus on finding the space characteristics that prevail throughout the given range of Ra numbers. We do not have time-series for these high Ra numbers long enough to perform temporal analysis. The computation of high Rayleigh number convection requires high computer memory and times and so the runs were continued only to the time at which we were sure that the systems had left their transient regimes. Then we located the main characteristics of the system's attractor, and we were able to compute the mean values of the kinetic energy and the surface heat flow from the time-series (the mean values are listed in Table 3.4, page 61).

Although computed in a spherical-shell geometry, the figures of temperature fields will be displayed in Cartesian domain (by means of a Cartesian mercator projection) in the following sections. The space structure of high-Ra systems is quite complex and we prefer obtaining a little geometrical distortion due to Mercator projection than to have small pictures, which are more difficult to see.

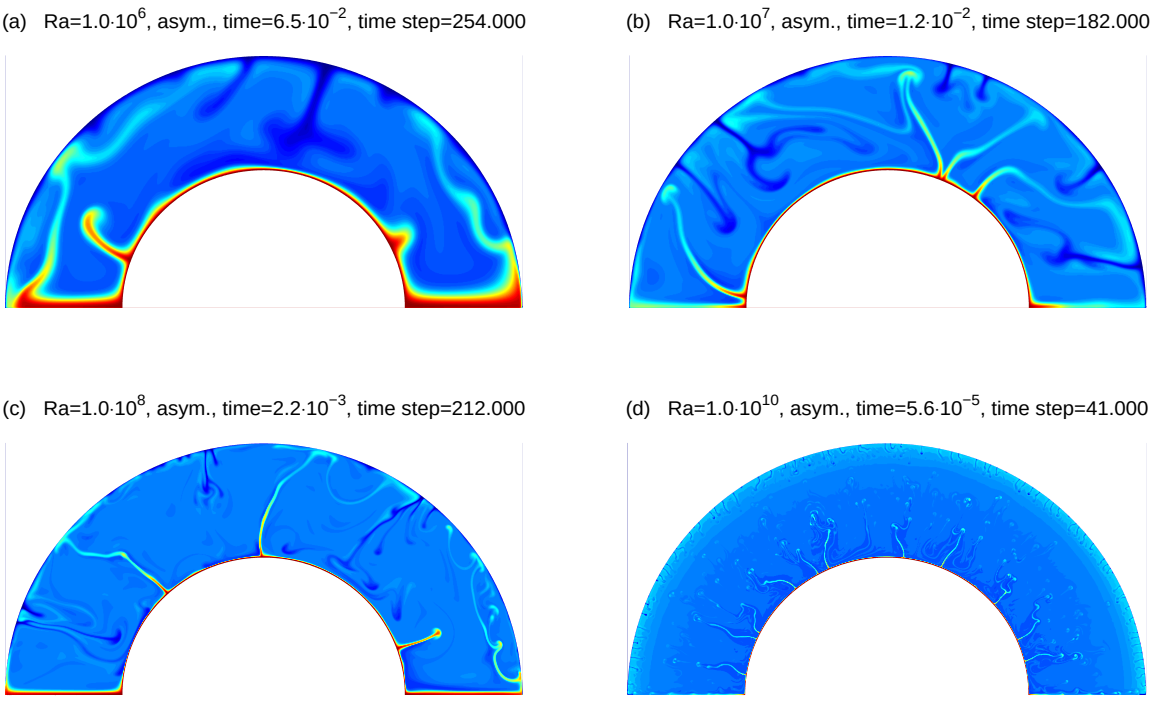

Figure 3.17. Absolute temperature (with conductive term) for high Rayleigh numbers.

The $Ra = 10^6$ run

We will show a character of the $Ra = 10^6$ convection on the examples of four different time stages, see Figure 3.18. The thermal convection still keeps two major convection cells and the main downwelling stays in the azimuth of about 100°. The opposite parts of the convection cells, hot upwellings, lie on the edges of the spherical shell (azimuths 0° and 180°). The convection is powerful enough to enable raising of the local instabilities inside the cells. The hot upwellings are attracted to the edges (see Figure 3.18a) and could downwellings to the center major instability. The plumes are still thick relatively to the size of the shell, the plume heads occurs only when the convection is locally still (as in the Figure 3.18c). The other effect of the large plume thickness and less powerful mixing are long plume tails, which are reflected in the hot waving remains in the upper part of the shell (Figure 3.18b). We remark that these objects look very similar to the Whitehead instabilities (see Section 3.5.5) but they are not true ones, they occur only as the result of collision of the plume tail with the upper boundary.

The last temperature field in Figure 3.18d shows a first attempt at to create more convection

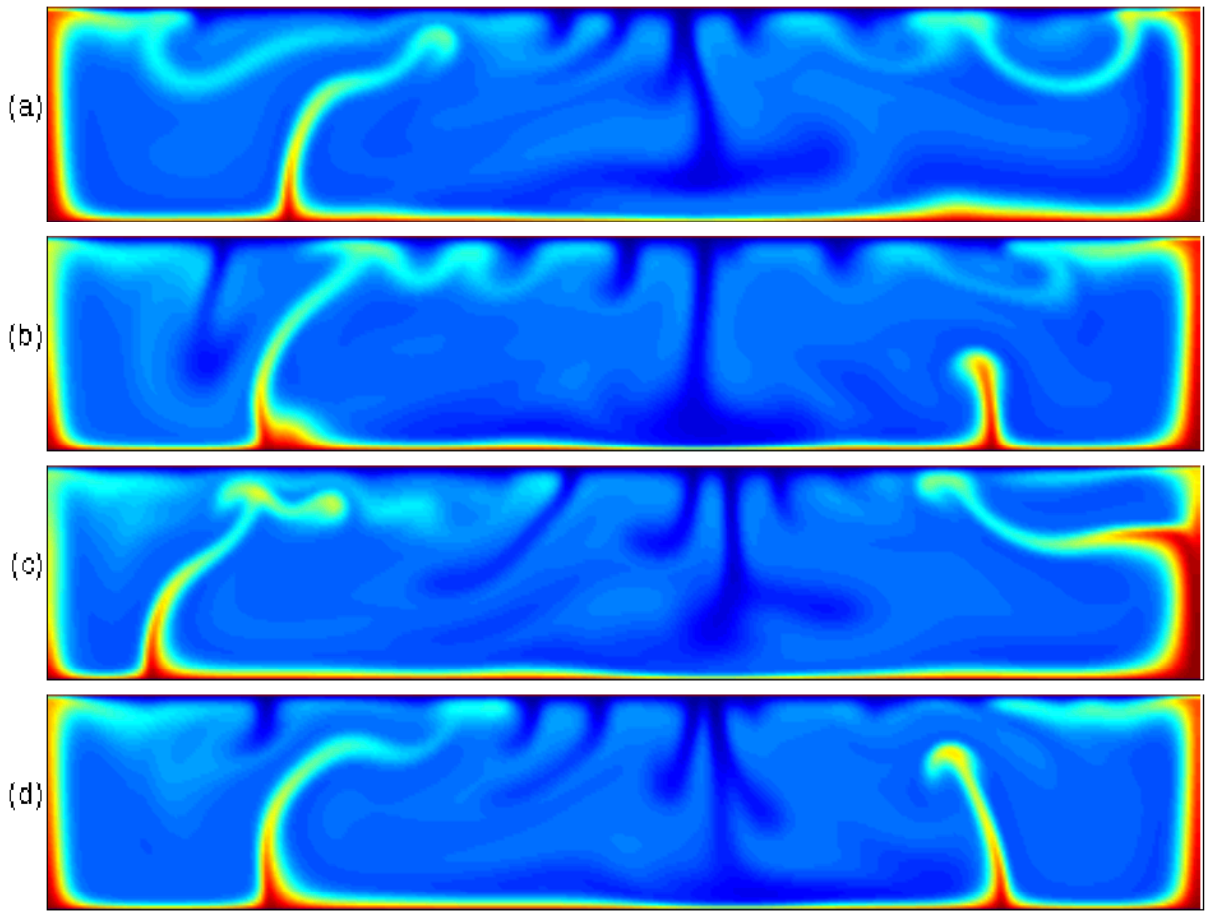

Figure 3.18. Absolute temperature field (with conductive term) for $Ra = 10^6$ in Cartesian projection. There are four states: (a) dimensionless time 0.0018 and timestep 71.500. (b) time 0.024 and timestep 92.000. (c) time 0.044 and timestep 170.000. (d) time 0.064 and timestep 251.000.

cells. The collision between hot upwellings and small cold downwellings on the left side of the picture is a bridge to the more complicated behavior, visible in next runs.

The $Ra = 10^7$ run

The convection at such high Rayleigh number no longer has two cells. (A detailed study of the number of the convection cells can be found in Section 4.3.) In comparison with the $Ra = 10^6$ case, the bending of the plume tails is not so frequent (Figures 3.19a-d). This feature corresponds to absence of the very large convection cells, in which local instabilities were attracted to the edge main plumes and their fast movement produced bended tails. The example of the perfect straight upwelling can be seen in the Figure 3.19a, on the left-hand side. Also plume heads start to occur, see Figures 3.19c-d.

Examining Figure 3.19b, we can observe the same bending of of the plumes remaining at the top of the shell as in the case of $Ra = 10^6$; a new feature what we find is a change between up- and

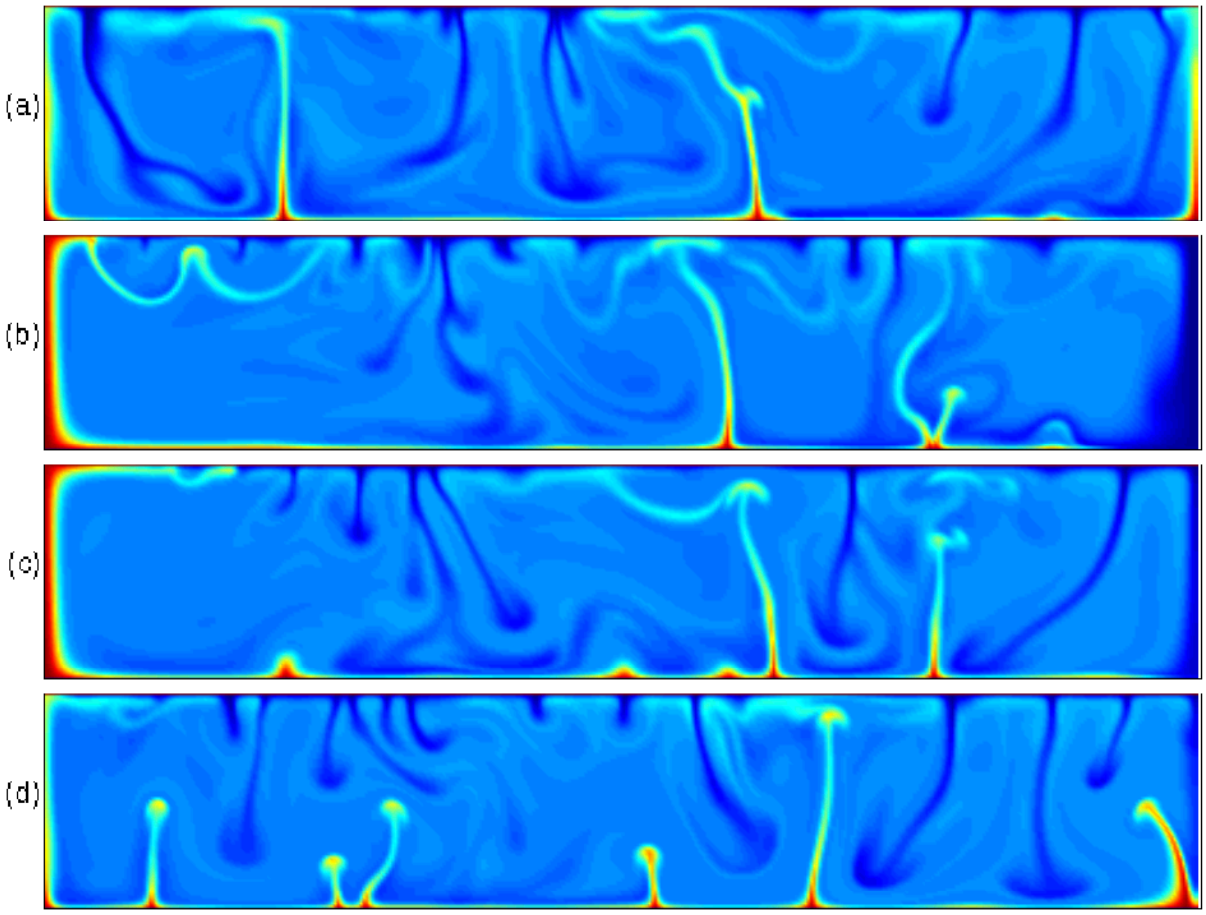

Figure 3.19. Absolute temperature field (with conductive term) in Cartesian projection. There are four states from the $Ra = 10^7$ run: the panel (a) shows the temperature for the dimensionless time 0.0084 and timestep 130.000, the panel (b) for the time 0.0093 and timestep 140.000, the panel (c) for the time 0.0096 and timestep 141.000 (d) time 0.0109 and timestep 143.000.

downwellings on the shell edges. The four displayed time stages in Figures 3.19 show reversing of the plume on the right-hand side of the shell.

The very complicated relations between up- and downwellings in the $Ra = 10^7$ convection are caused by the relatively large thickness and robustness of the plumes, together with mixing that is not powerful enough to prevent most up- and downwellings from going through the whole mantle without disturbance. In Figure 3.19c, we can see such a collision of the downwelling head and the upwelling root (on the right-hand side) or the downwelling jammed between neighbouring upwellings.

If we count a number of upwellings, we are surprised that there are about 3-4 whole mantle plumes, which is of the same order as in the $Ra = 10^6$ convection. Only when young plumes appear (Figure 3.19d), the total number of the plumes rise.

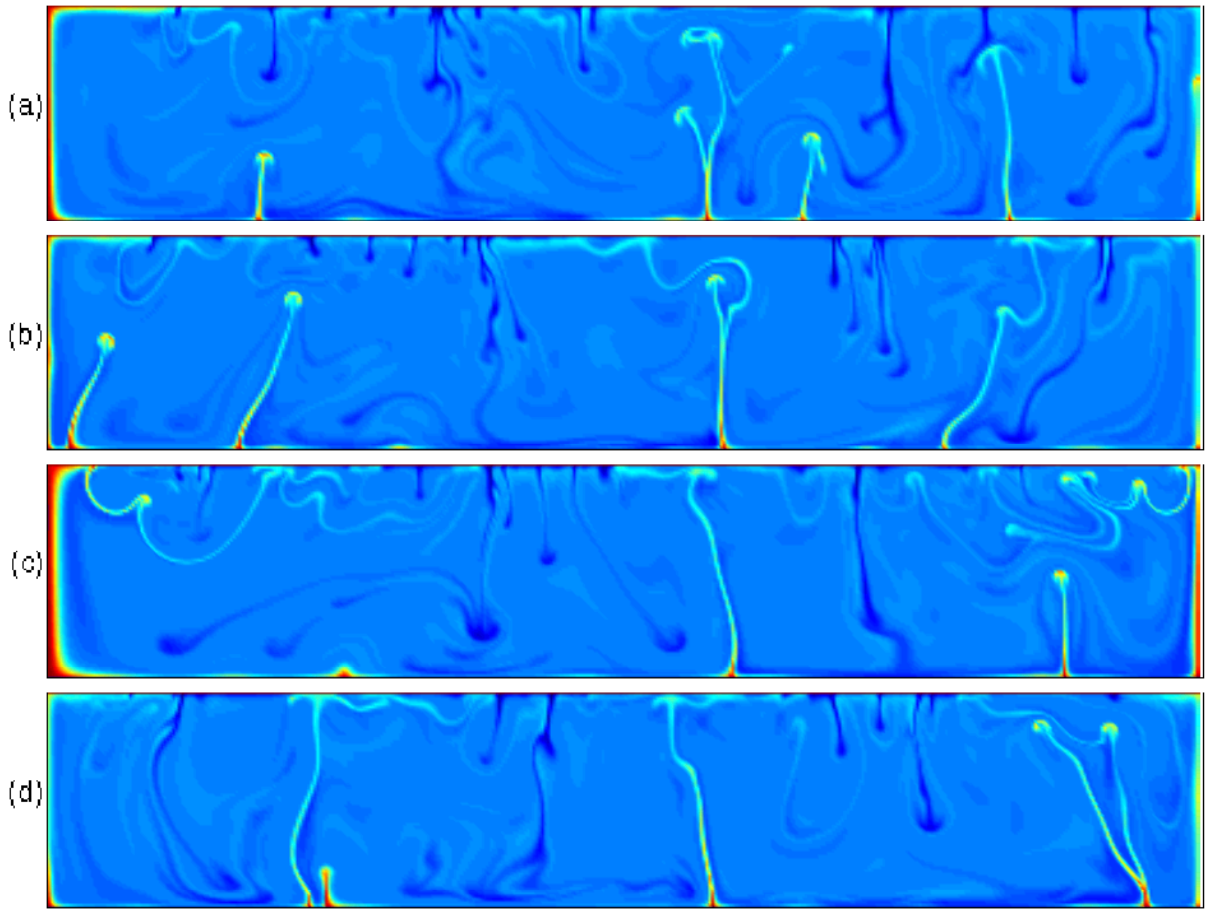

Figure 3.20. Absolute temperature field (with conductive term) for $Ra = 10^8$ in Cartesian projection. There are four states: (a) dimensionless time $6.4 \cdot 10^{-4}$ and timestep 80.000. (b) time $14.6 \cdot 10^{-4}$ and timestep 152.000. (c) time $15.7 \cdot 10^{-4}$ and timestep 162.000. (d) time $20.1 \cdot 10^{-4}$ and timestep 202.000.

The $Ra = 10^8$ run

The convection system of $Ra = 10^8$ is still characterized by whole mantle plumes; moreover, there exist plumes stable for longer time periods (see upwellings at an azimuth about 100^o in Figure 3.20), even for high degree of mixing belonging to convection at this Rayleigh number.

The plumes are narrow, straight, and have well-developed heads, which is caused by much the greater rising speed of the plumes in comparison with the background motion. The collisions between up- and downwellings still persist (Figure 3.20a, the plume on the right-hand side), and another very frequent feature is bending and branching of the plumes (Figures 3.20a,c-d). The formation of new plumes from a bent one (so-called Whitehead instabilities) will be further investigated in the following section.

The behavior of the system for $Ra = 10^8$ remains qualitatively the same as in the previous cases. Higher Rayleigh number convections reflected in thinner plumes that can still get through the whole mantle. Also a number of whole mantle plumes remained relatively small. We can say that changes due to increasing Rayleigh number are continuous, without any jumps.

3.5.4 Ultra-high Rayleigh number convection

During our investigation of the thermal convection, which is a nonlinear system controlled by the Rayleigh number, we have also touched on convection at ultra-high Rayleigh numbers, such as $Ra = 10^{10}$ and $Ra = 10^{11}$. Difficulties with extreme requirements on computation time and computer memory are compensated by a look into a new and still not very well explored part of the thermal convection regime. Moreover, we are motivated by an effort to get an as large as possible ensemble of convective systems in order to study, how convective behavior depends on Rayleigh number.

The $Ra = 10^{10}$ run

Previously we have seen how $Ra = 10^{10}$ reveals a new convective regime (compare Figures 3.17a-c with Figure 3.17d). The relatively small number of whole mantle plumes in the case of high Rayleigh numbers is replaced by a band of small plumes which can rise only to a certain height in the case of ultra-high Rayleigh numbers. We chose temperature at four timesteps (Figure 3.21) to show snapshots of the time evolution of the system. To prevent long computation of the transition regime we used the last temperature state from the $Ra = 10^8$ run as an initial state for $Ra = 10^{10}$ run.

An example of the transition regime is shown in Figure 3.21a. The medium is highly mixed and the first 'baby' plumes arise at the bottom and the top of the convection shell. The characteristic width of the plumes is so small that we are almost not able to recognize lateral plumes on the left and right pole of the shell. The other product of the system geometry, the greater width of the downwellings over the upwellings, is not also obvious. The only visible and easily noticed feature of the spherical shell geometry is a different length of the up- and downwellings. In Figure 3.21b, the medium is better mixed and the mean length of the up- and downwellings is larger than in the previously displayed timestep. The progress of the plumes is shown in Figure 3.21c, where

we also can find the remains of the first generation of plumes (especially upwellings), which can even reach the opposite side of the shell. The last temperature field (Figure 3.21d) illustrates the stage where plumes achieve their maximum (average) height; the high magnitude the mixing causes plume curving and prevents them from growing straight.

Another interesting feature in the temperature field for the $Ra = 10^{10}$ run is the strong temperature inversion in the shell top (Figure 3.21a). It is the remainder of the rapid injection of the mass during transition regime, and we can see its partial disappearance in the next timesteps (Figures 3.21b-d). A more detailed analysis of the mixing of the temperature field is presented in Section 4.3; here we only note that the mixing is no longer characterized by convection in whole-mantle cells but in much smaller ones. That is why the mixing is very powerful at the small scales but the large-scale phenomena, such as the liquidation of the warm area in the top of the shell, take much more time than in the case of lower Ra runs. For more analysis of the vertical temperature profiles for different Ra runs see Section 3.5.6.

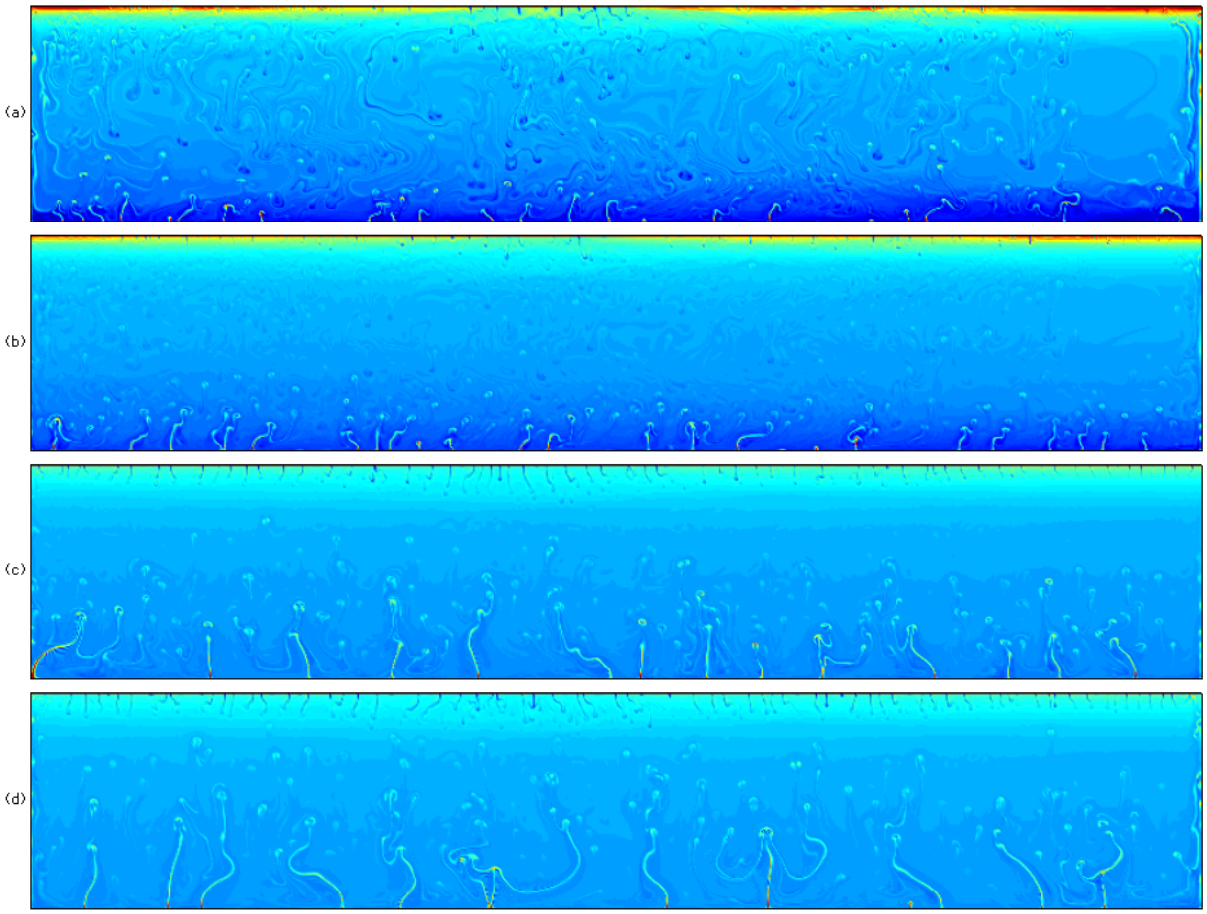

Figure 3.21. Absolute temperature field (with conductive term) for $Ra = 10^{10}$ in Cartesian projection. Four states are shown: (a) dimensionless time $0.9 \cdot 10^{-5}$ and timestep 14.000. (b) time $1.8 \cdot 10^{-5}$ and timestep 19.000. (c) time $4.4 \cdot 10^{-5}$ and timestep 31.000. (d) time $5.4 \cdot 10^{-5}$ and timestep 40.000. To improve the visibility of the complex small-scale structures in the temperature field the colormap was chosen as follows: the colormap is linear for temperatures $0 - 0.8$ with colors changing from blue through green and yellow to red; all temperatures higher than 0.8 are displayed only in red.

The $Ra = 10^{11}$ run

The highest Rayleigh number convection was computed on a grid-size of 1100×5100. Despite of such fine resolution numerical instabilities still occured (see waving ares near fast moving plumes in the Figure 3.22). The large requirements of computer memory and the long computation time are the reasons why the $Ra = 10^{11}$ run has not yet been finished; the system has not left its transition state yet. The transition state (shown in Figure 3.22) is very similar to the $Ra = 10^{10}$ one, with the same inversion of the temperature (especially by the hot layer in the top), with a highly mixed middle part of the shell and new 'baby' plumes rising along the top and bottom. Therefore we expect that the $Ra = 10^{11}$ convection belongs to the qualitatively same regime as $Ra = 10^{10}$ run.

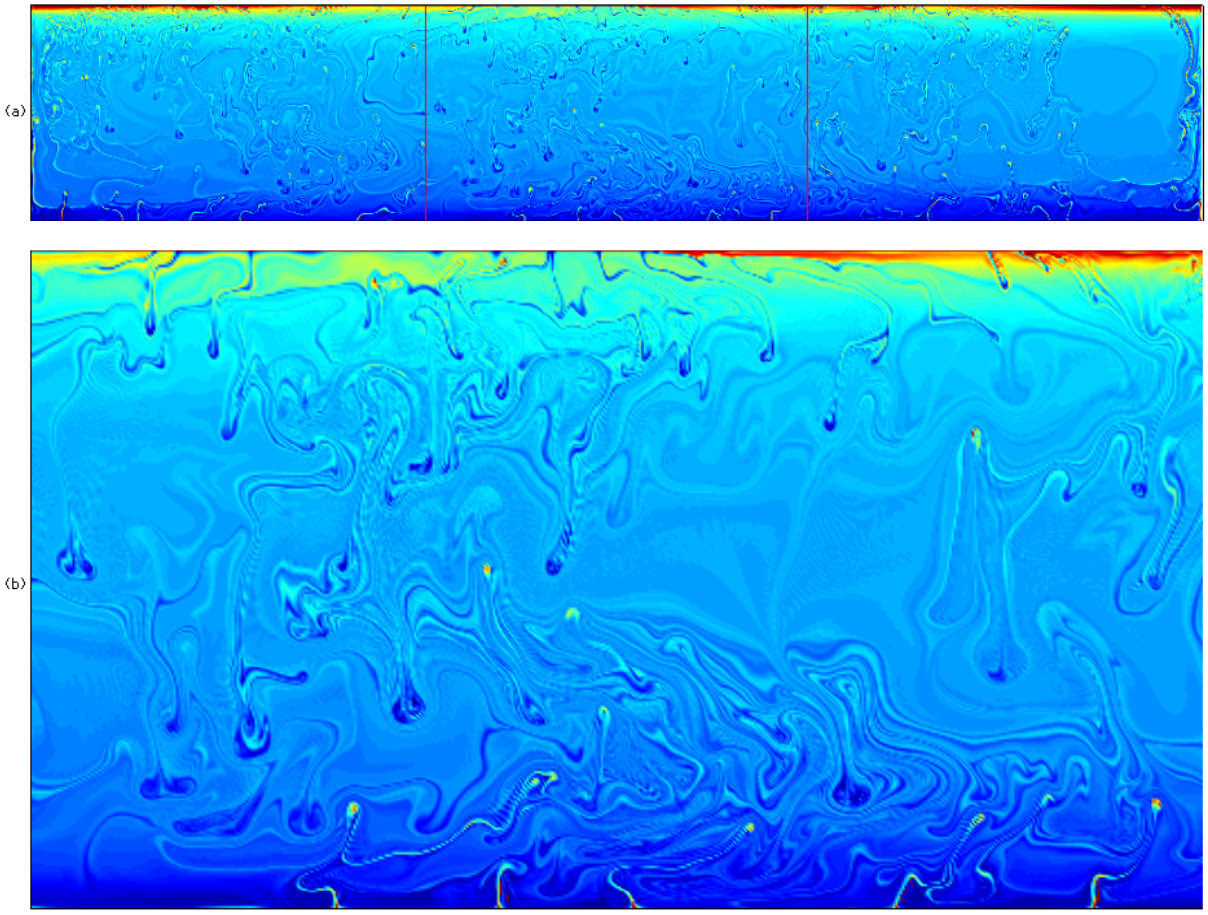

Figure 3.22. Absolute temperature field (with conductive term) for $Ra = 10^{11}$ in Cartesian projection. The temperature for dimensionless time $9 \cdot 10^{-6}$ (with corresponding timestep 22.500) is displayed in the panel (a) and a zoom of the area between red lines in the panel (b). Colorscale same as Figure 3.21.

3.5.5 Whitehead instabilities

A new and interesting feature which can develop in convective systems at higher Rayleigh numbers are the so-called Whitehead instabilities. This section originates in the paper by Murphy et al. (2000).

The idea of secondary instabilities developed from plumes has come from the recent high Rayleigh number simulation by Vincent and Yuen (2000). There is also evidence from seismic tomography (Bijwaard and Spakman, 1999; Goes et al., 1999) to suggest that mantle plumes can branch to some extent. Skilbeck and Whitehead (1978) and Whitehead (1982) performed laboratory experiments showing the formation of secondary instabilities from a tilted plume in a set-up in which the conduits were made by injecting oil into a more viscous heavier liquid.

We can show that Whitehead instabilities can be generated in high Rayleigh number convection within the framework of a homogeneous constant viscosity fluid (see Figure 3.23). In the case of $Ra = 3 \cdot 10^6$ (Figure 3.23a), the plumes are not yet fully developed, but we have found structures similar to Whitehead instabilities (see the red arrow in the figure). We do not consider them as true secondary instabilities, because the bent structure is an artifact of the collision of the plume with the top boundary. True Whitehead instabilities are shown in Figures 3.23b-d. The plumes are bent to such a point that new plumes (secondary or Whitehead instabilities) can rise from the old plume. We remark that while locating Whitehead instabilities it is necessary to view closely spaced timestep images or animations of plume formation and propagation to ensure that the wave-like patterns that we can see are generated due to secondary instabilities rather than plume-plume interactions which can appear deceptively similar.

The last figure (3.23e) shows convection for ultra-high Rayleigh number ($Ra = 10^{10}$). There is a transition in the style of convection somewhere between Rayleigh number of 10^9 and 10^{10}. Thus in ultra-high Rayleigh number convection there is the tendency for multicellular activities involving small-scale flows close to the top and bottom boundary layers. The plumes are shorter, the behavior is very turbulent, plume-plume collisions occur quite often, and it is no wonder that Whitehead instabilities appear no longer in such 'hard' convection.

We can infer that there exists a window in Rayleigh number space which favors the formation of Whitehead instabilities. We did not find any fully developed secondary instabilities in the case of $Ra = 3 \cdot 10^6$, and the turbulence of $Ra = 10^{10}$ does not allow the folding instabilities to progress. Thus the appearance of Whitehead instabilities can be considered as a feature pointing to convection between a certain window of Rayleigh numbers.

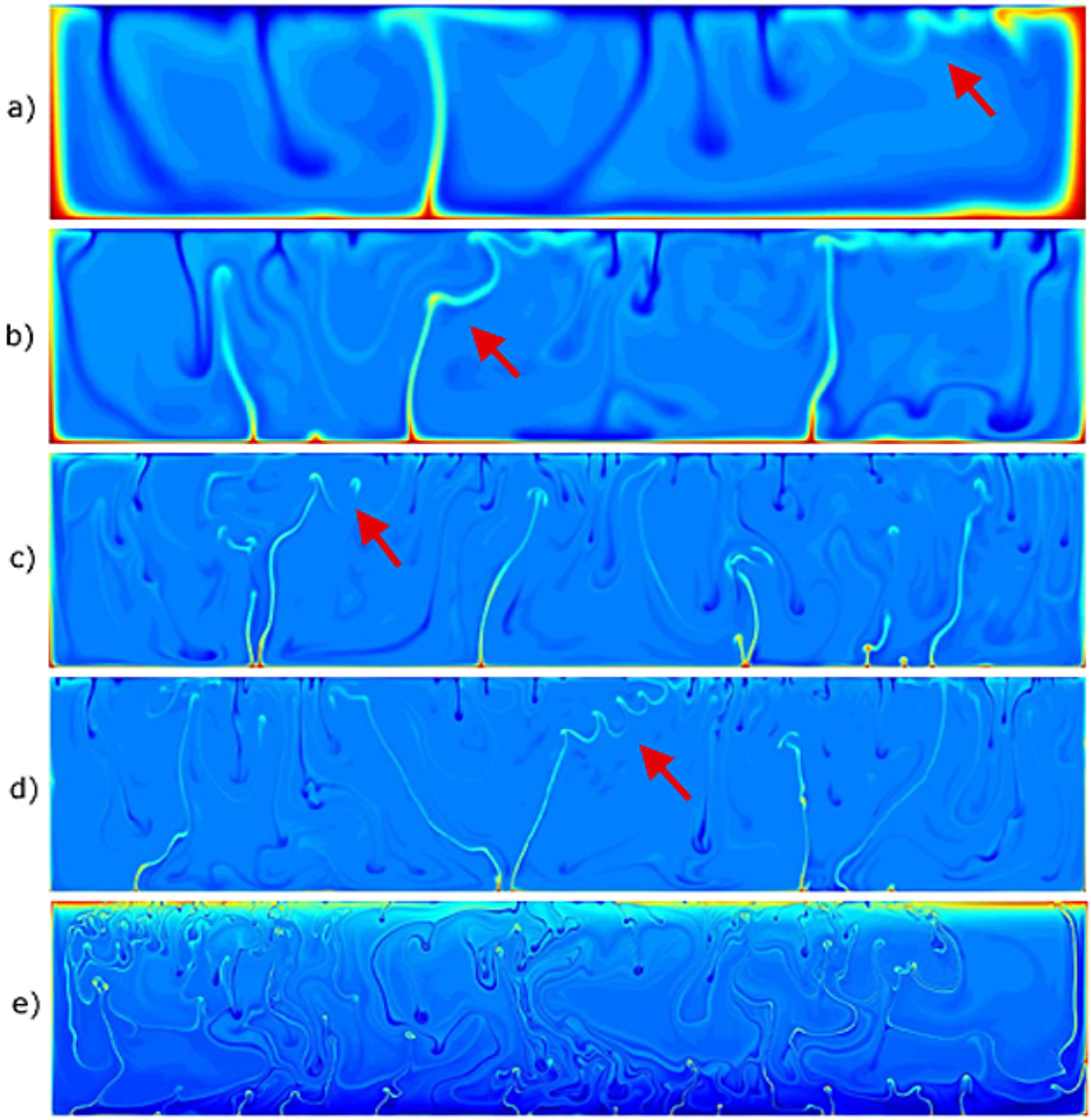

Figure 3.23. Examples of Whitehead instabilities developed in temperature fields. The used Rayleigh numbers: (a) $3 \cdot 10^6$, (b) $3 \cdot 10^7$, (c) $3 \cdot 10^8$, (d) 10^9 and (e) 10^{10}. The red arrows point to (a) the Whitehead-like instabilities and (b)-(d) the Whitehead instabilities. Panel (e) shows 'hard' convection with no Whitehead instabilities.

3.5.6 Vertical temperature profiles for high Rayleigh numbers

We have investigated vertical temperature profiles for Rayleigh numbers 10^6, 10^7, 10^8, 10^9 and 10^{10}. The last timestep for each run was chosen so as to be sure we were on the characteristic attractor of the run. Each vertical temperature profile was computed as an horizontal (tangential) average of the temperature field. Nondimensional temperature profiles are shown in Figure 3.24a. The temperature deviations, with excluded conductive term (3.48), are presented in Figure 3.24b.

First we will focus on features common for all considered Ra numbers. In the nondimensional temperature graph (Figure 3.24a), there is a sudden decrease from 1 to around 0.20 to 0.25 at the shell bottom. The temperature then remains nearly constant until it suddenly falls to 0 near the top. The profiles reflect boundary layered convection (e.g. Jarvis and Peltier, 1989), with the upper and lower boundary layers isolated by the isothermal middle core. The spherical geometry causes higher temperature peaks near the top boundary, the bottom peaks are almost negligible.

The thickness of the boundary layers, in general, decreases as the Rayleigh number grows, and the peaks move toward the boundaries (Jarvis and Peltier, 1989). These trends can be seen in Figure 3.24. There are also other features which can be seen in the figure. In the case of the $Ra = 10^6$ run, the influence of large-scale motion is still visible in the oscillations of the curve (Figure 3.24). The $Ra = 10^{10}$ run temperature profile differs from the others. The profile has a reversed temperature gradient in the central gradient (similar to that seen in cases of very low Ra profiles) and a large top boundary layer. This difference can be caused either by insufficient computational time which would be required for the absorption of the large scale mass in the top area or by a different convection regime from the ultra-high Ra convection (Section 3.5.4).

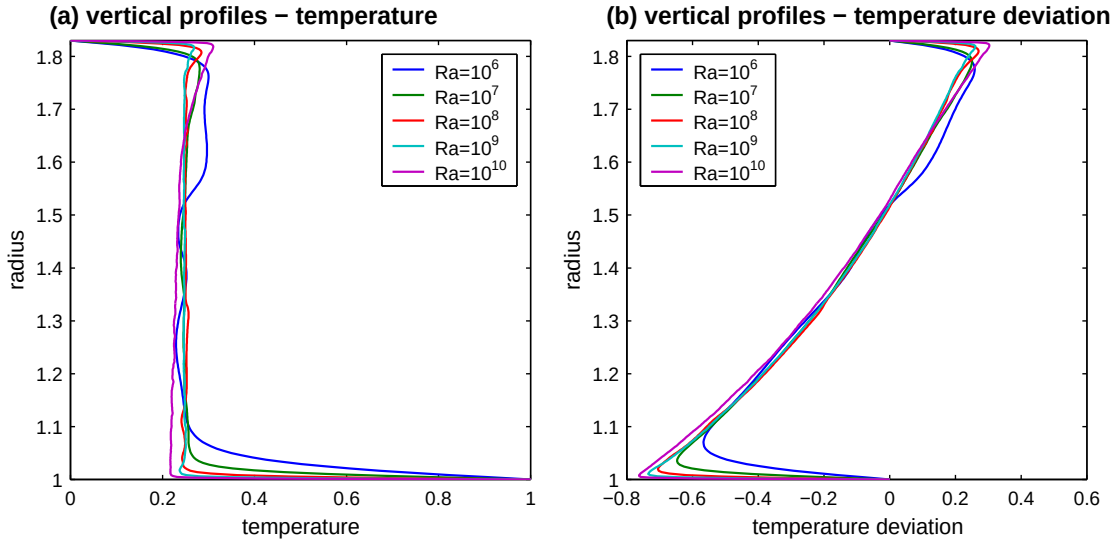

Figure 3.24. Vertical profiles of horizontally averaged dimensionless (a) temperature and (b) temperature deviation (without conductive term) for several values of Rayleigh number Ra.

3.5.7 Power laws for the kinetic energy and the Nusselt number

One of tools which can be used to predict the thermal history of the Earth without the necessity of solving the full set of hydrodynamic equations is the Nusselt number-Rayleigh number power law relation (Jarvis and Peltier, 1989). The power law is usually expressed in the form

$$Nu = \beta \left(\frac{Ra}{Ra_c} \right)^S \tag{3.64}$$

or

$$Nu = \gamma Ra^S , \tag{3.65}$$

where Ra is the Rayleigh number (3.24), Ra_c is the critical Rayleigh number for which convection occurs and the coefficient $\gamma = \beta / Ra_c^S$. The coefficient β and exponent S are, in general, functions of the aspect ratio of the convection cells, and they also depend on the boundary conditions (free, rigid) (Jarvis and Peltier, 1989). The effects of other physical parameters, spherical geometry, and partial internal heating were assumed to be insignificant. The studies by Christensen (1984, 1985) of high Rayleigh number regimes suggest that these assumptions are not valid for high Ra convection.
We have tabulated some of the previously published coefficients for the Nusselt number-Rayleigh number power law:

S	β (or γ)	**Description**
0.30	1.222	experiments with water (Pr=6.7) by Rossby (1969)
0.278	1.449	experiments with water (Pr=6.7) by Chu and Goldstein (1973)
0.281	1.490	experiments with silicon oils (Pr=200) by Rossby (1969)
0.282	1.55	high Prandtl number experiments by Sommerscales and Gazda (1969)
0.318	2.24	numerical convection model by Jarvis and Peltier (1982)
0.3185	0.2697 (γ)	numerical convection model by Christensen (1989)

Table 3.3. Published coefficients of the Nusselt number-Rayleigh number power law, definitions (3.64) and (3.65).

The Nusselt number-Rayleigh number relationship is not the only power law applicable to thermal convection. The boundary layer theory introduced by Turcotte and Oxburgh (1967) predicts that similar power laws also exist for the boundary layer thickness and the mean horizontal and vertical velocities, which was also demonstrated by Jarvis and Peltier (1989) from results of numerical modelling of thermal convection.

We investigated the dependencies of the kinetic energy W (definition (3.62)) and the Nusselt number Nu (definition (3.63)) on Rayleigh number Ra, see log-log graphs in Figure 3.25. The values are shown in Table 3.4, the mean kinetic energies and Nusselt numbers were computed from time-series from which we excluded the initial transitional parts. Corresponding standard deviations are included, the very small deviation in the case of $Ra = 10^{10}$ is probably caused by the insufficient time-series length for this high Rayleigh number. There are two dependencies in the cases of low Rayleigh numbers, the solid line belongs to runs started from the asymmetrical initial state and the dashed line to runs started from the symmetrical one.

Ra	**sym/asym**	$\bar{W}$	**std**	ϱ	$\bar{Nu}$	**std**	ϱ	**from time**
conductive state	-	0	-	-	1	-	-	-
$1.7 \cdot 10^4$	sym	$0.44 \cdot 10^5$	0	0%	4.0	0	0%	end
$1.7 \cdot 10^4$	asym	$0.47 \cdot 10^5$	0	0%	3.6	0	0%	end
10^5	sym	$3.8 \cdot 10^5$	$0.9 \cdot 10^5$	24%	6.3	0.4	6%	0.5
10^5	asym	$3.5 \cdot 10^5$	$0.5 \cdot 10^5$	14%	5.1	0.3	6%	0.5
$5 \cdot 10^5$	asym	$1.7 \cdot 10^6$	$0.5 \cdot 10^6$	29%	9.5	0.9	9%	0.3
10^6	asym	$4.2 \cdot 10^6$	$1.3 \cdot 10^6$	31%	11.6	1.1	9%	0.22
10^7	asym	$1.8 \cdot 10^7$	$0.6 \cdot 10^6$	33%	23.9	1.6	7%	0.0017
10^8	asym	$4.1 \cdot 10^8$	$1.2 \cdot 10^8$	29%	54.5	3.2	6%	0.0010
10^{10}	asym	$1.9 \cdot 10^9$	$0.05 \cdot 10^9$	3%	213.0	1.8	1%	5.55e-6

Table 3.4. Mean values of the kinetic energy W and the Nusselt number Nu for different Rayleigh numbers Ra and symmetrical/asymmetrical initial temperatures. Std refers to the standard and ϱ to the relative deviations of the quantities. The last column gives the time from which the means were computed to be sure that the convection left its transition part. In the conductive state row, there are theoretical values for the conductive temperature profile (3.48). Other rows contain values of computed Ra runs. The $Ra = 10^{10}$ value might still be influenced by short computational time.

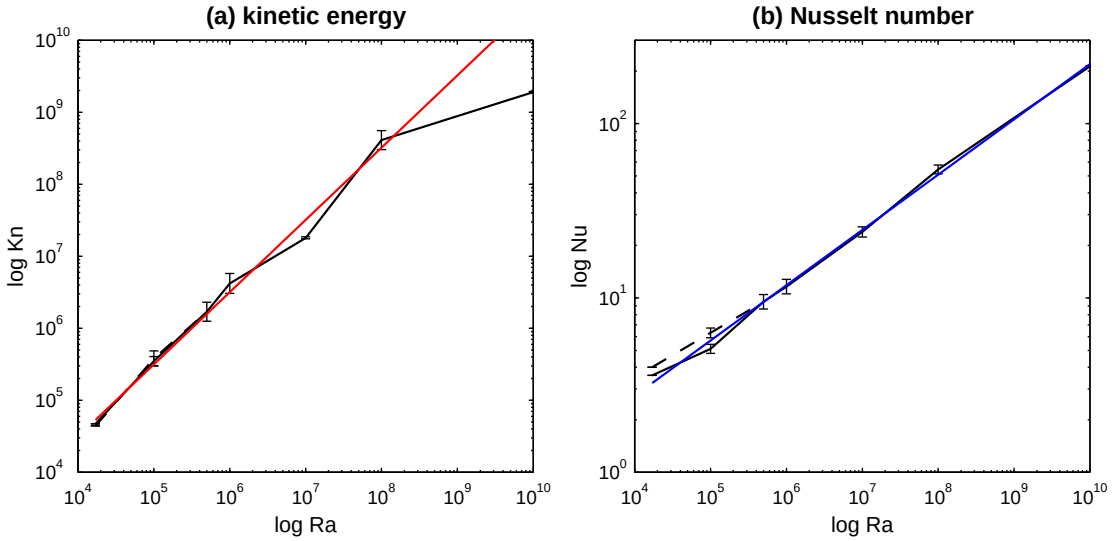

Figure 3.25. Log-log graphs of relationships between (a) the kinetic energy W and (b) the Nusselt number Nu (also surface heat flow) on the Rayleigh number Ra. Values and deviations see in Table 3.4. Solid black lines connect values for asymmetrical initial state, dashed lines for symmetrical one. The linear approximation is marked by color lines, the red line has a slope equal to 1.003, shift to 0.482 and the approximation was computed on the Ra interval $1.7 \cdot 10^4 - 10^9$. The blue approximation has a slope equal to 0.317, shift to -0.830 and it was computed on the Ra interval $5 \cdot 10^5 - 10^{10}$.

Although the coverage of points in the graphs in Figure 3.25 is not very dense, we can see a linear trend in the relationships. A linear approximation of the kinetic energy plot gives a slope

of 1.003 and a shift of 0.482, which corresponds to $S = 1.003$ and $\gamma = 3.030$ in relation (3.65). A similar approach for the Nusselt number plot gives a slope of 0.317 and a shift of -0.830, which corresponds to $S = 0.317$ and $\gamma = 0.148$. Comparing the Nu coefficient with the last row in Table 3.3, we can see very good agreement in the exponent S and agreement on the order of the coefficient γ). Different values of γ may be caused by different geometries or aspect ratios, but we must be careful in presenting such conclusions because of the insufficient length of the time-series for different Rayleigh numbers.

Also, very small values of the averaged kinetic energy for $Ra = 10^{10}$ (see Figure 3.25a) could be caused by the small number of computed timesteps; although the related Nusselt number fits the blue line (Figure 3.25b) very well. The other possibility is the qualitative change of the convection regime in the case of $Ra = 10^{10}$ run (see Section 3.5.4).

3.6 Discussion & concluding remarks

In the first sections of this chapter we introduced thermal convection as a nonlinear system. Therefore, a question arises as to different kinds of attractors to which the system may get when the controlling parameter changes. One of the attractors can be the so-called strange attractor, at which the attempt to find a current position of the system on the attractor is impossible; only certain characteristics of the whole attractor are able to be found. This chapter is aimed at characterizing strange attractors.

The former works (Lorenz, 1963; Chang and Shirer, 1984), in which only simplified models of thermal convection with only a few coefficients were used, indicated the following sequence of regimes with increasing control parameter (the Rayleigh number): conduction, steady state, a periodic solution and a chaotic attractor (see Figure 3.2 on the page 33). Our model has many more dimensions, but we can expect a similar development of the system regimes.

We have started the investigation with a low Rayleigh number $Ra = 1.7 \cdot 10^4$. Since this Ra is higher than the critical one, the system has already left the conductive state and finished in the steady state. We chose two starting states, one tangential symmetrical (Figure 3.3a, page 36) and the second slightly tangential asymmetrical (Figure 3.3b). After leaving the transitional state the systems settled in two different steady attractors. Both attractors are symmetrical, which corresponds to the attempt of the system to find the simplest regime corresponding to the low Rayleigh number. The system, which started from the symmetrical initial temperature is four-celled (Figure 3.4a, page 36); while the second system is only two-celled (Figure 3.4b). To verify our idea that four-cell convection is not very stable for low Rayleigh number due to its small attracting basin, we prepared a control run with the same symmetrical initial temperature but with a small (1/100 of the original amplitude) asymmetrical perturbation. This run ended in a two-cell attractor as with the asymmetrical case. In comparison with the first two runs, the time evolution of the control run was more complicated. Examining the kinetic energy and the surface heat flow (Nusselt number) time-series (Figures 3.5, 3.6 on the page 38), we found two sudden jumps by which the system switched its regime from the four-cell to the two-cell one. The first, 'unsuccessful', jump is visible only in the kinetic energy time-series (which is a global proxy), the semi-global Nusselt number proxy was influenced minimally. There is another interesting feature in the examined control run, which is important for other low Rayleigh number convections; the

very long time needed for stabilization of the system as compared to the time needed for reaching the attractors in the original runs. We can suppose for the following low Ra runs that the physical space structure of the systems will be simple, but the time evolution will be complicated and for a perfect description of the system's attractor we will need a very long time evolution investigation.

We have also chosen a similar strategy of two different starting stages for the next Rayleigh number, $Ra = 10^5$. The run that was started from the symmetrical initial stage finished in the periodic symmetrical attractor (Figure 3.4c, page 36). The number of convection cells decreased to two, and the temperature distribution was the inverse of the $Ra = 1.7 \cdot 10^4$ run. The major upwelling in the middle of the shell periodically changes its intensity, which can also be seen in the both kinetic energy and the Nusselt number time-series (Figure 3.7, page 40). The system, which started from the asymmetrical state, remained in a two-cell regime similar to the previous low Rayleigh number system; however, the Rayleigh number was high enough to prevent the system from reaching a simple symmetrical regime. The major downwelling moved to the right-hand side, and gave rise to the small convection cell in the right-hand side and the cell with an aspect ratio high enough to allow the formation of the secondary plumes on the left-hand side. Although the system still looks simple, the temporal evolution of the kinetic energy and the Nusselt number proxies embody unexpected complexity. The Fourier spectrum of the time-series (Figure 3.9-3.10, pages 41-42) contradicted the expectation that the regime is quasi-periodic. The wavelet spectrum reveals two significant period bands (one around $5 \cdot 10^{-3}$ and the second around $2 - 3 \cdot 10^{-2}$ dimensionless time), with time-windows of both high and low activity. A certain similarity of the long-period band in the wavelet spectrum of the kinetic energy with the band in the Nusselt number spectrum, together with the absence of the short-period band in this semi-global proxy, give us the opinion that the long-period band originates due to the behavior of the two convection cells; while short-period events belong to the development of secondary plumes in the large cell. We did not conduct analysis of the wavelet spectra arising from a correlation of the short- and long-period bands, which could reveal an interference between the convection cells and the plumes rising inside the cells; instead we focused on the estimation of the attractor dimension for the system.

Computation of the correlation dimension from the kinetic energy and the Nusselt number time-series was prevented by an unsatisfactory time-series length. The first estimation of the dimension was performed for time-series of dimensionless time 3.9; neither the correlation integral computed from the kinetic energy time-series, nor the integral from the Nusselt number time-series saturated as the embodied dimension increased. We increased time-series by two times, after which the dimension of the kinetic time-series settled on approximately 13-15; while the Nusselt number still had an improper value for the successful dimension estimation (see Figure 3.12 on the page 45). High temporal chaoticity for such a low Rayleigh number as $Ra = 10^5$ is rather surprising.

From the $Ra = 10^5$ convection, where we found one periodic and one chaotic attractor depending on the initial state, we conducted similar computations of long time-series followed by the dimension estimation for higher Rayleigh numbers. Moreover, we reduced starting conditions to only the asymmetrical one, the computation became more and more time demanding and the symmetry was quickly lost due to numerical errors.

The $Ra = 5 \cdot 10^5$ and $Ra = 10^6$ runs have a regime qualitatively similar to the $Ra = 10^5$ (asym.) run. Two cells still dominate the convection system, but the convection itself becomes more turbulent, and secondary plumes arise in both the cells. We can also see increasing deviations from the average values of the kinetic energy and the Nusselt number (Table 3.4, page 61) with

increasing Ra. Maximum deviations occur for the $Ra = 10^6$ and $Ra = 10^7$ convection systems. The wavelet spectra of the $Ra = 5 \cdot 10^5$ and $Ra = 10^6$ time-series still preserve the separation of the wavelet power to the two main frequency bands, also the mean values and the gap between the bands remain at the same values (see Figures 3.15-3.16 on the pages 48-49). The higher vigour of the secondary plumes, which influences motion in the two main convection cells, is reflected in the appearance of larger and larger significant periods in the wavelet spectra. All these features indicate the end of the two-cell convective regime and the increasing domination of the plume-convective regime with higher Rayleigh numbers. The change in regimes, where the effects of these two kinds of convection are balanced, was found at $Ra = 10^6 - 10^7$ when the deviations from the average values of the kinetic energy and the Nusselt number are the highest. We point out that these Rayleigh numbers correspond to the estimated Rayleigh number for the whole-mantle convection in the real Earth (Jarvis and Peltier, 1989).

Since the plume-convective regime prevails in the high Rayleigh number convection (10^6-10^9), we focused on examination of the plume evolution characteristics. A first look at the temperature fields reveals a low number of whole mantle plumes; although the plumes are thinner and thinner with increasing Rayleigh number, the average number of the upwellings remains small (about 3-5 plumes, see Figures 3.17a-c, page 50). In the case of the $Ra = 10^6$ convection (Figure 3.18, page 51), the cell-convection mode is still strong. The plumes are large and bent, with almost no plume-heads, but with plume-tails that remain in the top and the bottom boundary layers. On the contrary, the regime $Ra = 10^8$, with stronger plume-convection, has the plumes flatter with fully developed plume-heads. The convection at $Ra = 10^7$ seems to be critical to the transition. The cell-convection is of the same power as the plume-convection; the plumes have an optimal width to participate in the hardest collisions between themselves (Figure 3.19, page 52).

The evolution of the plumes together with the plume collision is the first effect which anybody studying high Rayleigh number convection will notice. We found features, such as the collision of up- and downwellings, side collisions of two upwellings followed by absorption of one plume by another, or the striking of an upwelling root by a downwelling head. An interesting phenomena, which occurs only in a certain interval of Rayleigh numbers, is the apparition of Whitehead instabilities (see Figure 3.23, page 58). This multiple bending of one plume, followed by the rising of new 'baby' plumes from the critically curved 'mother' plume, occurs under the same conditions as whole mantle plumes which can collide. We found an interval (Murphy et al., 2000) of Rayleigh numbers at 10^7-10^9, for which Whitehead instabilities occur. In the case of the $Ra = 10^6$ convection, the plumes are too wide to be capable of multiple bending. In the case of the $Ra = 10^{10}$ convection, there are no whole-mantle plumes. Thus the discovering of the Whitehead instabilities in the convection can help to narrow the possible interval of Rayleigh numbers.

Significant change of the behavior of the convection system arose at $Ra = 10^{10}$. The turbulence is now so high that it prevents plumes from growing through the whole mantle; layered convection occurs (Figure 3.21, page 55). A lot of small up- and downwellings can rise only to a certain height (due to the spherical geometry of our model the downwellings are much smaller than the upwellings), the middle layers are filled with the remains of plumes, especially plume-heads, which look like little drops. The strong mixing had to be compensated by computations with large dimensional fields and the used timestep was very small. Therefore the modelling of ultra-high Rayleigh number convections was very time-consuming. We successfully bypassed the transition stage in the case of the $Ra = 10^{10}$ convection, but the question still remains, whether we fully reached the attractor

of the system. The $Ra = 10^{11}$ computation did not still leave its transition stage (see Figure 3.22, page 56).

In the previous paragraphs we described the convection regimes that we saw during our investigation of the different Rayleigh number runs. The last section of this chapter will be applied to features that should be independent on the convection regime, and to the proxies at power law relations.

Horizontally averaged vertical temperature profiles for high Rayleigh numbers embody a flat middle part with temperature peaks in the boundary layers (Jarvis and Peltier, 1989). Because we used the spherical shell geometry, and not the Cartesian one, there are small differences in our vertical profiles (Figure 3.24) from the published ones (Jarvis and Peltier, 1989). The constant temperature in the middle part of radial profile is shifted from 0.5 to ~ 0.25. The other effect of the geometry is the reduction of the low boundary temperature peaks, while the upper ones are more expressive. What remained similar to the simulations in the Cartesian box is the shrinking of temperature peaks along with their shifting to the boundary with increasing Ra. The last temperature profile computed for $Ra = 10^{10}$ is slightly different from the others. Whether the negative gradient in the middle part together with the high and large temperature peak at the top of the shell is caused by a quantitatively different convection regime, or only by the short computation of this run, is an open question at this moment.

Dissimilarity of the $Ra = 10^{10}$ run from the others is also evident in the power laws of the global proxies. The Nusselt number-Rayleigh number power law relation is well known both from physical experiments with water (Rossby, 1969; Chu and Goldstein, 1973) and silicon oils (Rossby, 1969) and from numerical simulations (Jarvis and Peltier, 1982; Christensen, 1989). Our slope of $S = 0.317$ (see Figure 3.25b) is in a good agreement with the values of 0.318 published by Jarvis and Peltier (1982) and 0.3185 published by Christensen (1989). The coefficient γ related to the shift of the power law in the log-log graphs was estimated at 0.148, which is approximately two times less than the value of 0.2697 found by Christensen (1989) in a Cartesian box. Here the difference is probably caused by the different geometries in which the convection was computed. A power law relation similar to that for the Nusselt number was also determined for the kinetic energy (Figure 3.25a). Although the problematic $Ra = 10^{10}$ run satisfies the Nusselt number-Rayleigh number power law relation very well, the averaged value of the kinetic energy is much smaller than the corresponding linear approximation. Thus the fitting value of the Nusselt number corresponds to the proper shift of the upper boundary temperature peak, but questions related to the small value of the kinetic energy and the negative temperature gradient in the interior will last until longer computation times are achieved for $Ra = 10^{10}$ run.

One of the helpful tools in the investigation of the different kinds of convection regimes can be the 2-D wavelet analysis of the temperature and vorticity fields. We included the convection scalograms in Chapter 4.

Chapter 4

Results of Wavelet Analysis

Wavelet functions, with a Gaussian or a peak-like Fourier spectrum, are able to localize a structure of a given frequency in an analyzed time-series (or field). In such case the wavelet transform behaves as a powerful band-pass filter. In this chapter, we will focus on the examining abilities and efficiency of the wavelet filter in 2-D space. We chose three different areas of interest: the geoid, mixed mediums and thermal convection. Each of the fields has its own characteristics. The geoid embodies distinct large-scale structures but small features are invisible 'to the naked eye'. On the contrary, the mixed field hides its large-scale texture; moreover, the field also contains discontinuities, and this fact causes high sensitivity of the wavelet transform to the field shape. The last analyzed domain, thermal convection, behaves differently as the controlling parameter is changed. We will try to demonstrate the efficiency of the wavelet transform in the exploration of all scales.

The isotropic 2-D wavelet transform (2.6) is used in the next three sections. We chose the 2-D Mexican-hat wavelet (2.14) as the convolution kernel. The scalograms directly show the wavelet

Scale mode	r	λ	Scale mode	r	λ
3	0.47	0.42	18	0.02	0.02
5	0.30	0.27	20	0.01	0.01
6	0.24	0.22	23	0.006	0.005
7	0.19	0.18	25	0.004	0.003
11	0.08	0.07	30	0.001	0.001
15	0.03	0.03	40	0.0001	0.0001

Table 4.1. Resolution of the 2-D wavelet transform for the Mexican-hat wavelet. r is the relative diameter (with respect to the length of the box) of an area where the main peak of the wavelet function is positive, and λ is the Fourier wavelength corresponding to the wavelet scale a, see (2.15). Half of λ gives the resolution of the wavelet transform relative to the length of the box.

spectrum corresponding to the signed L_1-norm (2.18) for both the geoid and the thermal convection analysis, or the unsigned L_1-norm in the case of the mixed field. The problem with visualization of the 3-D scalograms was solved by portraying panels for several wavelet scales or modes. The number of the mode is always referenced in the text; it corresponds to the resolution of the wavelet function as shown in Table 4.1.

4.1 Geoid

4.1.1 Introduction

The Earth's geoid is the equipotential surface of the gravity field. Over the ocean it corresponds to sea level after subtracting the oceanic dynamic topography. Geoid anomalies are undulations of this equipotential surface with respect to a reference ellipsoid. Earth's rotation is one mechanism that produces anomalies (Sabadini et al, 1990). A non-hydrostatic geoid is corrected for the Earth's rotation. Non-hydrostatic geoid anomalies are due to mass anomalies within the Earth, and their source depends on their wavelength. Long wavelength geoid anomalies have sources mainly in the lower mantle (Chase, 1979); whereas short wavelength anomalies have a lithospheric source (Hager, 1983; Le Stunff and Ricard, 1995). Past studies of geoid anomalies have made use of spherical harmonic decomposition to separate features of different wavelengths. Short wavelength features have been used to study local lithospheric structures (Calmant and Cazenave, 1987). Long wavelength features bring information on deep mantle processes (Cazenave et al., 1989). Recent studies have used geoid anomalies to constrain the viscosity structure of the mantle (Hager, 1984; Ricard et al., 1984; Forte and Mitrovica, 1996; King, 1995; Čadek et al., 1995; Kido and Čadek, 1997; Čadek and Fleitout, 1999).

We used a Mercator projected non-hydrostatic geoid with 4 degree latitude and longitude resolution, which was obtained by converting and truncating the full geoid with 1 degree resolution (Rapp and Paulis, 1990). This section will discuss the wavelet filter used in the study followed by a display of the wavelet-filtered geoid at various scales. Next we will introduce the use of the E_{max} and k_{max} proxies in relation to the geoid. A discussion about the advantages of wavelet analysis over the more well known spherical harmonic analysis will follow, and, finally, we will display the use of small scales to study regional features of the geoid.

4.1.2 The wavelet featured geoid

The potential anomalies corresponding to the non-hydrostatic geoid used in our study were of spherical harmonic degree 90, which corresponds to about 400 km in spatial resolution. The geoid is displayed in Figure 4.1a in the Mercator projection. The horizontal and vertical axes represent longitudes (0 to 360 degrees) and latitudes (-90 to 90 degrees), respectively. A coastline map is also shown in each figure. Only large-scale features, such as a strong maximum over Indonesia or local minimum over India, are clearly observed (Figure 4.1a). From now on, the color map ranges from blue (minimum) to green, yellow, and red (maximum). As we are only interested in qualitative features here, all the data displayed in the following figures were normalized to 1.

The wavelet filtered gravity potential (Figure 4.1b) at a wavelet resolution of 9000 km shows only

the largest structures of Figure 4.1a. More details are displayed at a resolution of 3000 km (Figure 4.1c). Strong depressions in the geoid appear over the southern tip of India and the west Atlantic, and strong maxima appear over the western and central Pacific and the Andes. The presence of a maximum over Iceland is not interpretable because of the strong deformation of the Mercator projection at latitudes over 45 degrees. Visible features are well known from previous studies (e.g. Crough and Jurdy, 1980). The wavelet analysis allows us to selectively dial into different scales to see at which scales various features appear. This is an important advantage over both conventional truncated window analysis and spherical harmonic expansion.

At scales of about 400 km, the visible anomalies only sample the Earth down to about 100 km depth. Therefore, anomalies seen at this scale are caused by lithospheric structures. The wavelets allow us to outline topographic features from our dataset of spherical harmonic degree 90 and compare them with the Earth's relief (see Figures 4.3 and 4.4). The subduction zones along the west coast of South America (number (1) in Figure 4.4), the Aleutian Arc (2), and the East Pacific trenches down to the latitude of Tonga are clearly visible, (3)-(9). Mountain belts formed by convergent plate processes such as the Himalayas (12) and the Andes (11) are apparent. The African rift system, the Mid-Atlantic ridge (16), Hawaii (18), the Atlas Mountains (15) of northwest Africa, and some details of the plates of the Indian Ocean at the latitude of Madagascar (17) are also visible. The appearance of the Australian coastline visible in the scalogram is due to the absence of a continental margin and can easily be picked out on very high resolution spherical harmonic gravity maps (Sandwell and Smith, 1997). Areas with more complicated tectonic structures such as Europe can be studied by zooming into the region (see below).

4.1.3 The $E_{\max}$-$k_{\max}$ maps

The complete information of the local wavelet spectra analysis is difficult to visualize because at each location an entire spectrum must be rendered (Chapter 2). This requires operation over a grid size of $N \times N \times M$ where N is the number of grid points and M is the number of scales computed. This demands such a large memory capability that it is prohibitively large for a high resolution dataset such as the gravity dataset of Sandwell and Smith (1997).

We used the low-dimensional parameterization of the two proxy quantities discussed in Chapter 2: E_{max}, the local gravitational energy, and k_{max}, the associated local wavenumber, to synthesize the data. Since the sign of the geoid anomaly is lost when taking the L_2-norm to calculate E_{max}, we represent the local sign energy by using $\tilde{E}_{max}$ defined in (2.20). The k_{max} map represents the distribution of scales for which the absolute value of the gravity potential is maximal locally. For a given range, if k_{max} were the smallest wavenumber, we would have a flat plateau on the k_{max} map. The k_{max} increases sharply along boundaries where there are sharp gradients in E_{max}. Therefore, the k_{max} helps to facilitate the detection of boundaries of structures.

The spatial distributions of E_{max} and k_{max} are plotted in Figures 4.2a and 4.2b. E_{max} has been normalized at each scale by the areal average of E_{max} for that scale. We calculated E_{max} for scales ranging from 1000 km to 400 km. In the E_{max} map we can immediately discern strong positive signals in the Andes (for their localization see the number (11) in Figure 4.4), the Tibetan Plateau (12), and the Alpine-Tethys range (13) and a negative signal in southern India. We can also discern Hawaii (18) and the Azores. All the plates and ridges shown in Figure 4.2b are also present in the k_{max} map. Fracture zones in the three major oceans can also be determined from

the k_{max} map as well as the boundaries of the Pacific, the Nazca, and the North America Plates (compare Figure 4.2a with Figure 4.4). Many convergent zones such as those of South America, Indonesia, Japan, and Tonga are delineated. In fact, E_{max} gradients are related to small values of k_{max}. Boundaries of the zones associated with high E_{max} values, such as long ridges, are correlated with strong gradients in gravity potential. This implies very small spatial scales due to the sharp front of the adjacent high and low gravity potential values along ridges. The scale of these gradients could be a criterion for limiting the horizontal extent of the gravity influence of the oceanic ridges.

4.1.4 Advantages of wavelets over spherical harmonics

The results presented in this chapter are obtained by means of the wavelet analysis. We very often have datasets in a spherical-harmonic decomposition; the cutting of the spherical harmonics on a certain level offers an easy but dangerous way to depict features of only certain scales in our dataset. To show the hazard allied with such a method we compared the short-wavelength geoid cut at degree 20 or 40 with the wavelet spectrum of mode 20 (Figure 4.5). We see the same structure in all places where the signal is strong, but to the global character of the spherical bases, the cutting method fails in places of a weak signal. The strong signal in one place excites a formation of a false signal in the spherical-harmonic decomposition in other places, and must be fixed by the harmonics of higher orders. Thus after the truncation we obtain the false spotted signal in places of low magnitudes, which can be confusing.

A more precise comparison of the geoid that is cut at degree 20 or 40 with the wavelet spectrum of mode 20 reveals more of the ability of the wavelet filter. As we have already noted, the Fourier spectrum of the Mexican-hat wavelet is the Gaussian function, and on the scalogram shows features not only at scale mode 20, but also those which are slightly bigger or smaller. Therefore, we can localize not only the small-scale subduction zones but also the medium-scale Mid-Atlantic Ridge. In the truncated spherical harmonic geoid, some areas are of same clarity as in the wavelet spectrum (subduction zones, the Himalaya, and the Atlas Mountains), some can be found in the truncated spherical harmonic geoid only when we know where to look for them (the Mid-Atlantic Ridge and Australian coastline), and some of them can only be found in the wavelet figure (structure around Hawaii). Thus we again emphasize the wavelet transform as a powerful local analysis which, reflects all the features.

4.1.5 Regional studies

Due to their compact support, wavelets allow us to zoom into any region and renormalize the fields using regional maxima. This allows us to investigate regional geologic problems such as the location of terrane boundaries. We have selected four regions to zoom into: the area of Japan and the Philippine Plate, South America, Europe, and the United States. Each region is shown at a scale associated with 400 km resolution, together with the E_{max} and k_{max} distributions.

The Japan and Philippine Plate area is shown in Figure 4.6. The E_{max} map (Figure 4.6c) shows two strong maxima over Japan (see number (1) in Figure 4.7) and the Philippines (2). These are areas associated with very strong compressional features. The Japan maximum occurs over an area of a major triple junction of the Eurasian (3), Philippine (4) and Pacific (5) Plates. Another strong maximum appears over the Philippines (2) which are being compressed by trenches on both

sides. Small-scale minima occur in the vicinity of the Japan (6) and Mariana (7) Trenches, an even weaker minimum can be found over the deepest known place on Earth, the Challenger Deep (8). A large-scale minimum on the E_{max} map covers the Banda Sea (9), which looks like a forgotten promontory of the Eurasian Plate between New Guinea and the Philippines. The outline of the Pacific and Philippine Plate trench systems is clearly visible in the smaller scales (Figure 4.6a). The trench systems can be also seen in the k_{max} map along with the back-arc spreading in the Philippine plate.

The South American region is shown in Figure 4.8. A very strong maximum appears over the Altiplano Plateau (number (1) in Figure 4.9)) in E_{max} map. The Altiplano Plateau is associated with an E_{max} value of 3.7, the largest of any of the mountain ranges we examined (Table 4.2). This indicates the presence of a large quantity of light mass, most likely in the form of a very deep root. The Peru-Chile Trench (2) system and the Andes Arc (1) are visible on the smaller scale and k_{max} maps (Figure 4.8a-b).

The European area is shown in Figure 4.10. In the medium scale and E_{max} maps a strong maximum over the middle part of the Alpine-Tethys Range (with the Turkey mountains in the west, the Caucasus in the north and the Zagros Mountains in the east, see numbers (1)-(3) in Figure 4.11) and a maximum of the similar magnitude over the Atlas Mountains (4) of northwest Africa are visible. Note the absence of a strong maximum over the Alps (5)-(6). A minimum is apparent in the vicinity of the Hellenic Trench (7), especially its eastern part. In the small scale (Figure 4.10b) we see a very strong maximum over the Aegean Sea (8). This is an area of the high heat flow associated with back-arc spreading (Fytikas and Kolios, 1979). The Hellenic Trench appears as a strong minimum. The Atlas Mountains also appear as a strong maximum along with a weaker maximum associated with the Sierra Morgan (9) on the Spanish side of the collision zone. A very weak maximum (see Table 4.2) is visible over the Swiss Alps (5) and a barely detectable high is seen over the Austrian Alps (6). The disconnected nature of the roots of the Eastern and Western Alps is confirmed by seismic studies (Babuška et al., 1990). Yegorova et al. (1998) proposed that the gravity high that would normally be associated with the thickened root of an orogeny is weakened by high density bodies in the lower crust and upper mantle. The presence of a high density body below the orogeny is known from seismic studies (Kissling, 1993).

The United States and surrounding regions are shown in Figure 4.12. On the large scale and E_{max} maps we can see maxima in the western United States and the Sierra Madre Oriental of Mexico (see number (2) in Figure 4.13). Although the Sierra Madre Oriental (2) mountains are not as wide and high as the Sierra Madre Occidental (1) mountains, the maximum over the Sierra Madre Oriental is higher, and it is probably influenced by a volcanic region in the south of the mountains (outside map), where the volcanoes Popocatépetl, Pico de Orizaba and Iztaccihuatl are situated. Minima can be seen over the West Atlantic abyssal plains surrounding the Bermuda Rise (3) which appears as having an average gravity signature for the region. A minimum is also visible over the Gulf of Mexico (4) in the Mexico Basin. In the smaller scale map (Figure 4.12b) we can see detailed structure of the western United States. For wavelet coefficients and E_{max} values of important features see Table 4.2. We detect two strong maxima, one associated with the Colorado Rockies (5) and one over the Yellowstone hotspot (6). Other weak maxima can be found in the small-scale map (Figure 4.12b), e.g., along the Sierra Nevada (7) and the Cascades (8). The Mexico Basin in the Gulf of Mexico (4) appears as a strong minimum. Detailed structures of the Western Atlantic begin to appear at this scale (compare to Figure 4.13). The abyssal plains appear as

minima. The Blake Plateau (see the Bahamas (9)) off the east coast of Florida is visible along with the location of fracture zones cutting the weak maximum of the Bermuda Rise (3). The relatively flat area in the middle of the continent exhibits two interesting minima, related to the one billion year old Midcontinent rift, which starts in Lake Superior (10), continues in the SW direction (11). The rift is now buried by nearly one-half mile of younger sedimentary rocks (Cannon, 1992). On the k_{max} map, one of the most astounding features is the delineation of Precambrian rift zones including the Midcontinent Rift (10)-(11) and the Mississippi Valley Rift. The boundary between the continental shelf and the abyssal plain is delineated off the eastern coast. The Bermuda Rise (3) appears as a green point. In the western United States and northern Mexico the boundary of the Sierra Madre Occidental (1), Sierra Nevada (7) and Cascade Range (8) along the Great Valley (12) are delineated. The k_{max} distributions in Canada are not interpretable because of the distortion due to the Mercator projection above 45 degrees latitude.

Location	**Number & figure**	**Medium scale**	**Small scale**	**E-max**
Atlas Mts.	(4) in Figure 4.11, (15) in Figure 4.4	0.24	0.054	0.38
Swiss Alps	(5) in Figure 4.11	0.07	0.022	0.05
Aegean Sea	(8) in Figure 4.11		0.078	
Hellenic Trench	(7) in Figure 4.11	-0.31	-0.076	-0.81
south of the Caucasus	(2) in Figure 4.11	0.31	0.031	0.80
Zagros Mts.	(3) in Figure 4.11, (13) in Figure 4.4	0.21	0.035	0.08
Himalayas	(12) in Figure 4.4	0.40	0.063	1.22
Philippines	(2) in Figure 4.7	0.32	0.061	0.60
Japan	(1) in Figure 4.7	0.27	0.071	0.34
Challenger Deep	(8) in Figure 4.7		-0.041	
Sierra Madre Oriental	(2) in Figure 4.13	0.25	0.037	0.43
Colorado Rockies	(5) in Figure 4.13		0.025	
Yellowstone hotspot	(6) in Figure 4.13, (20) in Figure 4.4	0.23	0.020	0.35
Midcontinent Rift	(11) in Figure 4.13		-0.015	
Gulf of Mexico	(4) in Figure 4.13	-0.18	-0.034	-0.43
Abyssal Plains around the Bermudas	(3) in Figure 4.13	-0.22	-0.023	-0.40
Altiplano plateau	(1) in Figure 4.9 (11) in Figure 4.4	0.54	0.100	3.70

Table 4.2. Values of the wavelet spectra and E_{max} in several locations. Medium scale means mode 15, small scale mode 20. Resolution of the modes seen in Table 4.1.

4.1.6 Discussion and concluding remarks

In this first section we analyzed of the geoid with emphasis on the small-scale structure. We did not worry about the influence of the boundaries in computation of the wavelet spectrum; moreover, we could use the Mercator projection of the spherical field, since we concentrated on the low latitude belt. The problem of geometrical distortion introduced with the Mercator projection and the Fourier transform above latitudes of 45 degrees can be solved by rotating the data and putting the new equator over the desired great circle. Another possibility, the use of spherical Gaussian wavelets, will be investigated in future studies.

The input dataset, the geoid, was available in the spherical harmonic decomposition. The former method of exploration of small-scale structure, truncation of the spherical harmonic decomposition, was compared with the wavelet filter. While it was sufficient to compute only one mode of the wavelet spectrum, we had to try several truncation levels to get as many small-scale features hidden in the field as possible. The false signal in the spherical harmonics in places of low magnitude signals is a relict of their global character. The truncation method is thus very unsuitable for the detection of small-scale features. Moreover, we emphasize that the small number of the local wavelet bases will give much better resolution than the global spherical harmonic decomposition of high order in case of such inhomogeneous fields as the geoid.

In the last sections we focused on the comparison of regional small-scale structures with the geology of the Earth. The comparision was done rather carefully, as the wavelet resolution used was close to the highest degree of the spherical harmonic decomposition used, and the effect of the false signal due to truncation of the spherical harmonic decomposition could occur. Nevertheless, the Gaussian wavelet filter could detect fine features of the geoid at convergent zones, ridges, and fracture zones. The k_{max} maps were able to detect, at least to some extent, the plate tectonic history of the Earth, including present plate boundaries as well as former tectonic boundaries. After advancing to a higher-resolution geoid dataset, the correlation technique applied on the wavelet spectrum and the topography of the Earth will be a powerful tool for fast identification of areas of interest in the analyzed geoid.

As to general ideas for future research, we emphasize that the wavelet analysis might be useful for studying plate-tectonic phenomena on other planets. For example, the Venusian gravity field could be a possible target for wavelet filtering, as the field should yield information about the plume tectonics associated with the coronae (Barriot et al, 1998). The k_{max} maps of Mars could help to decipher whether plate tectonics existed on this planet in the past. Wavelet processing of extremely high-resolution geoid and topography data, down to 1 minute, together with high-resolution regional seismic tomography models will shed more light on the geodynamics under Europe.

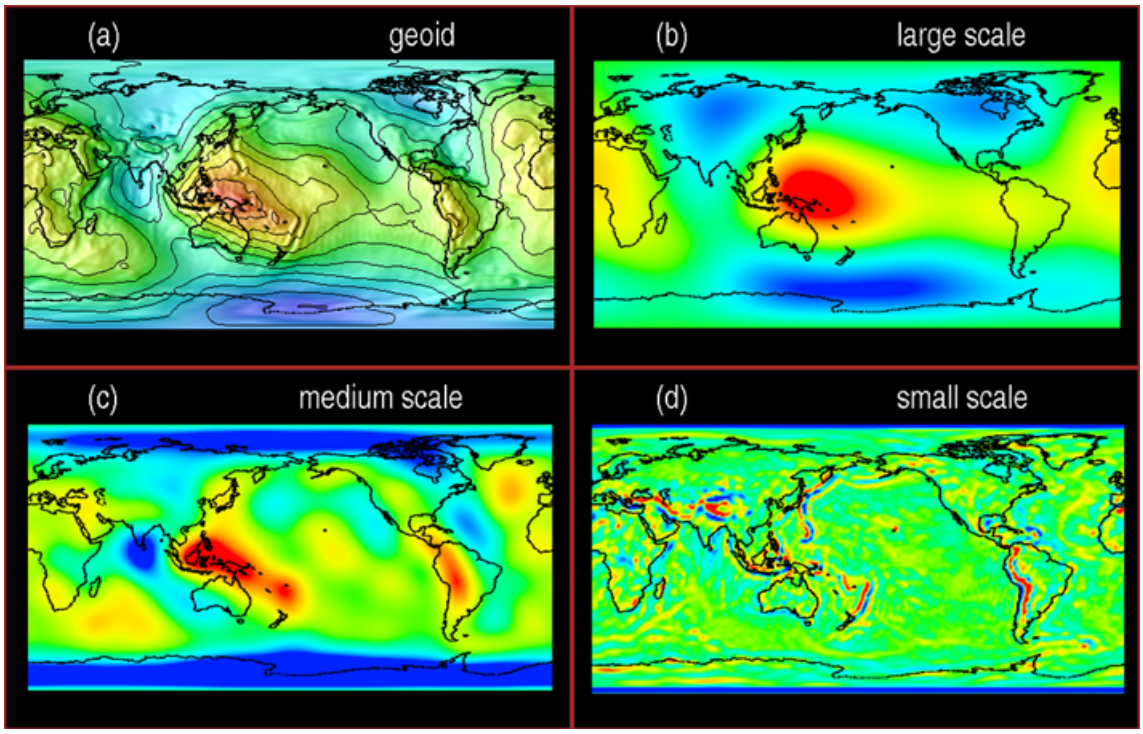

Figure 4.1. Snapshots from two-dimensional wavelet analysis of the geoid. (a) Original geoid. (b) Large scale scalogram of mode 5, (c) medium scale scalogram of mode 11, (d) small scale scalogram of mode 20. Resolution of modes given in Table 4.1. Red indicates a positive signal; blue indicates a negative one.

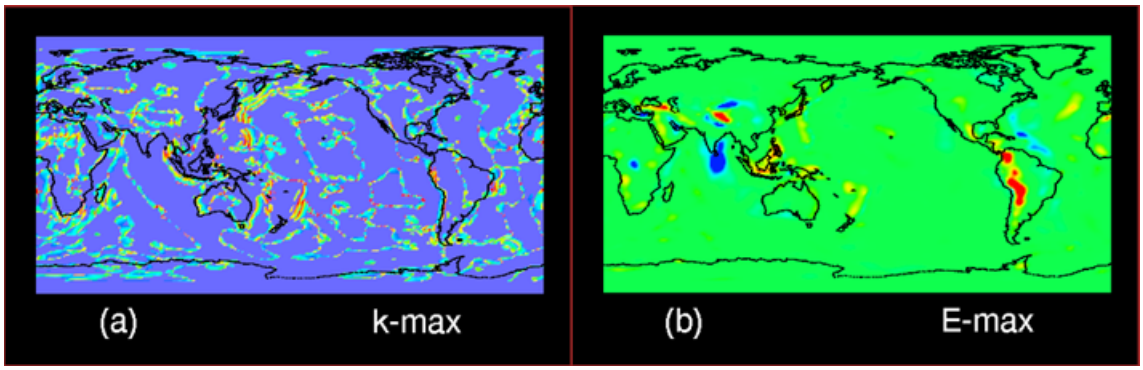

Figure 4.2. E_{max}/k_{max} analysis of the geoid using modes 15-20. Resolution of modes given in Table 4.1. Left slice (a) shows k_{max} map. Blue indicate low modes; red indicates high modes. Right slice (b) shows E_{max} map. Red indicates strong positive signals; blue indicates strong negative signals.

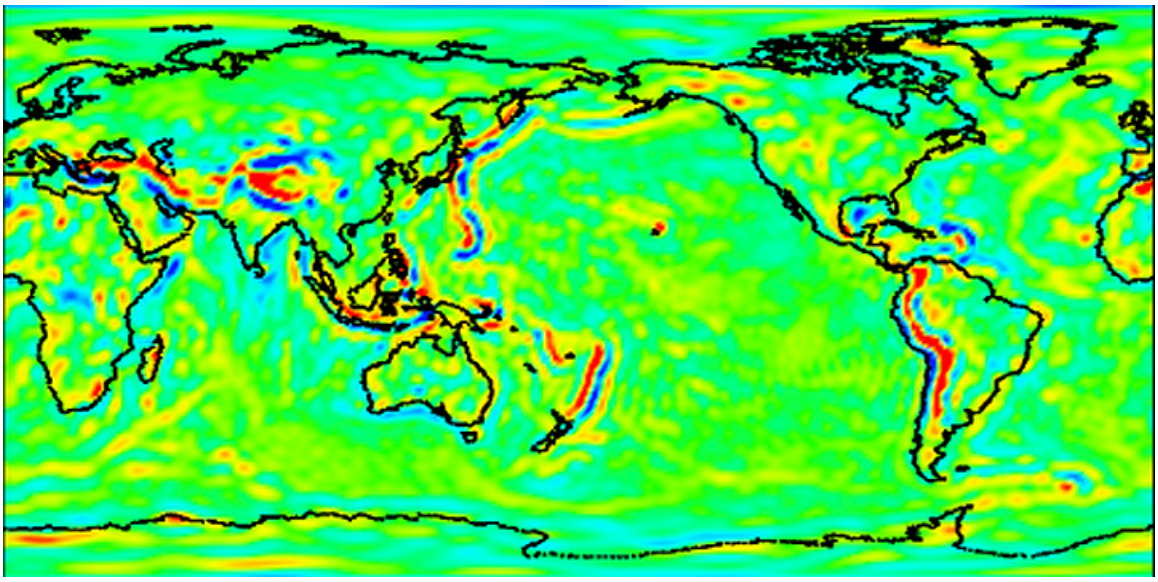

Figure 4.3. Enlargement of the Figure 4.1d.

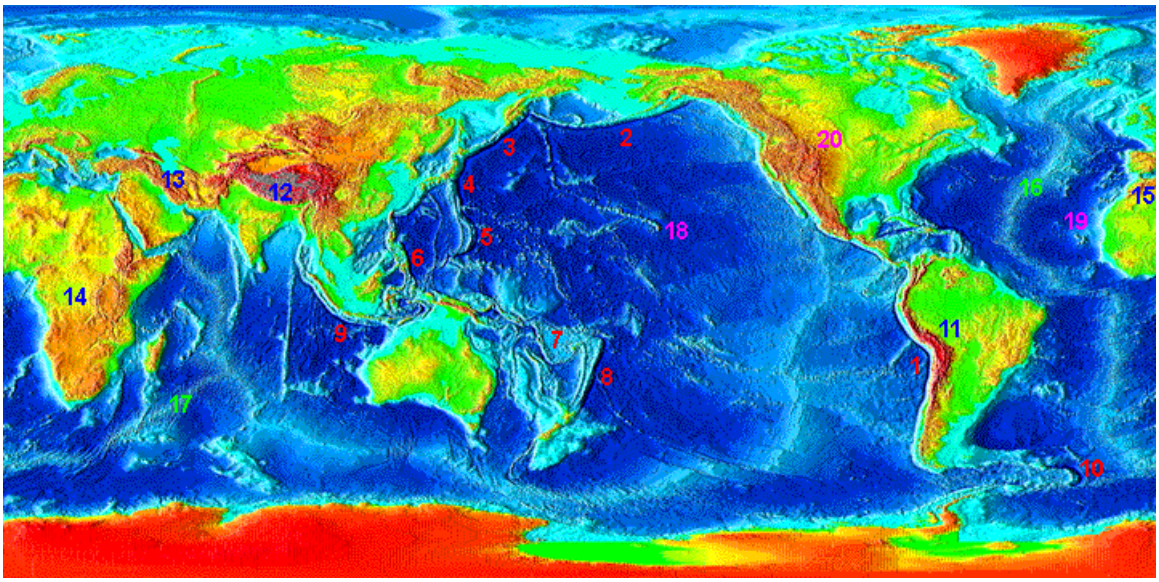

Figure 4.4. Relief of the surface of the Earth, ETOPO5 (1988). Some of the locations visible in Figure 4.3 are numbered: (1) Peru-Chile Trench, (2) Aleutian Trench, (3) Kuril Trench, (4) Japan Trench, (5) Ariana Trench, (6) Philippine Trench, (7) New Hebrides Ridge, (8) Tonga & Kermadec Trench, (9) Java Trench, (10) South Sandwich Trench, (11) Andes, (12) Himalayas, (13) Zagros Mts. (Alpine-Tethys Range), (14) Congo Basin, (15) Atlas Mts., (16) Mid-Atlantic Ridge, (17) South-West Indian Ridge, (18) Hawaii, (19) Cape Verde, (20) Yellowstone hotspot.

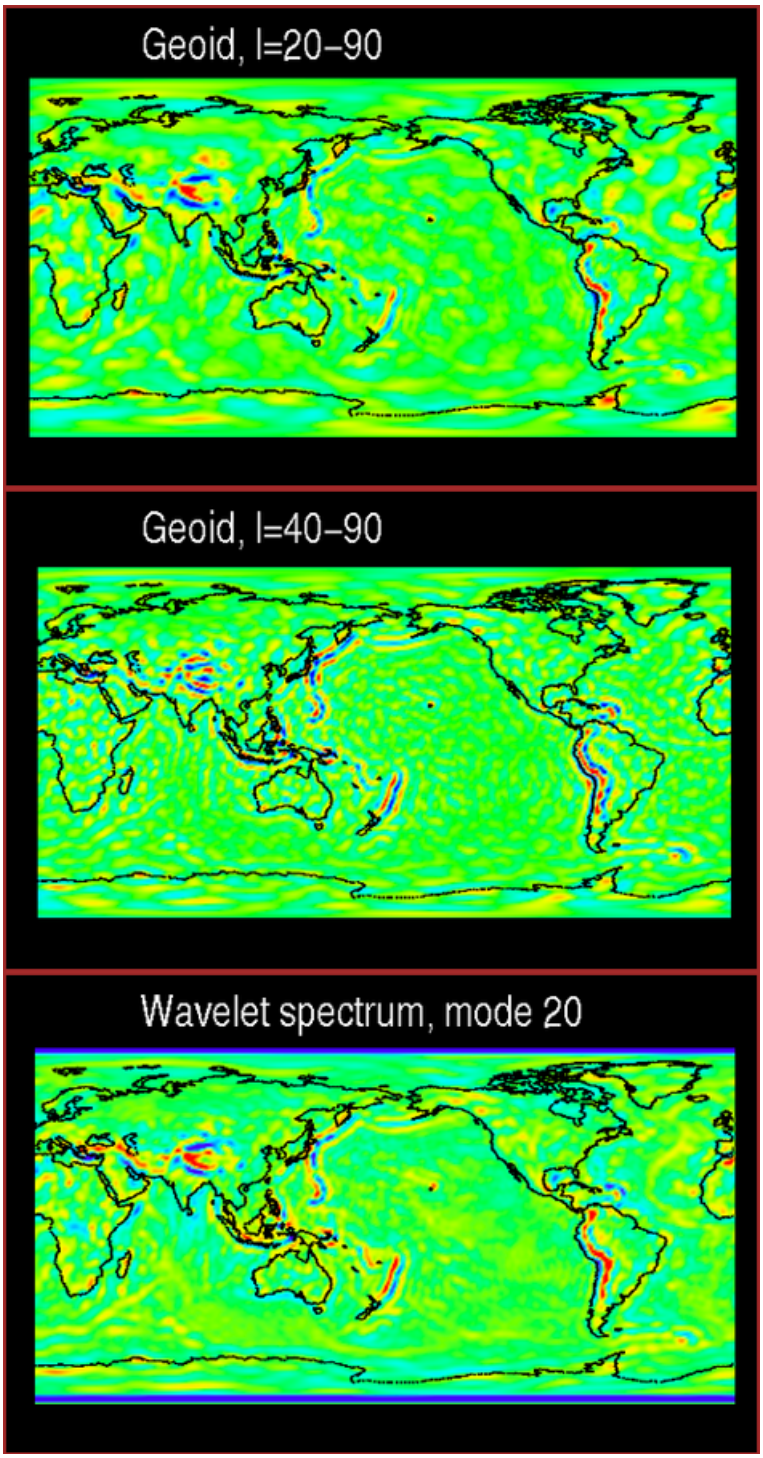

Figure 4.5. Comparison of the (a) geoid of spherical harmonic degrees 20-90, and (b) geoid of spherical harmonic degrees 40-90, with (c) wavelet spectrum of mode 20. Resolution of the mode in Table 4.1, colorscales same as Figure 4.1.

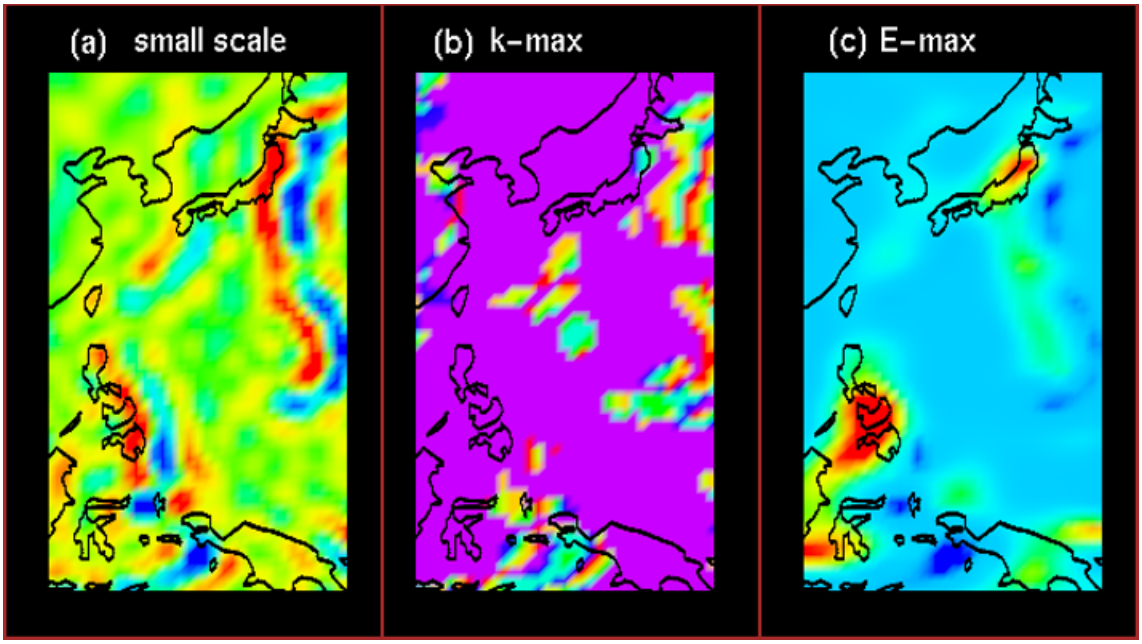

Figure 4.6. Philippine plate region. (a) Small scale (mode 20) wavelet scalogram, resolution of the mode given in Table 4.1, colorscale same as Figure 4.1d. (b) k_{max} and (c) E_{max} maps, colorscales same as Figure 4.2.

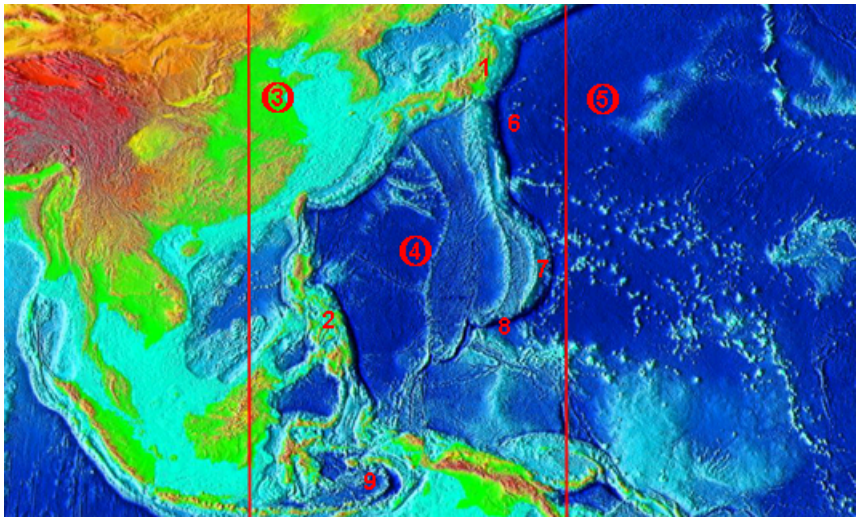

Figure 4.7. Philippine plate relief of the surface of the Earth, ETOPO5 (1988). The area used in Figure 4.6 is bounded by red lines. Locations mentioned in the text are numbered: (1) Japan, (2) Philippines, (3) Eurasian Plate, (4) Philippine Plate, (5) Pacific plate, (6) Japan Trench, (7) Mariana Trench, (8) Challenger Deep, (9) Banda Sea.

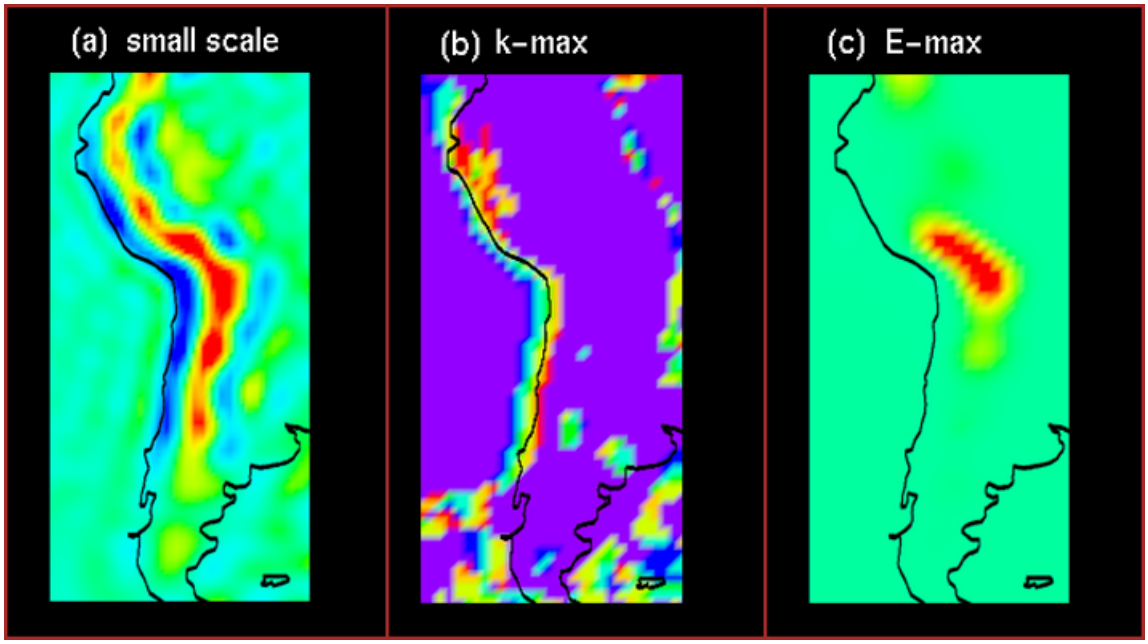

Figure 4.8. South America region. (a) Small scale (mode 20) wavelet scalogram, resolution of the mode given in Table 4.1, colorscale same as Figure 4.1d. (b) k_{max} and (c) E_{max} maps, colorscales same as Figure 4.2.

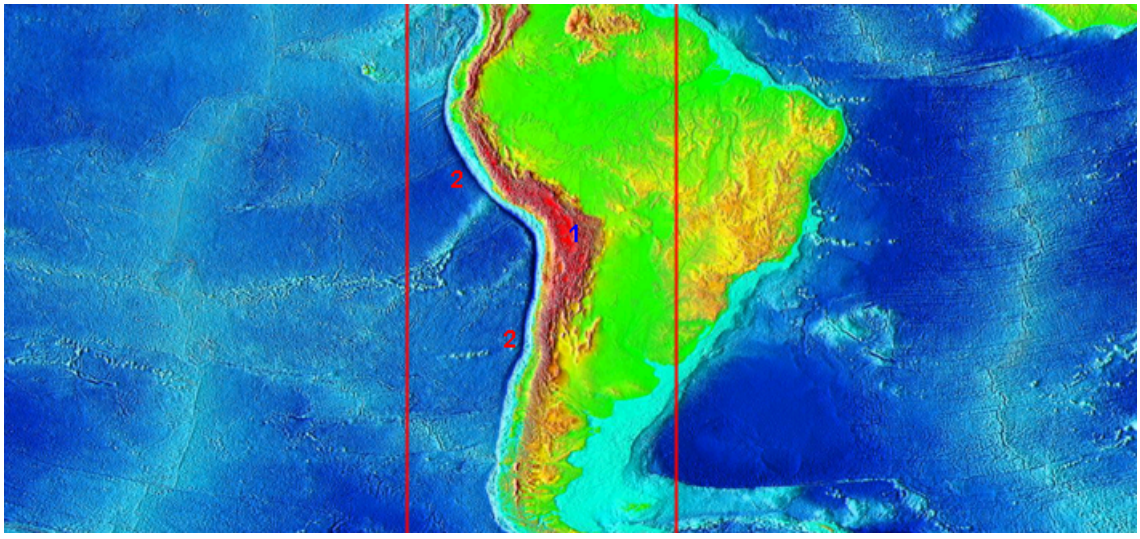

Figure 4.9. South America relief of the surface of the Earth, ETOPO5 (1988). The area used in Figure 4.8 is bounded by red lines. Locations mentioned in the text are numbered: (1) Altiplano Plateau, Andes, (2) Peru-Chile Trench.

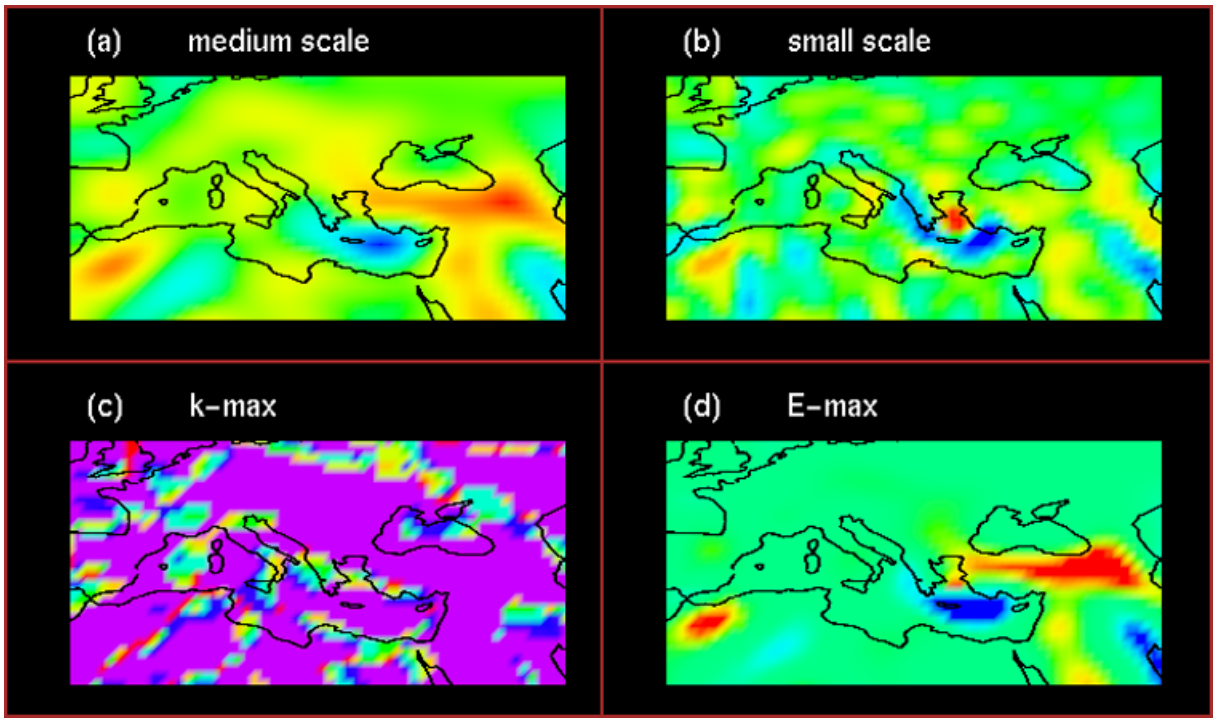

Figure 4.10. European region. (a) Medium scale (mode 15) wavelet scalogram, (b) small scale (mode 20) wavelet scalogram. Resolution of the modes given in Table 4.1, colorscales same as Figure 4.1. (c) k_{max} and (d) E_{max} maps, colorscales same as Figure 4.2.

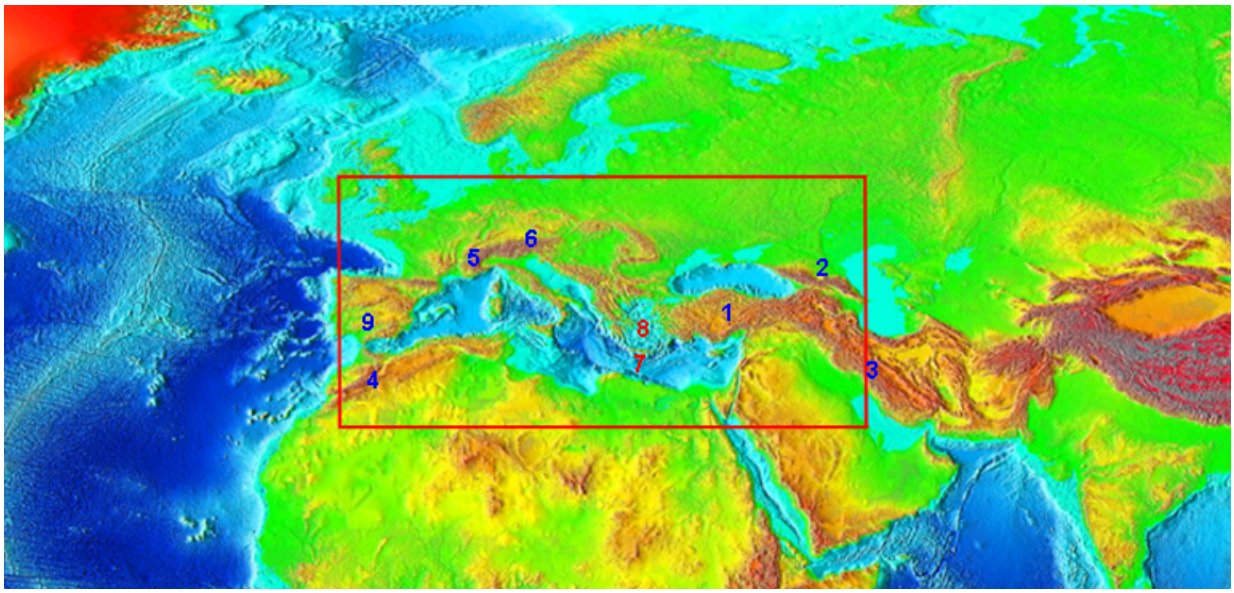

Figure 4.11. European relief of the surface of the Earth, ETOPO5 (1988). The area used in Figure 4.10 is bounded by red lines. Locations mentioned in the text are numbered: (1) Turkey, (2) Caucasus, (3) Zagros Mountains, (4) Atlas Mountains, (5) Western Alps, (6) Eastern Alps, (7) Hellenic Trench, (8) Aegean Sea, (9) Sierra Morgan.

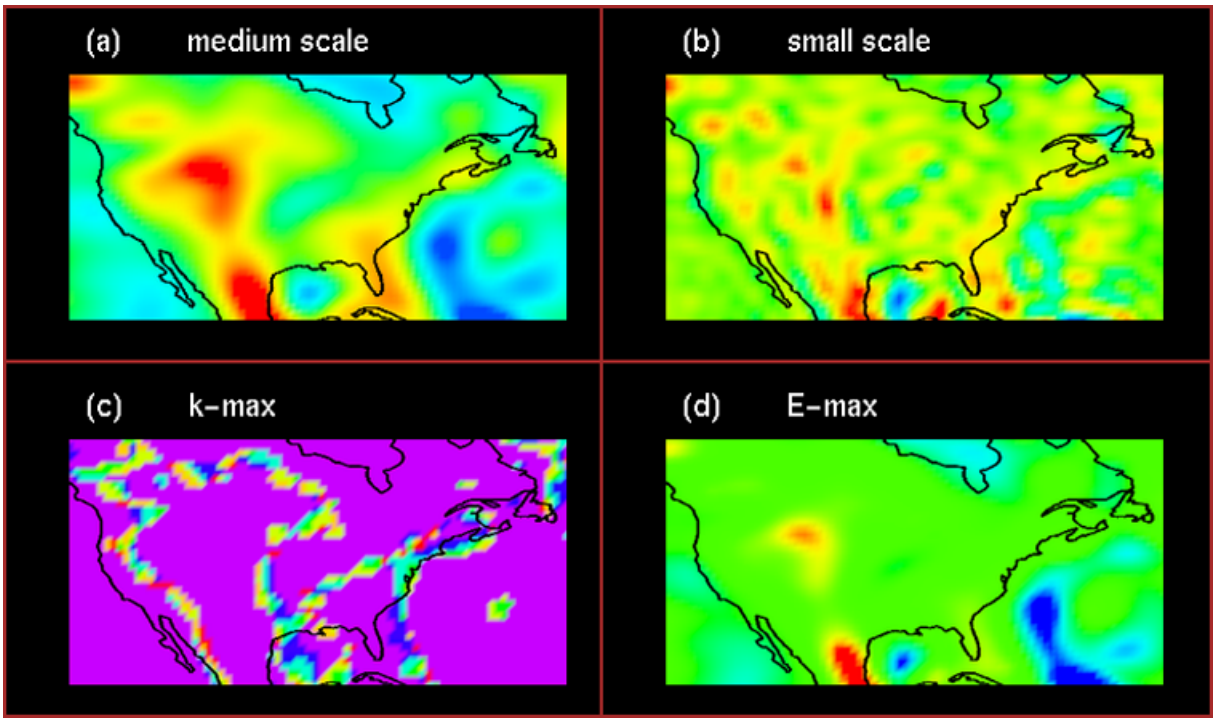

Figure 4.12. United States region. (a) Medium scale (mode 15) wavelet scalogram, (b) small scale (mode 20) wavelet scalogram. Resolution of the modes given in Table 4.1, colorscales same as Figure 4.1. (c) k_{max} and (d) E_{max} maps, colorscales same as Figure 4.2.

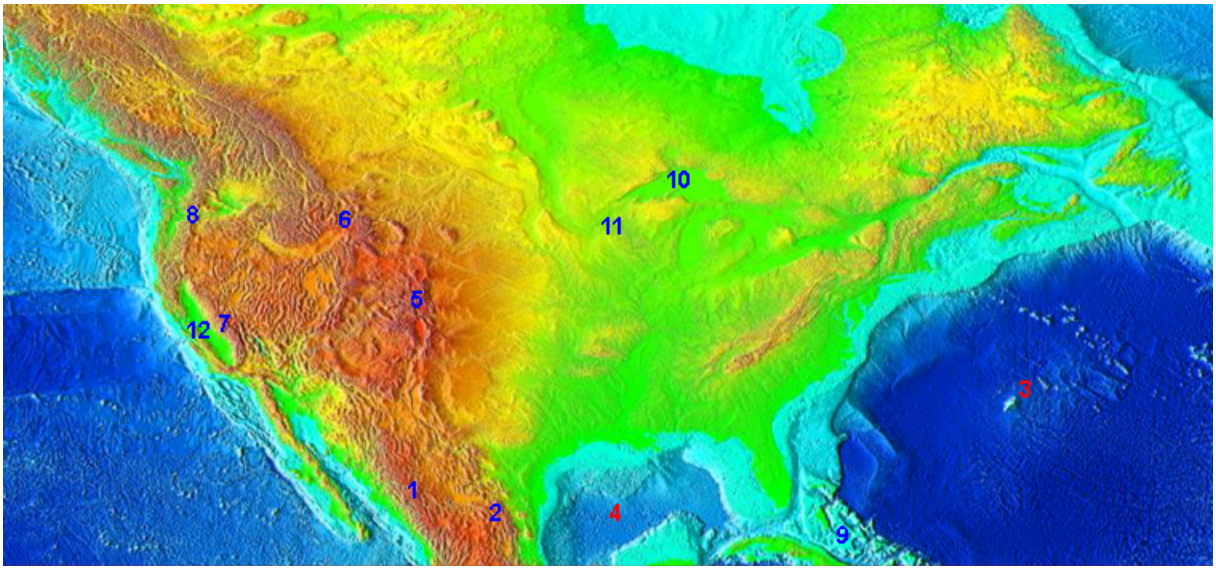

Figure 4.13. United States relief of the surface of the Earth, ETOPO5 (1988). Locations mentioned in the text are numbered: (1) Sierra Madre Occidental, (2) Sierra Madre Oriental, (3) Bermuda, (4) Gulf of Mexico, (5) Colorado Rockies, (6) Yellowstone hotspot, (7) Sierra Nevada, (8) Cascades, (9) Bahamas, (10) Lake Superior, (11) Midcontinent rift, (12) Great Valley

4.2 Mixing

4.2.1 Introduction

Mixing is a universal and ubiquitous process resulting in the homogenization of various systems. For example, mixing is a vital process in both organisms' digestive systems and in star formation. Unsurprisingly, mixing receives a great deal of interest from both scientists and engineers.

Conventionally, mixing comprises stretching, breakup and diffusion (Ottino, 1989). However, for many fluid systems stretching dominates over breakup and diffusion. This type of mixing is usually called kinematic mixing. In other words, a velocity field is the only agent driving this type of mixing. Although here we consider kinematic mixing, the method of analysis is applicable to a wide variety of non-kinematic problems.

The most common ways of monitoring and evaluating mixing are tracing techniques (e.g. Ottino, 1989). These techniques mainly rely on visualization and require two steps. The first step is visualization of the mixing, which generally involves some kind of passive tracers placed in the system (particles or dye). The second step is analysis of the tracer distribution. The simplest example of analysis is visual evaluation. However, visual evaluation is very rough and informal thus allowing for ambiguous results. Hence, the first challenging problem is to define formal criteria for describing a degree of mixing. Usually, these criteria are closely coupled to a method of monitoring. For example, evaluation methods developed for particle tracing differ from those for dye.

There are two major groups of monitoring techniques used in numerical modeling. Discrete methods place infinitely small passive particles into a flow. The particles are usually placed as a blob or blobs in various locations. As the flow evolves the particles disperse throughout the flow. Concentration and distribution of the particles may serve as a formal criterion for evaluation of mixing (Schmalzl et al., 1996). Variations of the particle method include the line method (e.g., Dritschel, 1989; Ten et al., 1998) and the method of coloring of particles in order to monitor a heterogeneous systems (Schott and Schmeling, 1998).

Field methods are another popular monitoring technique. Instead of placing discrete tracers, which carry information only about single points, one places a field which carries information about all points of the medium covered by the field. Only resolution and accuracy of the numerical technique limit the amount of information carried by the field. Thus, the field method preserves more information compared to the particles method and, consequently, is potentially much more powerful. However, it is also more demanding computationally.

Visualization of mixing is followed by the second very important stage - mixing evaluation and interpretation of the visualized mixing. Schmalzl et al. (1996) used a distribution of particles over the depth as a slightly more formalized method of evaluation. Ten et al. (1997) applied fractal dimension as a criterion for comparison of mixing in Newtonian and non-Newtonian thermal convection. A line method was used to evaluate mixing (Ten et al., 1998). A marker layer was placed in the flow, and the distribution of the layer was monitored over the depth. However, the described methods only provide integral characteristics, which evaluate overall mixing. They preserve little or no information about the locations or concentrations of the markers/field. A method preserving this information would be useful for many technical applications. The wavelet analysis presented here provides such functionality. It preserves information about both scale distributions and locations.

In this sense it delivers much more broader and detailed information about the mixing.

The method has been tested and verified on a well-documented basally heated thermal convection model. The model is of Newtonian convection in a box with an aspect ratio of 2. It utilizes temperature- and depth dependent viscosity with an effective Rayleigh number of about $2 \cdot 10^6$. The temperature dependent viscosity contrast varies by 300 across the depth of the box. The model has a depth-dependent viscosity increase by a factor of 10. Mixing is monitored by a field method. The field is placed in the box and passively advected by the velocity. The field is horizontally stratified at the initial moment and its evolution depicts the stretching and folding (mixing) in the model box.

A spline-based technique in combination with a characteristic-based method (Malevsky and Yuen, 1991) is employed to monitor the evolution of the field (Ten et al., 1996). A resolution of 3000 by 1500 bi-cubic splines is used. The field is advected with the fourth-order Runge-Kutta method.

4.2.2 Wavelet transform of the mixed field

We have used the same 2-D isotropic CWT as in the geoid section, 4.1, with the Mexican-hat as the kernel of the wavelet integral (2.6). All scales of wavelet spectra are important for mixing analysis. To avoid false large-scale signals on the edge of the box, we added layers of zero values around the box.

In order to quantify the evolution of the field, we have chosen the following tools:

- The L_1-norm of the wavelet power spectrum. We chose the norm (2.17) which yields a spectrum structure but does not distinguish the sign of the anomalies. We compute the two proxy quantities, E_{max} and k_{max}, together with the wavelet power spectrum for several time steps.
- Another useful proxy is the global spectrum of the field, especially its slope in the log-log graph, pointing to power law relationships and thus to the possible fractal structure of an analyzed field (Turcotte, 1992). We define the global wavelet power spectrum as the mean of the local wavelet spectrum over the given box :

$$W(a) = \int_0^{L_x} \int_0^{L_y} |\Psi_f(a, \vec{b})| d^2\vec{b} \tag{4.1}$$

- All mentioned quantities are defined only for a fixed time step (or a few of them). In order to study the time evolution characteristics we use the global wavelet spectrum for a given scale along with the maximum of the wavelet spectra as functions of time.

The maximum signal of the wavelet transform is found in areas surrounded by strong gradients, which appear as sharp color transitions. If the characteristic size of such a region is close to the wavelet support, then a maximum is generated. Smooth variations have only a small effect on the global wavelet spectrum compared to the high gradient surrounded areas (HGSA).

Such the behavior implies three states in dependence between wavelet scale (or wavelet 'size') and size of the HGSAs. If the support of the wavelet is much smaller than the HGSA, the contribution to the global spectrum is mostly from the edges of the HGSAs. If the wavelet support is substantially larger than the HGSAs, the wavelet function is sensitive to the mean of the field, and the wavelet spectrum can thus provide information about the global behavior of the field, such as convection cells in our case.

For wavelets fitting the HGSAs we must be aware of the more complex structure in the wavelet spectrum. If there exists a strong jump along the HGSAs' edges, the wavelet function of a given scale is more sensitive to HGSA geometry then to smooth objects. Also, mixed field structures tend to be strongly anisotropic resulting in large changes in scales with time and space. This is the reason why scale and time similarity of the wavelet spectra of the mixed field become important when the wavelet size is similar to the HGSA's size.

We have used only certain scale modes for wavelet spectrum visualization, resolution of the wavelets for the modes is shown in Table 4.1 on page 67.

4.2.3 Results of the wavelet transform for the mixed field

The question of when a field is considered mixed is complicated. This results in different definitions from different authors (Oldenburg et al., 1989; Schmalzl et al., 1996; Ten et al., 1997).

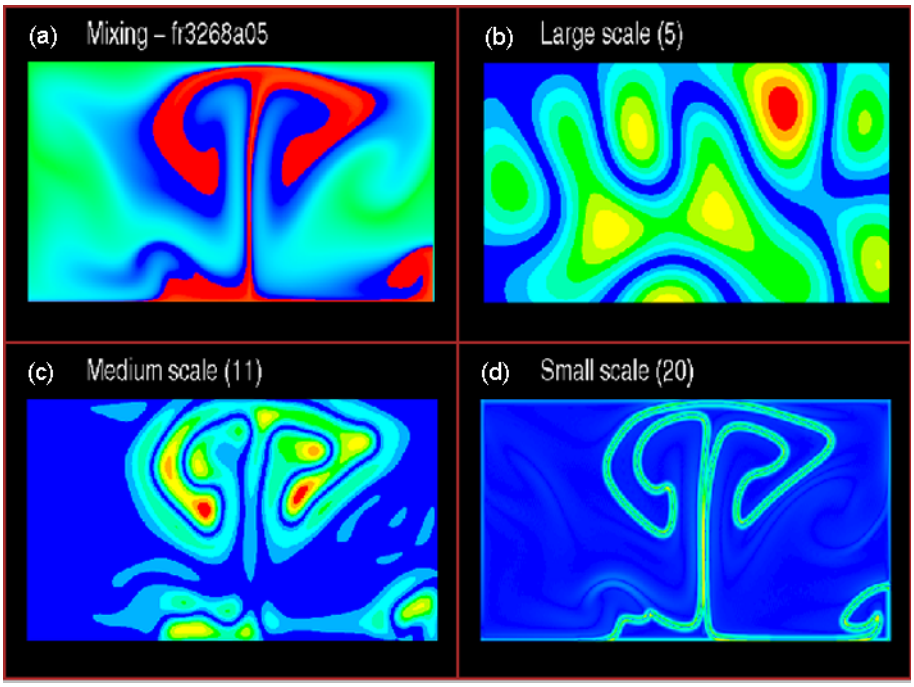

Figure 4.14. Snapshots from two-dimensional wavelet analysis of Newtonian mixing. (a) Original mixing scenario in time t_1, see Figure 4.26 for the location of the timesteps. The colorscale, from blue, green and yellow to red, is determined by values of the mixed field. (b-d) Scalogram slices for three wavelet modes. Red indicates strong (positive or negative) signal; blue indicates no signal. Resolution of modes given in Table 4.1; modes for each slice written in the parentheses.

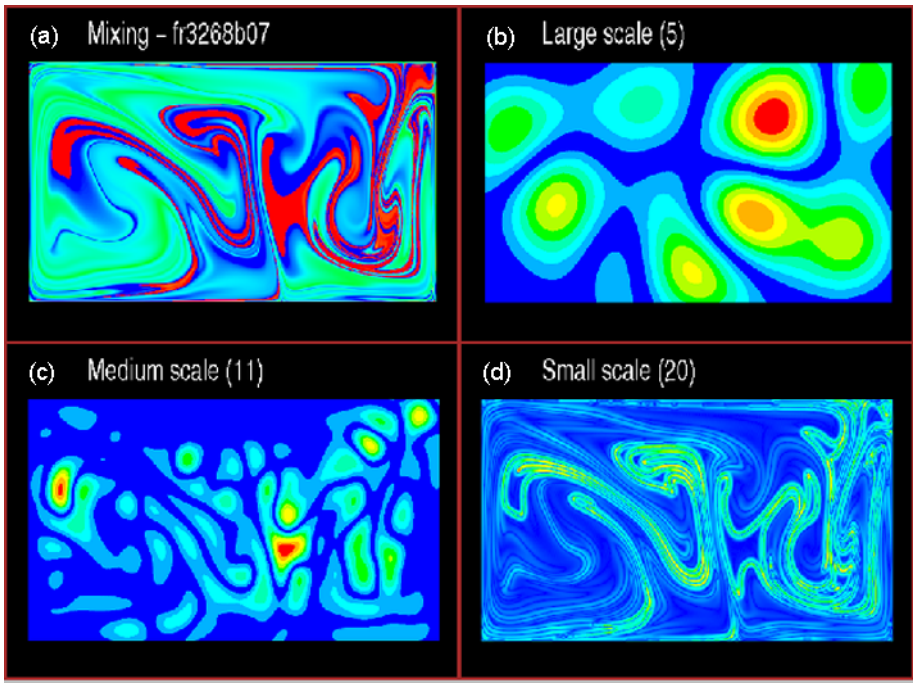

Figure 4.15. Time t_2 is portrayed, otherwise same as the Figure 4.14.

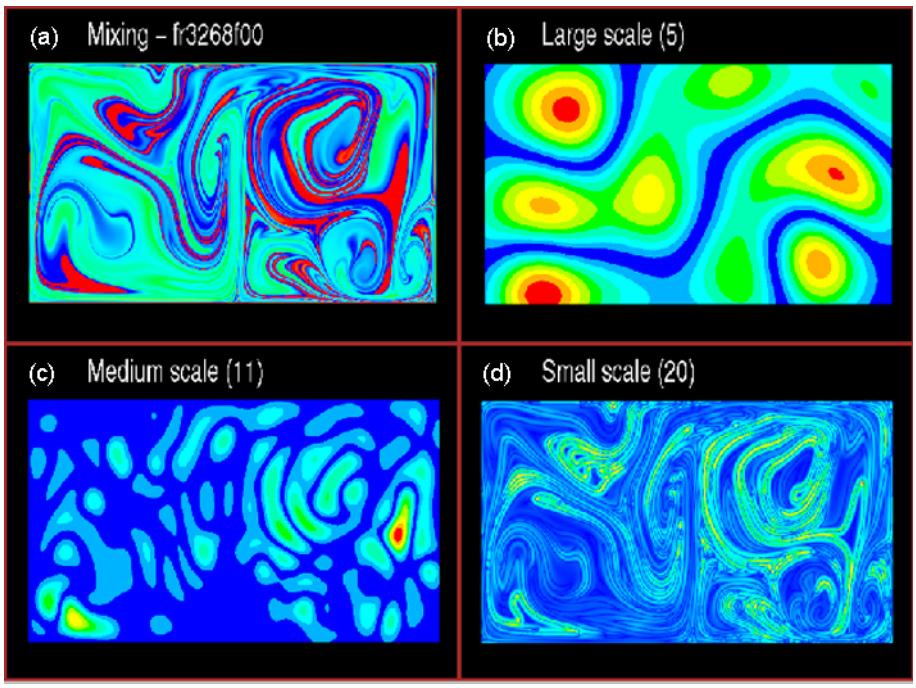

Figure 4.16. Time t_3 is portrayed, otherwise same as the Figure 4.14.

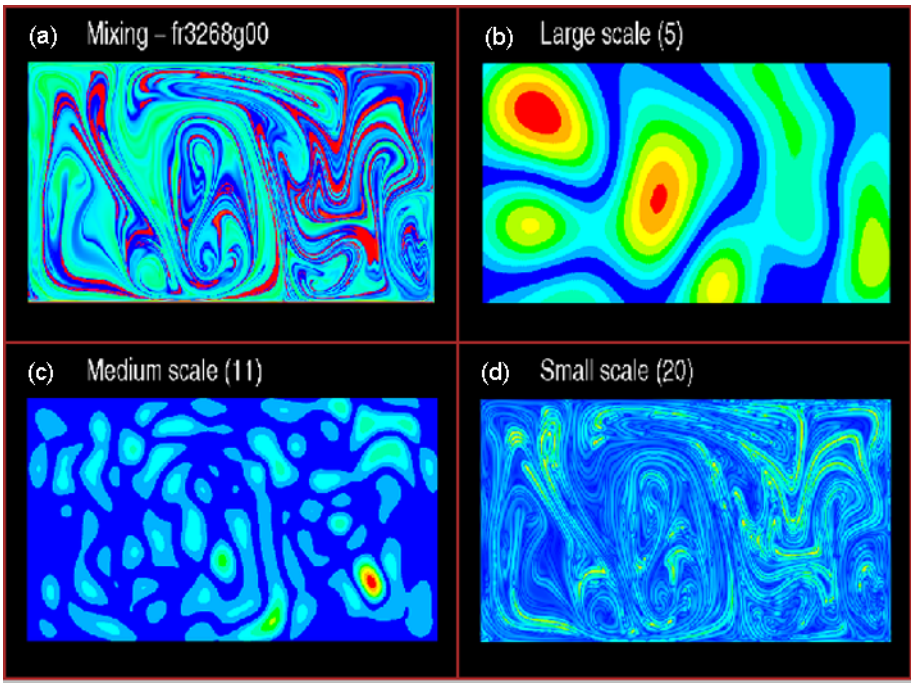

Figure 4.17. Time t_4 is portrayed, otherwise same as the Figure 4.14.

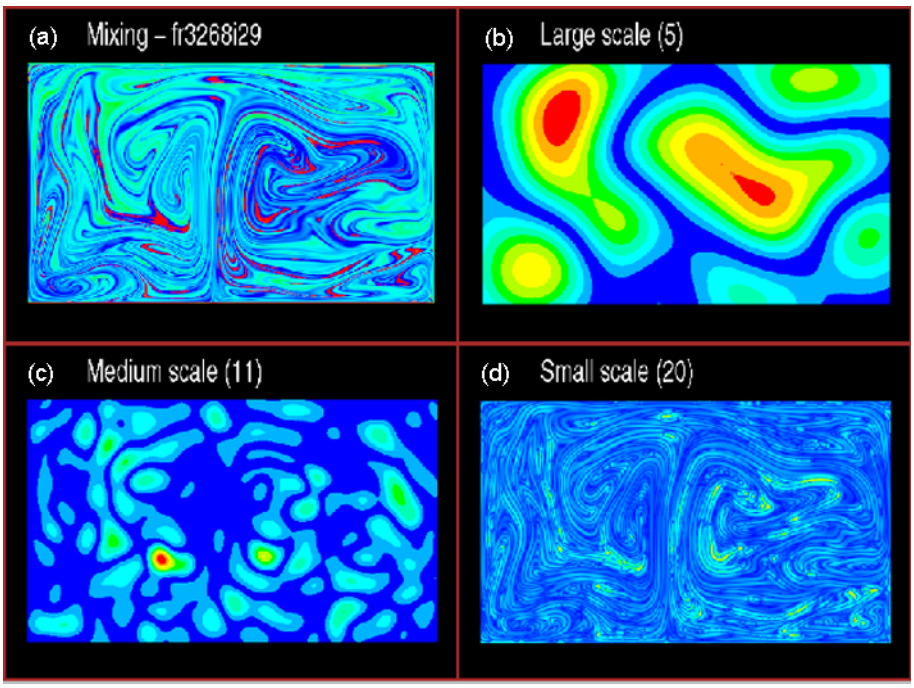

Figure 4.18. Time t_5 is portrayed, otherwise same as the Figure 4.14.

Here we demonstrate the ability of wavelets to provide insight into the time evolution of mixing.

We start with the description of the local wavelet spectra. The local wavelet spectra are shown only for five time-steps t_1 - t_5 (their locations are shown in Figure 4.26). The wavelet spectrum of the mixed field in time t_1 is displayed in Figure 4.14. The figure is divided into four panels, the left upper one is the original field, the other three panels show the L_1-norm of the wavelet spectra for three different scale modes. We note that the colormap (in comparison with the previous geoid section) now goes from blue (zero) through green and yellow to red (the global maximum of the absolute wavelet spectrum in the box in the selected fixed time).

In the large scale, mode 5 (Figure 4.14b), the original field (Figure 4.14a) is close to the end of 'rough' mixing at timestep t_1 (see Figure 4.26b). Nevertheless, the HGSA's dimensions are still similar to the dimension of the wavelet function. The strong dependence of the isotropic wavelet analysis on the shape of HGSA causes an asymmetry of the wavelet spectrum; we can see that the spectrum does not have the same structure as the original field. In the medium scale (Figure 4.14), the wavelet function just fits the red HGSAs (the wavelet is little smaller than the HGSAs). The highest values of the wavelet spectrum are on the edges of HGSAs, where the wavelet function is mostly rounded by opposite anomalies on the field. Finally, we observe a fine copy of the structure in the small-scale analysis, see mode 20 in Figure 4.14d. The wavelet function support of the small-scale mode is very thin in comparison with the dominating large structure at this first time step. The wavelet spectrum can thus pick up only the edges of the HGSAs.

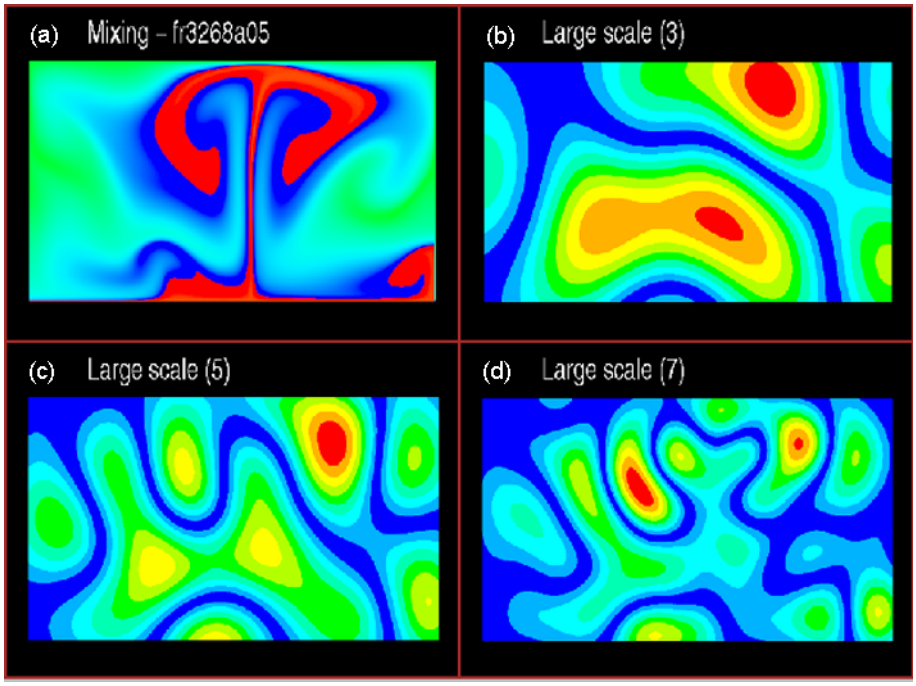

Figure 4.19. Large scales in mixing. (a) Original mixing scenario in time t_1, see Figure 4.26 for the location of the timesteps. The colorscale, from blue, green and yellow to red, is determined by values of the mixed field. (b-d) Scalogram slices for three wavelet modes. Red indicates strong (positive or negative) signal; blue indicates no signal. Resolution of modes given in Table 4.1; modes for each slice in parentheses.

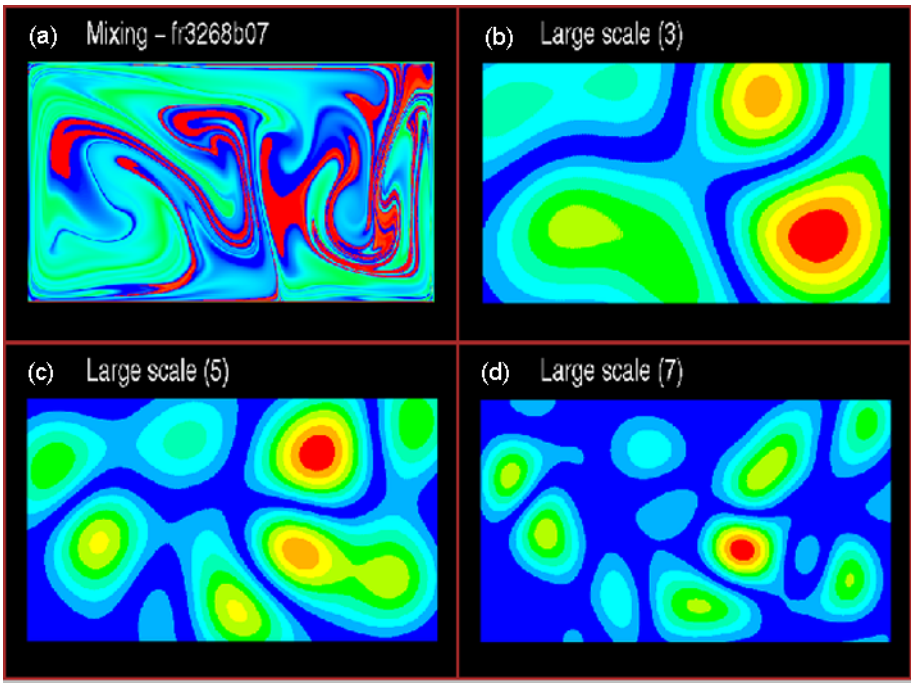

Figure 4.20. Time t_2 is portrayed, otherwise same as the Figure 4.19.

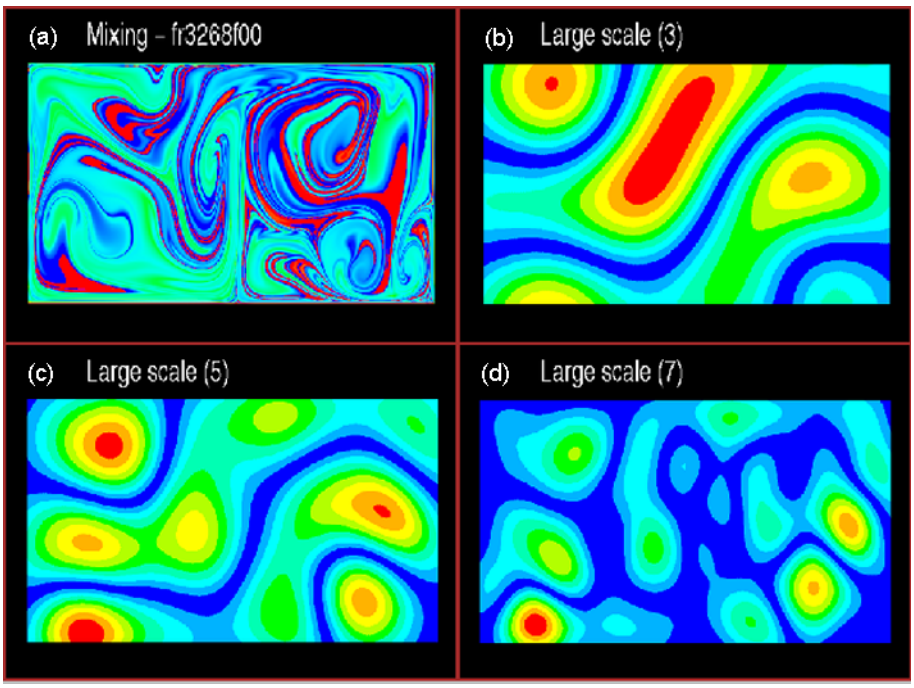

Figure 4.21. Time t_3 is portrayed, otherwise same as the Figure 4.19.

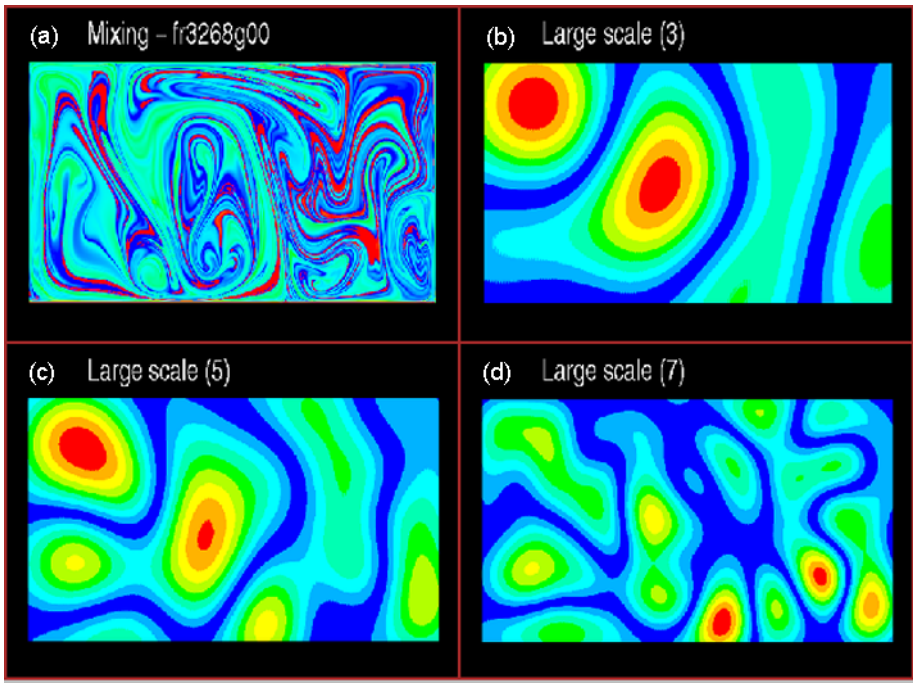

Figure 4.22. Time t_4 is portrayed, otherwise same as the Figure 4.19.

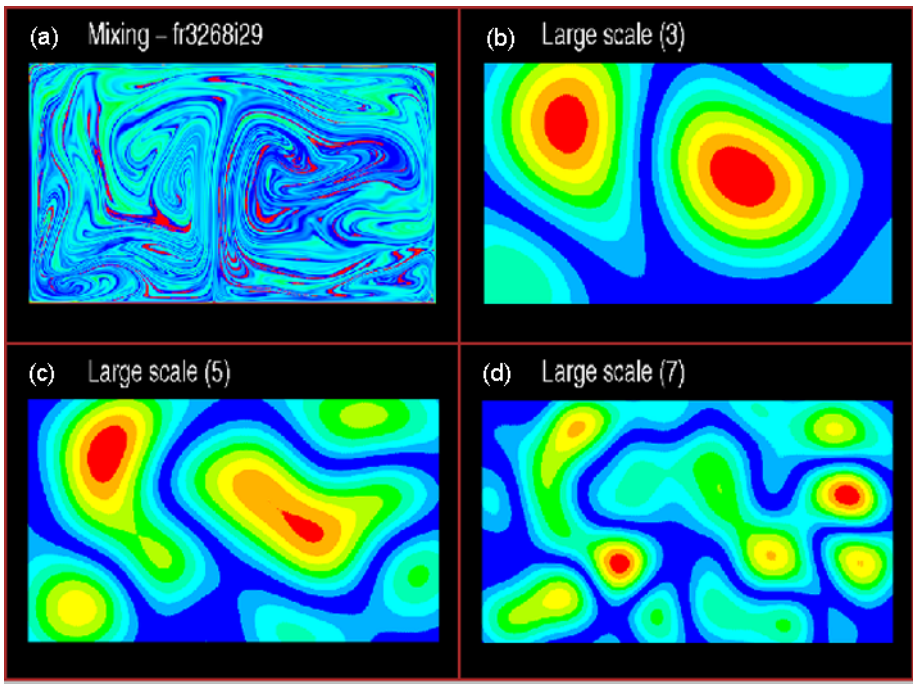

Figure 4.23. Time t_5 is portrayed, otherwise same as the Figure 4.19.

In the next timestep t_2 (Figure 4.15) all the scales reflect the more complicated behavior of the right-half of the field. While this feature persists in the two next timesteps for small scales (Figures 4.16d, 4.17d), the main power of the large-scale wavelet spectrum is moving to the left (Figures 4.16b, 4.17b), as the right part of the field becomes better mixed. Comparing HGSAs' sizes with the wavelet support we notice that the small-scale wavelets successfully detect (Figures 4.15d, 4.16b, 4.17b) not only HGSAs' edges but also entire HGSAs. The maximum value of the medium-scale wavelet spectrum (Figures 4.15c, 4.16c, 4.17c) is still generated by a few large HGSAs, which persist in the field. Moreover the medium-scale wavelets start to detect the field globally, in average, like the large-scale wavelets.

The last timestep t_5 (Figure 4.18) reveals good-mixing for large scales (Figure 4.18a). The wavelet spectrum is not influenced by the shape of the HGSAs any more, only the average density of the field plays a substantial role here. The maxima are flatter than in the previous timesteps.

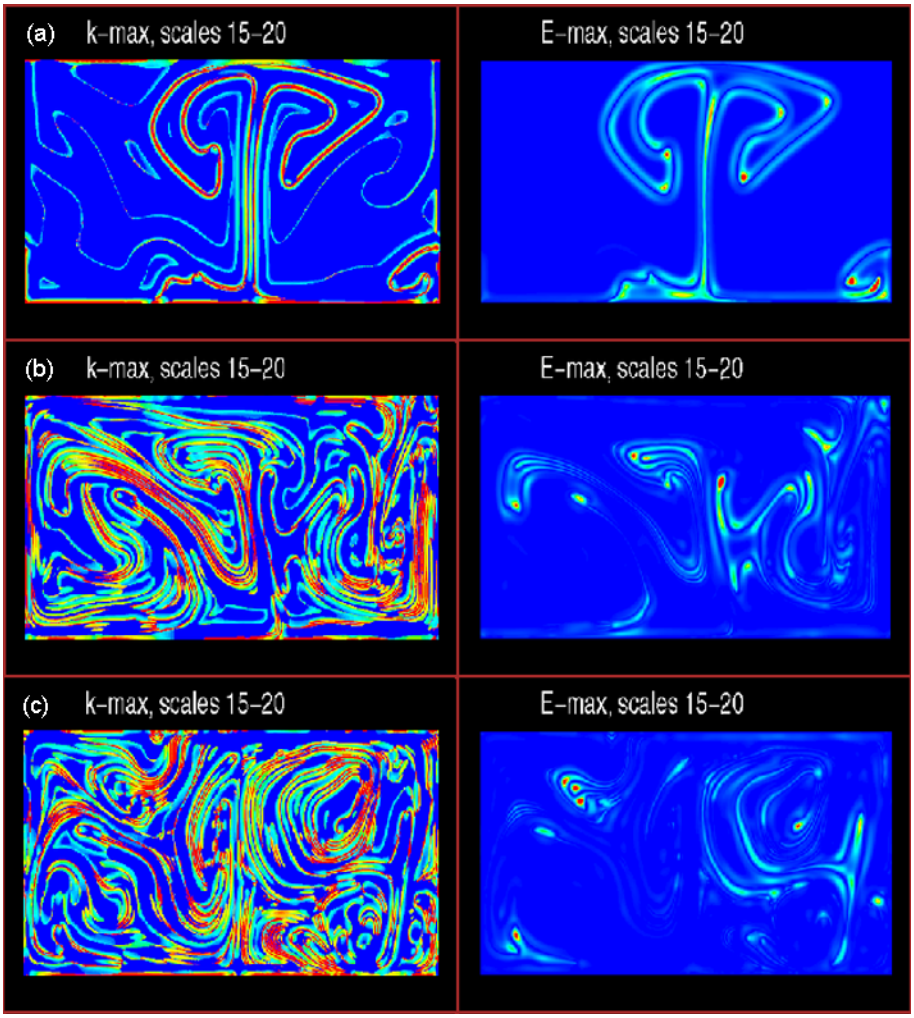

Figure 4.24. Time development of both $k_{\max}$ and $E_{\max}$ distributions taken over modes 15-20. Resolution of modes given in Table 4.1. (a-c) Times t_1-t_3, see Figure 4.26 for the locations of the timesteps. Left panels show $k_{\max}$ maps. Blue indicates low modes; red indicates high modes. Right panels show $E_{\max}$ maps. Red indicates strong (positive or negative) signals; blue indicates no signals.

They are larger and their number is lower for the large-scale mode.

The evolution of mixing can be also detected by the scale and time similarity. We can assume that the mixed field is characterized by a similar structure of close scale wavelet spectra; while the presence of the unmixed HGSAs will cause a highly sensitive dependence on the HGSAs' dimension, which will result in very different wavelet spectra on close scales. Similarly, the time evolution of the system where the HGSAs are moving and changing their shapes will cause high contrasts in temporally close spectrum snapshots on the given scale. In our studied field, the scale and time similarity is obvious in the case of large-scale structures. We compared time evolution of the modes 3, 5, and 7 (Figures 4.19-4.23). While all three scales look very different at the first timestep t_1 (Figure 4.19), the scale similarity between scales 3 and 5 develops more and more clearly, as seen in Figures 4.22 and 4.23. The time similarity is already obvious from timestep t_3 (Figure 4.21b) for mode 3 and from timestep t_4 (Figure 4.23c) for mode 5. The structure of mode 7 is not mixed even for the last computed timestep t_5, as seen in Figure 4.23d.

The last quantities used for examination of the mixed Newtonian convection field are E_{max} and k_{max}. The maximum of the local energy E_{max} and related wavenumber k_{max} were computed for small-scale range, given by modes 15-20. The E_{max} on the right panels of Figures 4.24 and 4.25, show only spots rounded with opposite field ('heads'), related mostly to the mode 15. The k_{max} figures on the left panels are more interesting. The blue color used in the colormap belongs to mode 15, red color to mode 20. Distribution of the red color thus can better pick out places with stronger gradients. We can see that after the initial rough mixing (Figure 4.24a) these places are distributed irregularly (Figure 4.24b), but with longer time evolution (Figures 4.24c, 4.25a) the coverage becomes more complex (Figure 4.25b). Thus the $k_{\max}$ maps first display large boundary areas (see long red areas) and later, after finer mixing, the large boundaries turn into local ones,

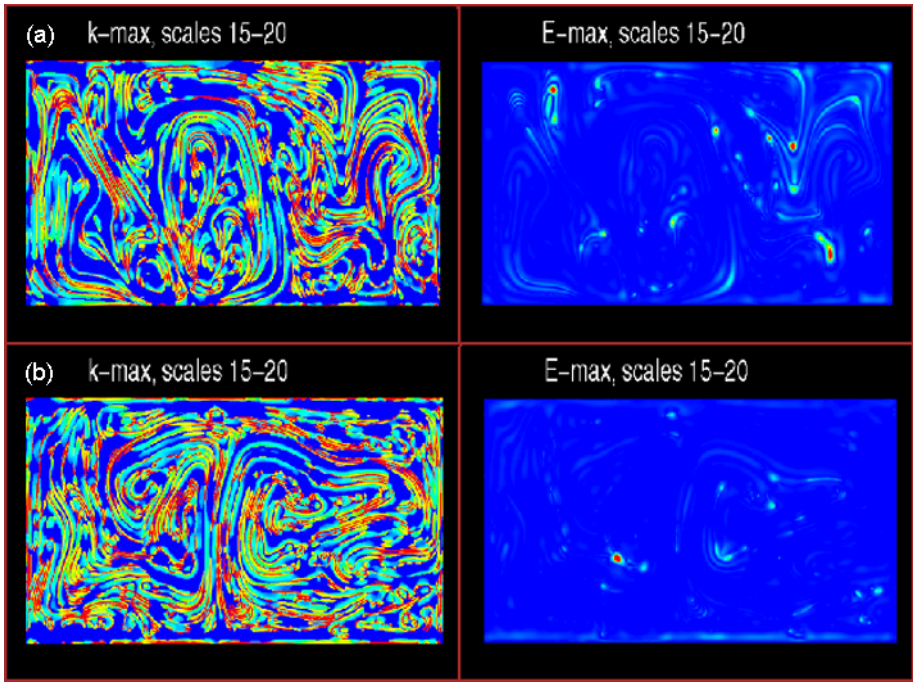

Figure 4.25. Times (a) t_4 and (b) t_5 are portrayed, otherwise same as the Figure 4.24.

and the $k_{\max}$ shows their regular distribution.

After discussion of the local features of the wavelet spectrum we will continue with global wavelet spectrum (GWS), definition (4.1). First we will focus on time evolution of the GWS for different scale modes, then we will compare log-log graphs of the GWS for the chosen timesteps t_1-t_5.

In Figure 4.26, there are plotted (blue lines) box maxima of the wavelet spectrum and (red lines) the GWS, both as a function of time, which is given by a timestep of an output slice. Circles at five timesteps correspond to the times t_1-t_5 in Figures 4.14-4.25.

What should be consider as a mixed field is a rather difficult question. If we look at large-scale modes (Figure 4.26a-c), we can try to define 'rough' mixing as a state when the first outstanding maximum is missing. In wavelet language this means that the size of the HGSAs is smaller than the size of a wavelet support. Another possible definition of a well-mixed field can be determined by a stable part of the GWS curve. Mixed fields defined as such occur for large-scale modes 3-7 (Figure 4.26a-c) at times corresponding to time-slices of about 30 to 50.

It is evident that full mixing of the field should result in zero GWS. As we can see, this state did not occur even for (relatively) long times in large-scale parts of the field (which should be mixed first). This is caused by the global behavior of the mixed field (given by the geometry and controlling parameters, which is the Rayleigh number here). Thus, although the wavelet scale is much larger then the HGSAs' sizes, the wavelet spectrum can be still non-zero. In our studied mixing convection, there are two relatively stable convection cells (see Figure 4.23a), containing different masses of the red and blue valued fields (the right cell is more blue, and the left one is more red). Therefore, although the mixing inside the cells is very intensive, the redistribution of the masses between the cells is almost negligible, which reflects in very slow (or even zero) decrease of the GWS value for long mixing times.

For medium- and small-scales it is important to note that the smaller-scale parts of the field are mixed slower. In the case of the medium-scale (mode 11, Figure 4.26d) we recognize a similar trend of the GWS as in that for large scales, only the first high peak comes later. The maximum curve is slightly different. The time evolution of the HGSAs of the medium-scale size is more complicated, which results in complex fluctuations of the maximum curve.

Using small-scale glasses (Figure 4.26e), we can very well distinguish the first linear part of the mixing convection with no (or little) HGSAs of the same size as the wavelet support. The wavelet signal is thus made mainly from HGSAs edges. We can see very slow mixing of the parts related with this small-scale mode inside the analysed time interval.

Similar features can be recognized in log-log figures of GWSs (left blue panels of Figure 4.27). The horizontal axis is the scale mode m (scale $a = exp(-0.22 \cdot m)/\pi$) and the quantity M drawn on the vertical axis is defined by $W = exp(-0.22 \cdot M)$, where W is the GWS (4.1). The right red panels show the slopes (first derivatives) of the corresponding log-log curves in the left panels. We have chosen five timesteps t_1-t_5 to show the time evolution of the log-log GWS curve. Time position of the timesteps is marked in Figure 4.26 (five circles t_1-t_5). The log-log curves show a decreasing trend of the GWS maximum (which is related to large scales) with time, and very slow changes of the small-scale parts of the curves. The log-log GWS curve goes down and becomes flatter as time increases. Later, this behavior is disrupted by the rise of the relatively stable convection cells which obstruct the large-scale mixing. In the case of the slope of the log-log GWS, we can see

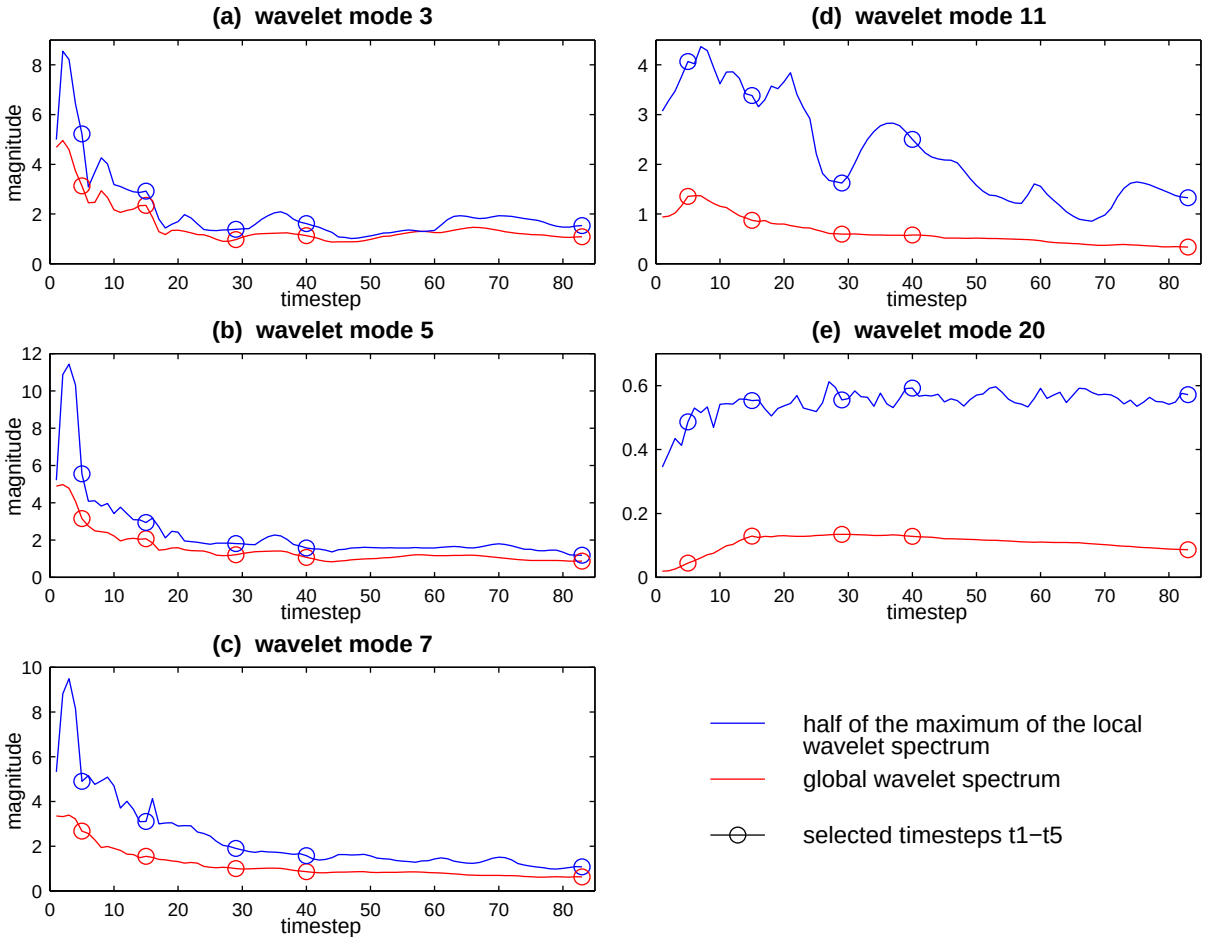

Figure 4.26. The time history of the modal coefficients from mode 3 to 20. The blue line indicates the half of the maximum of the local wavelet spectrum in the domain; while the red line represents the global wavelet spectrum (4.1), which is the average of the local wavelet spectrum. Five selected timesteps t_1-t_5 are marked by the circles.

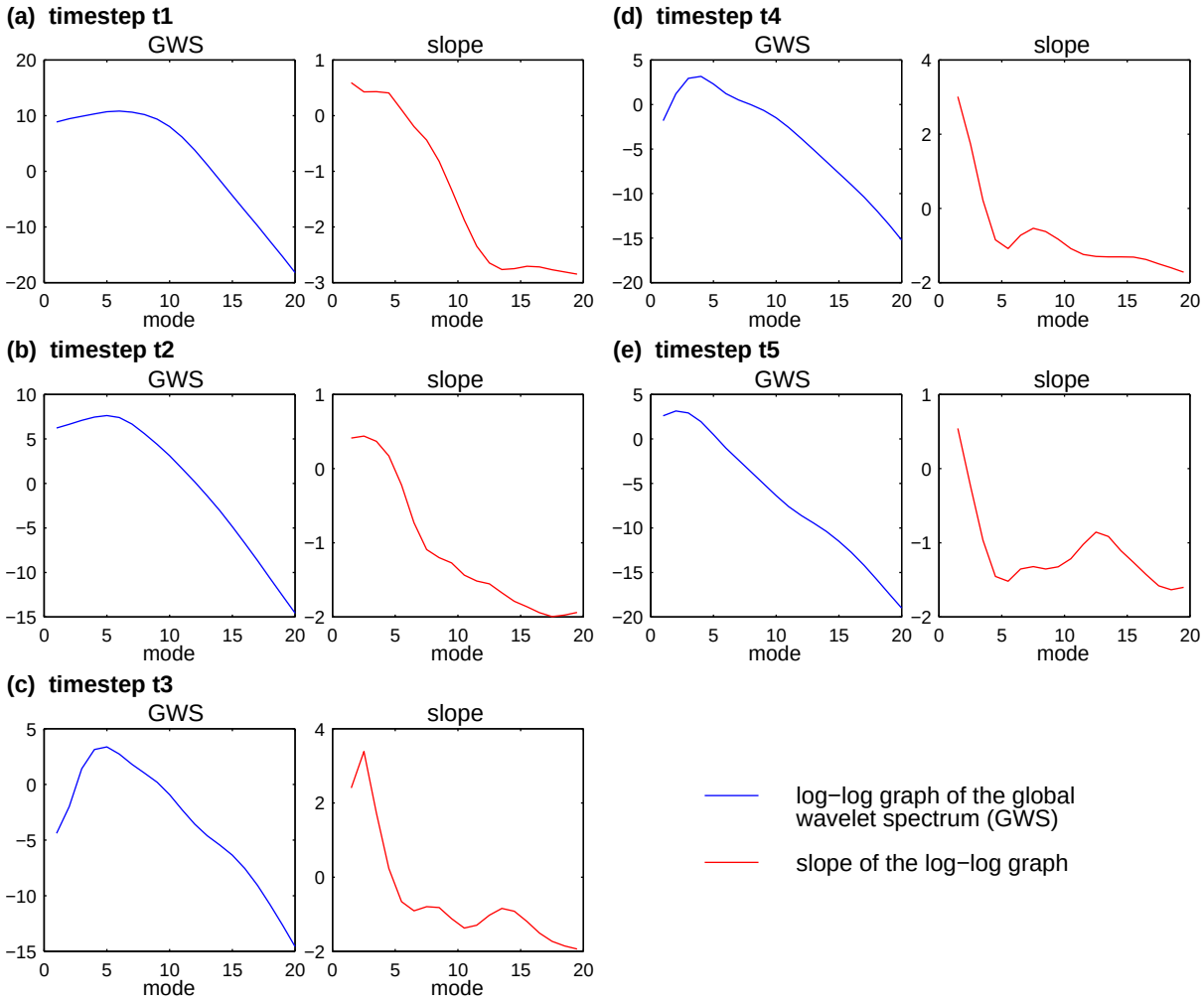

Figure 4.27. Modal decomposition of the global wavelet spectra at times t_1 to t_5. Panels with blue lines describe the logarithm of the amplitude of the wavelet transform as a function of the modes, which is the logarithm of the scale. Thus this is a log-log plot. Panels with red lines portray the slope of the curves in the log-log panels as a function of the mode (log of the scale). Times t_1 through t_5 are covered.

that the descending part of the GWS has slope between 0 and -1 for times after the first 'rough' mixing is completed.

4.2.4 Discussion and concluding remarks

In the geoid section 4.1, we focused on the most interesting part of the geoid field, the small-scale features. The analysis of the mixing with help of the wavelet transform represents a more complex problem. All scales, small, medium and large, are needed for a full description of the mixing; moreover, the time evolution of the system increases the dimension of the problem. The false wavelet signal from the boundary areas in large-scale analysis was successfully solved by adding zero layers around the convection box; the problem with time as a new dimension of the analyzed problem led to the establishment of the lower dimension global wavelet spectrum related to the Fourier spectrum. Thus, the evolution of the system was first interpreted from a rough point of view with the global spectrum and then the local wavelet spectra of several timesteps was analyzed.

The time-dependent global spectra confirmed the expected nature of the mixing, where the larger the surveyed scale the faster the mixing. The progress of the global spectra offers different definitions of the mixed field at the given scale; the field can be mixed when the first high peak in the global spectra comes to an end (we call this 'rough' mixing) or when the spectrum reaches its steady state (perfect mixing). Note that the steady character of the spectrum need not agree with the zero state, where all the components are fully mixed; especially in the case of large-scale mixing, the system can develop into a two or more cell convection regime. Although the global wavelet spectra for different scales are shifted in time, the characteristic shape of the curves looks the same for each scale. Unfortunately, we did not obtain a mixing dataset long enough to reach the steady state in small-scale global spectra.

Already in the case of the global spectra we noticed the sensitivity of the wavelet transform to the discontinuities in the analyzed field. The areas (we call them HGSA - high gradient surrounded areas) of slightly changing values bounded by a sudden jump in values became places of high wavelet signal. Presence of the HGSAs of a certain magnitude increased the value of the wavelet spectrum on the scale corresponding to this magnitude. Although the shape of the HGSAs was rapidly changing, the global spectrum mostly detected the average magnitude of the all HGSAs present in the field and thus it only registered the increasing, and later, decreasing trend of the HGSAs' evolution.

On the other hand, the local wavelet spectrum detects the HGSAs very sensitively. We defined a third possibility of how to recognize the mixed field with time and scale similarity of the local wavelet spectra. The observed similarity in large-scale wavelet spectra agreed with the steady plateau in the global spectra. As we located the similarity only subjectively, we plan to impose the correlation of the wavelet spectra to obtain more sophisticated evaluation of the similarity.

All those tools are very useful for the examination of mixing. We can easy see how mixing develops on different scales; moreover, the wavelet transform is a suitable tool for the indication of better or worse mixed parts at a certain time and scale. We can thus say that wavelet analysis is able to provide detailed information about the time and space progress of the mixing process.

4.3 Spherical shell convection wavelet analysis

4.3.1 Introduction

In this section we present the results obtained from wavelet analysis of the spherical shell convection study in Chapter 3. The spherical shell datasets were transformed to the Cartesian coordinate system and then analyzed with the Mexican-hat convolution kernel (2.14). The wavelet transform of two quantities was investigated: the temperature deviation from the conductive profile and the vorticity. Two-dimensional slices through the scalograms are presented using the signed L_1-norm of the local power spectrum (2.18).

Table 4.1 on page 67 provides the resolution of the wavelet analysis corresponding to the wavelet modes cited in each scalogram of this section. We also present signed $E_{\max}/k_{\max}$ (2.20) analyses of the temperature deviation fields.

4.3.2 Convection for $Ra = 10^6$

The temperature deviations from the conductive profile are shown in Figure 4.28a with areas hotter than the conductive profile displayed in red and those colder than the conductive profile in blue. The figure shows a coarse layering with a weakly defined hotter layer over a strong colder layer. Strong plumes are found along the edges of the box; whereas the center is dominated by weak downwellings.

Three slices of the scalogram through modes 5, 11, and 20 are presented (Figure 4.28a) with red indicating strong signals from positive structures, blue indicating strong signals from negative structures and green indicating weak signals. Mode 5 has a resolution of about 27% of the horizontal box width. Mode 11 a resolution of about 8% and mode 20 about 1%. The large-scale mode shows the gross structure of the coarse layering. It also picks up the overall division of the upper layer of the box into two regions of strong upwelling separated by a regional weak downwelling. The medium scale still shows the overall structure of hot material on top and cold on bottom, but signals of individual plume heads are beginning to appear. In the small scale, the exact shapes of individual plumes and downwellings are visible. Note that the blue surrounding individual plumes is created from the attempt to fit the wavelet function to these structures; it is not a true feature of the dataset.

The $E_{\max}/k_{\max}$ analysis for the temperature deviation of $Ra = 10^6$ is shown in Figure 4.29a. The analysis was conducted for scales ranging from mode 15 to mode 20, which correspond to 3% and 1% of the box width respectively. The $k_{\max}$ map shows low values of $k_{\max}$ in red and high values in blue. This analysis shows the ability to outline individual plumes and downwellings in the dataset. This is due to the fact that high gradients in $E_{\max}$ are associated with low $k_{\max}$. The $E_{\max}$ map shows strong positive signals in red, strong negative signals in blue, and weak signals in green. Wide areas of individual plumes are the most apparent feature in this figure.

The vorticity for the $Ra = 10^6$ run is displayed (Figure 4.28b) with positive vorticity in red and negative in blue. The vorticity has a complicated pattern; however, the features of this pattern become apparent with the wavelet analysis. The scalogram slices are shown with the same slices and colormap as for the temperature deviation. In the large scale, we can see the two main

convection cells. The medium scale shows how the two main cells are subdivided into smaller areas of circulation. The small scale shows the shear zones created by the individual plumes.

4.3.3 Convection for $Ra = 10^7$

In the temperature deviation (Figure 4.28c) we can see a coarse layering with hot on top and cold on bottom, which is better defined than for $Ra = 10^6$. Mode 5 picks up this layering. Mode 11 emphasizes this layering but also begins to pick out areas of strong upwellings separated by the weaker downwellings. Mode 20 outlines the structure of individual plumes and downwellings.

The $E_{\max}/k_{\max}$ analysis (Figure 4.29b) is done over a smaller scale, modes 18-23, than for $Ra = 10^6$. Mode 18 is about 2% of the horizontal box width, and mode 23 is about 0.5%. The $k_{\max}$ map outlines in great detail the structure of the temperature deviation field. The $E_{\max}$ map shows the shape of individual plumes and downwellings. It is similar to the small-scale scalogram slice, but downwellings are better emphasized.

The original vorticity field for $Ra = 10^7$ is shown in Figure 4.28d. Mode 5 shows that there are three large convection cells. Mode 11 shows the division of the large-scale convection cells into smaller cells. Mode 20 shows the shear zones of the individual plumes.

4.3.4 Convection for $Ra = 10^8$

The original temperature deviation field for $Ra = 10^8$ is presented in Figure 4.30a. The temperature deviation profile is more layered, indicating that the absolute temperature is better mixed than for lower Ra numbers. The hotter temperature deviations are still concentrated in the two plumes on the sides of the box, however.

Large-scale structures are no longer visible due to the high degree of mixing. Mode 11 (Figure 4.30a) picks up the concentration of heat in the two plumes on the edges of the box. Mode 15, which corresponds to about 3% of the horizontal box width, shows the wider areas of plumes, especially the plume heads along with wider areas of the downwellings. The small scale, mode 20, delineates individual plumes and downwellings. Many of the structures appear clearer than those composing the original temperature deviation field.

Modes 20-25, which correspond to a resolution of 1% to 0.5% of the horizontal box width, were used in the $E_{\max}/k_{\max}$ analysis (Figure 4.29c). The $k_{\max}$ outlines the structure of the temperature deviation field in much more detail than the small-scale scalogram slice (Figure 4.30a). $E_{\max}$ (Figure 4.29c) shows information very similar to the small-scale scalogram slice (Figure 4.30a); although only the wider areas of plumes and downwellings are emphasized.

The vorticity field for $Ra = 10^8$ (Figure 4.30b) shows the five main convection cells. These cells are shown very clearly on the large-scale scalogram slice. The medium scale shows the subdivision of these large cells into smaller circulation areas. The small scale picks out shear zones associated with individual plumes.

4.3.5 Convection for $Ra = 10^{10}$

At the high Ra number of 10^{10} the temperature deviation field is layered (Figure 4.30c), which indicates homogenization of the absolute temperature field. The medium-scale scalogram slice, mode 15, clearly shows this homogenization, but indicates that there is still a hot layer in the temperature deviation at the top and a cold one at the bottom. The small-scale slice, mode 20, begins to show the thicker area of individual plumes, especially the plume heads. The smaller scale, mode 25, which corresponds to a resolution of about 0.5% of the horizontal box width, shows the detailed structure of tiny plumes and downwellings. This structure cannot be discerned on the original temperature deviation field.

In order to better study this detailed structure we enlarged (Figure 4.31a) the center of the box in Figure 4.30c. In this enlargement, we see the detailed structure of the small-scale scalogram slice (Figure 4.30c). The greater detail towards the top of the box is due to its greater width in the spherical coordinates in which the convection simulation was conducted.

The scalogram was computed over the entire original box, and then the center of the scalogram slices were enlarged. Therefore, the resolution is associated with the width of the original box (Figure 4.30c), not that of the enlarged box (Figure 4.31a). In mode 20 (Figure 4.31b), we pick out the wider areas of plumes, many plume heads, and a few of the wider downwellings. Mode 25 (Figure 4.31c) shows the complicated pattern of individual plumes and downwellings in detail. Mode 40 (Figure 4.31d), which has a resolution of 0.05% of the horizontal width of the original box, shows numerical instabilities. This indicates that the grid size is not small enough for the thin structures. This introduces a new tool of wavelets; the ability of the very small-scale modes to pick out numerical instabilities that are not visible in the original field.

The $E_{\max}/k_{\max}$ analysis was performed for the temperature deviation field from Figure 4.30c. The analysis was computed for modes 25-30 with resolution of 0.5% to 0.1% of the horizontal width of the box in Figure 4.30c. Enlargements of the center of the $E_{\max}/k_{\max}$ dataset is shown in Figure 4.32. The $k_{\max}$ (Figure 4.32a) outlines the intricate structure of the temperature deviation field and also detects the numerical instabilities. $E_{\max}$ (Figure 4.32b) shows the wider areas of plumes and downwellings.

It is very difficult to interpret the original vorticity field for $Ra = 10^{10}$ (Figure 4.30d). The scalogram slice of mode 6, which corresponds to 22% of the horizontal box width, shows that there are large-scale convection cells. It also reveals the onset of layered convection. Mode 11 shows the divisions of the larger convection cells into smaller circulation areas, and mode 20 shows the shear zones of individual plumes and downwellings.

An enlargement of the center of the vorticity field is presented in Figure 4.33a. The enlargement of the scalogram slice of mode 20 shows the shear zones of wider plumes and downwellings. Mode 25 shows shear zones of even thinner plumes and downwellings. Mode 40 reveals even thinner shear zones while also showing the presence of numerical instabilities.

4.3.6 Convection for $Ra = 10^{11}$

The temperature field for $Ra = 10^{11}$ (Figure 4.34a) shows very fine layering, indicating even higher homogenization of the absolute temperature. The scalogram slice of mode 15 (Figure 4.34b)

emphasizes this homogenization and demonstrates that there is still layering in the temperature deviation, with a hot anomaly at the top and a cold anomaly at the bottom. Mode 20 (Figure 4.34c) shows the wider areas of plumes and downwellings, which are hinted at in the original temperature deviation field in Figure 4.34a. Mode 25 (Figure 4.34d) shows an intricate filigree structure of thin plumes and downwellings. We see that the temperature deviation field behaves as a mixing system rather than a convection cell system.

An enlargement (Figure 4.34a) of the center of the original temperature deviation (Figure 4.33a) shows that the field has a complicated structure. Numerical instabilities can also be seen in this enlargement. The enlargement of the scalogram slice of mode 20 (Figure 4.34b) shows the wider areas of plumes and downwellings which create the complicated structure of the original field. Mode 25 shows even thinner structures. Mode 30, which corresponds to a resolution of about 0.1% of the horizontal width of the box in Figure 4.34a, shows the complicated filigree structure, and the existence of instabilities.

Figure 4.35a is a further enlargement to clearly emphasize the detailed nature of the temperature deviation field. This enlargement also clearly shows the numerical instabilities. The further enlargement of the scalogram slice of mode 30 (Figure 4.35b) shows the detailed nature of the mixing structure along with clearly pointing out the existence of numerical instabilities. The enlargement of the scalogram slice of mode 40 (Figure 4.35c) emphasizes the details of the numerical instabilities.

The vorticity field (Figure 4.33b) for $Ra = 10^{11}$ is so complicated that it is hard to investigate. The scalogram slice of mode 11, however, reveals the existence of horizontally orientated circulation cells. It clearly shows that a mechanism of layered convection is present in this strongly turbulent convection. In mode 15 we see a finer subdivision of the circulation cells shown in mode 11. In mode 20, the structures picked out are so tiny that the figure is difficult to interpret. Careful examination, however, indicates that these tiny circulation cells are shear zones associated with the mixing structure of the temperature deviation field.

4.3.7 Discussion and concluding remarks

In Chapter 3 we presented different thermal convection regimes as the Rayleigh number was changing. To get more information about the convection systems, we applied the 2-D wavelet transform to the temperature and vorticity fields. The complexity of the analyzed problem increased throughout this chapter, the geoid section embraced only one field, the time evolution of the mixed field brought another dimension to the problem, and here the Rayleigh number as the parameter controlling the regime of the convection intensified the variability of the problem. Therefore, the wavelet analysis is a very helpful tool, which is suitable not only for a certain scale, but can easily show the structure at all scales, small, medium, and large.

We started the wavelet analysis with the $Ra = 10^6$ run, and continued with higher Rayleigh numbers, as the structure of the temperature and vorticity fields became more complex, which required the power of wavelets. The scalograms of the temperature fields were not very interesting at first, the large-scale analysis showed only the simple structure of the layered convection, the small-scale analysis detected the same plumes as one can also see with the 'naked eye'. The power of the technique is shown for high and ultra-high Rayleigh numbers convection; the temperature

field is already so complex that the wavelet filter helps to visualizate the fine structure of the field. A much more powerful tool for depicting the plumes and also their remains is the E_{max}/k_{max} analysis, where k_{max} maps reveal not only the plumes themselves but also places of the intensive plume collisions. Another useful application of the small-scale wavelet transform was found in the retrieval of the areas of numerical instabilities in ultra-high Ra convection.

The most important effects were revealed by means of the wavelet analysis of the vorticity. The small-scale structure of the vorticity is the same as in the temperature field, but the large-scale analysis show the large convection cells, which become more and more hidden in the original field for higher Rayleigh numbers. The wavelet spectra of the vorticity fields are in great agreement with the results from Chapter 3. The loss of the two-cell character of the convection for Rayleigh numbers higher than 10^6 was confirmed, moreover, we can determine a number of cells, 3 for the $Ra = 10^7$ convection and 6 for the $Ra = 10^8$ one. The qualitative change of the regime when $Ra = 10^{10}$ run finished in the layered convection state resulted in a check-like texture of the large-scale wavelet transform of the vorticity field. The transition state of the still unfinished 10^{11} run is characterized by a horizontal layering of the vorticity of the large scales, with the beginning of separation into small convection cells.

We can see that the 2-D wavelet transform can successfully complete the analysis of the convection regimes, either by testifying to features observed from the long temporal evolution of the system or by the discovery of structures hidden from the human eye.

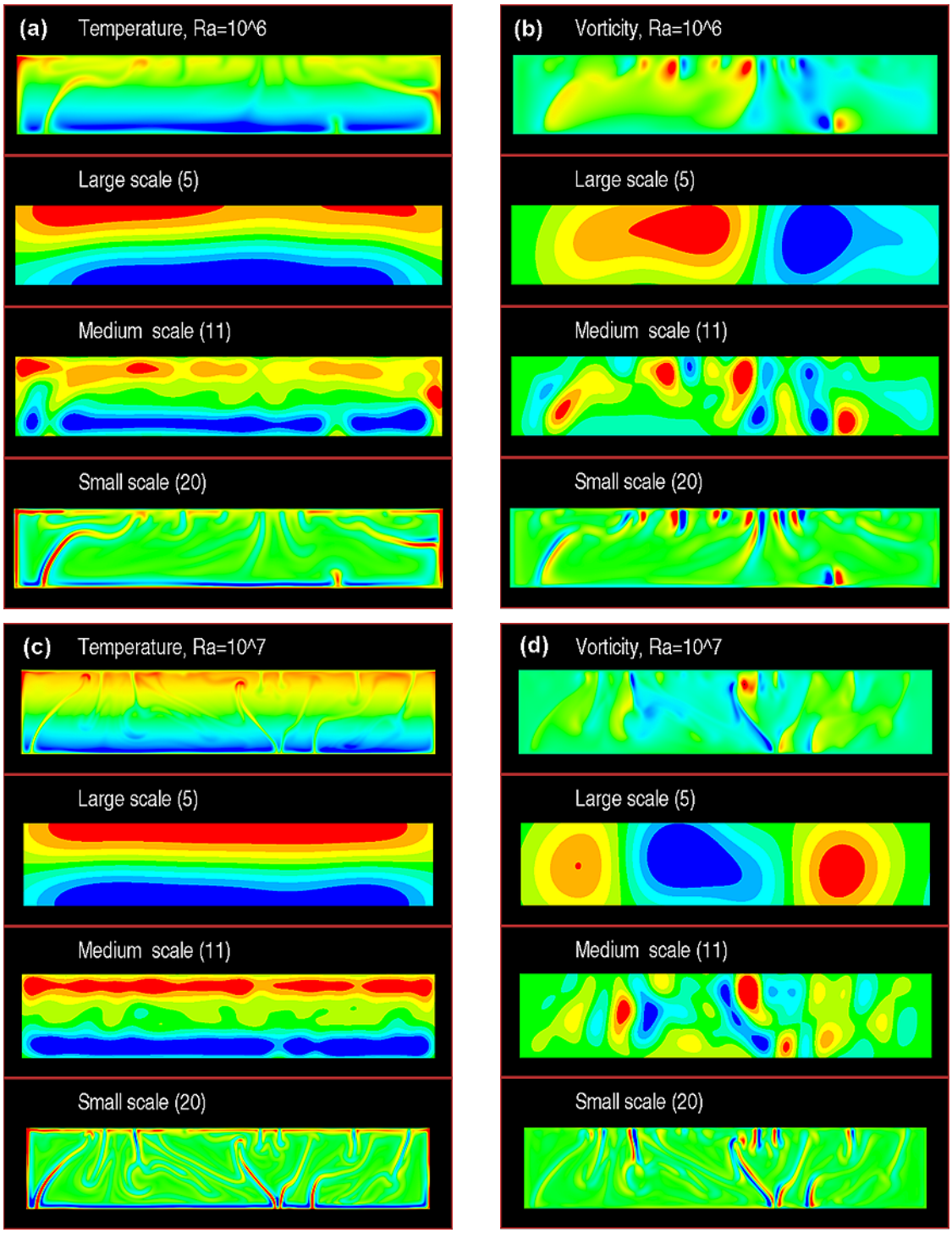

Figure 4.28. Temperature deviations and vorticity fields for (a)-(b) $Ra = 10^6$ and (c)-(d) $Ra = 10^7$. Top slices are original datasets for each panel. Panels (a),(c): red indicates areas hotter than the conductive profile; blue indicates colder areas. Panels (b),(d): red indicates positive vorticity; blue indicates negative vorticity. Other slices show scalograms through three wavelet modes. Red indicates strong positive signals; blue indicates strong negative signals. Resolution of the modes given in Table 4.1; modes for each slice in parentheses.

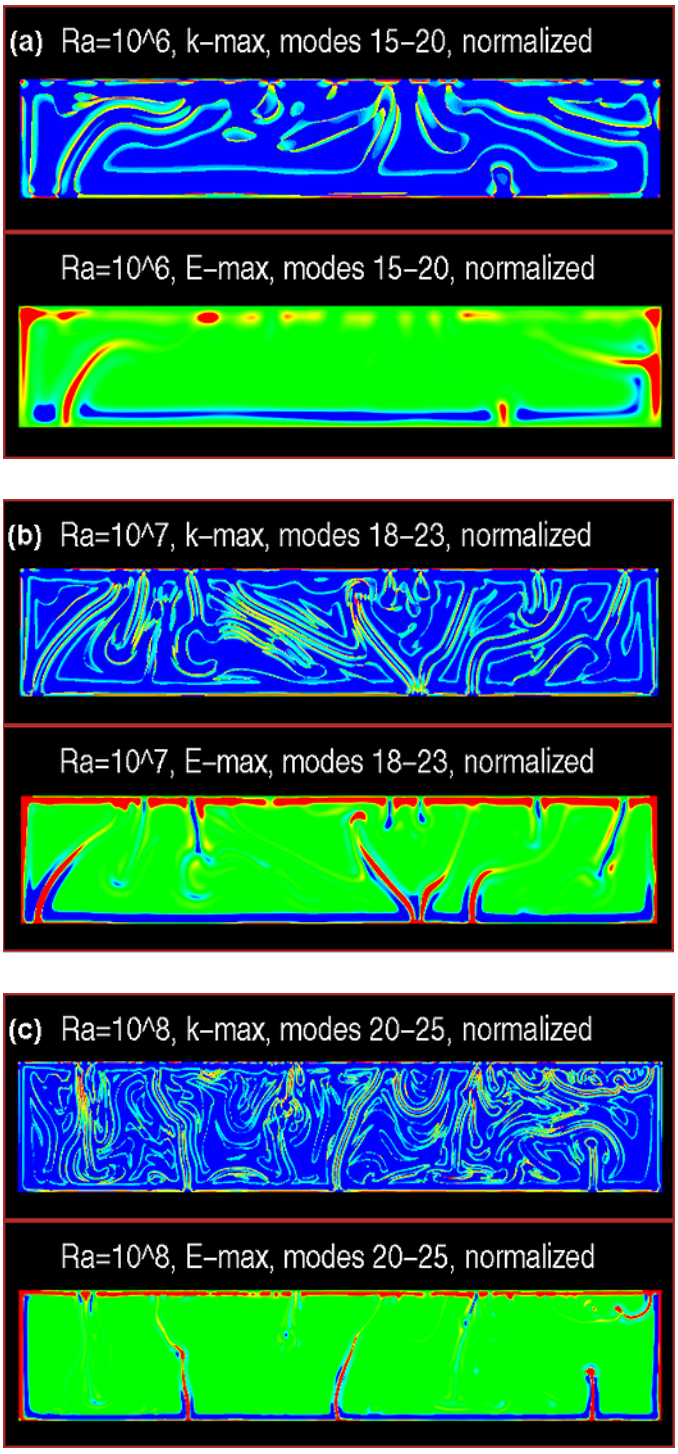

Figure 4.29. $E_{\max}/k_{\max}$ analysis for (a) $Ra = 10^6$, (b) $Ra = 10^7$, (c) $Ra = 10^8$ using modes 15-20. Resolution of modes given in Table 4.1. Top slices show $k_{\max}$ maps. Blue indicates low modes; red indicates high modes. Bottom slices show $E_{\max}$ maps. Red indicates strong positive signals; blue indicates strong negative signals.

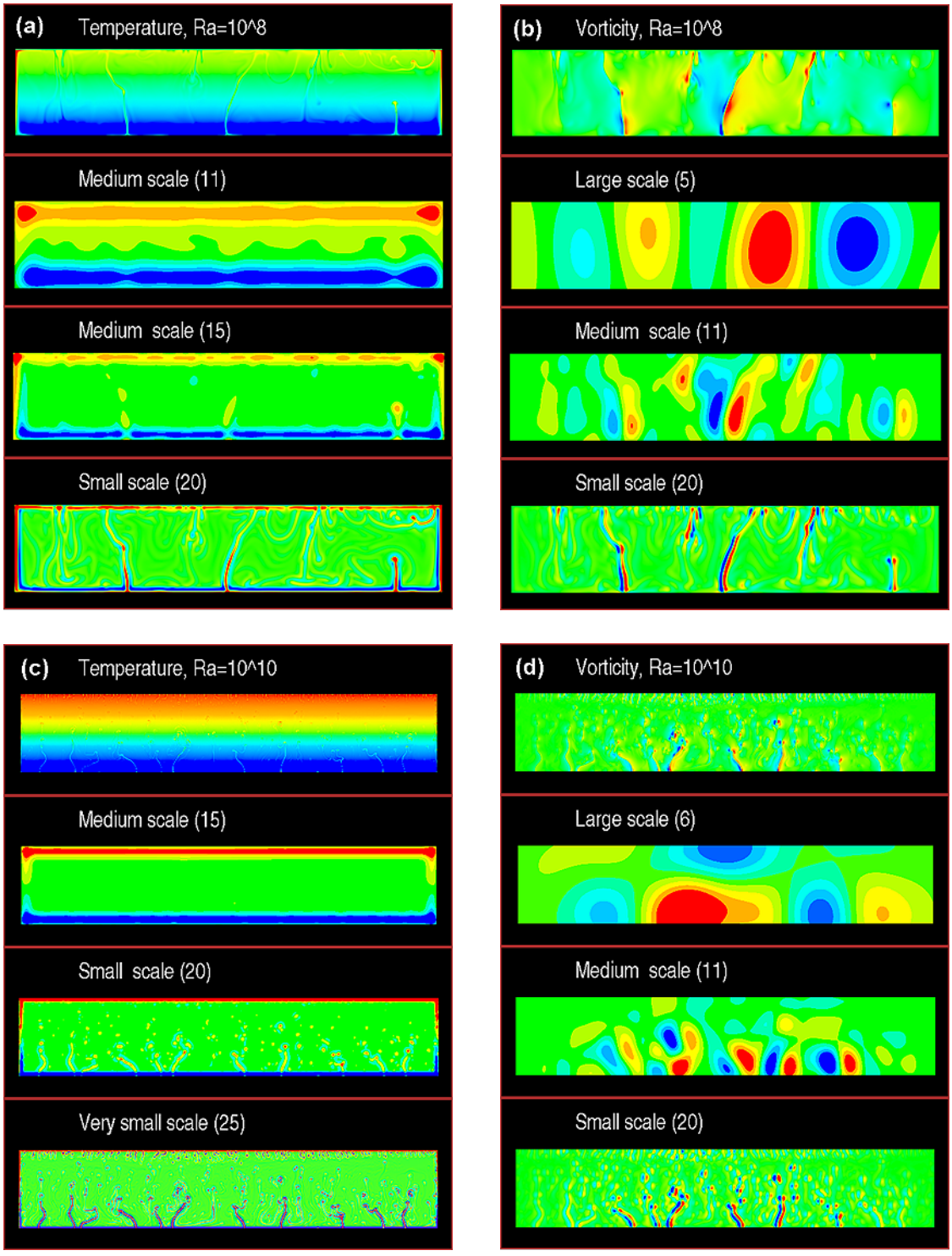

Figure 4.30. Temperature deviations and vorticity fields for (a)-(b) $Ra = 10^8$ and (c)-(d) $Ra = 10^{10}$. Top slices are original datasets for each panel. Other slices show scalograms through three wavelet modes. Colorscales same as Figure 4.28. Resolution of the modes given in Table 4.1; modes for each slice in parentheses.

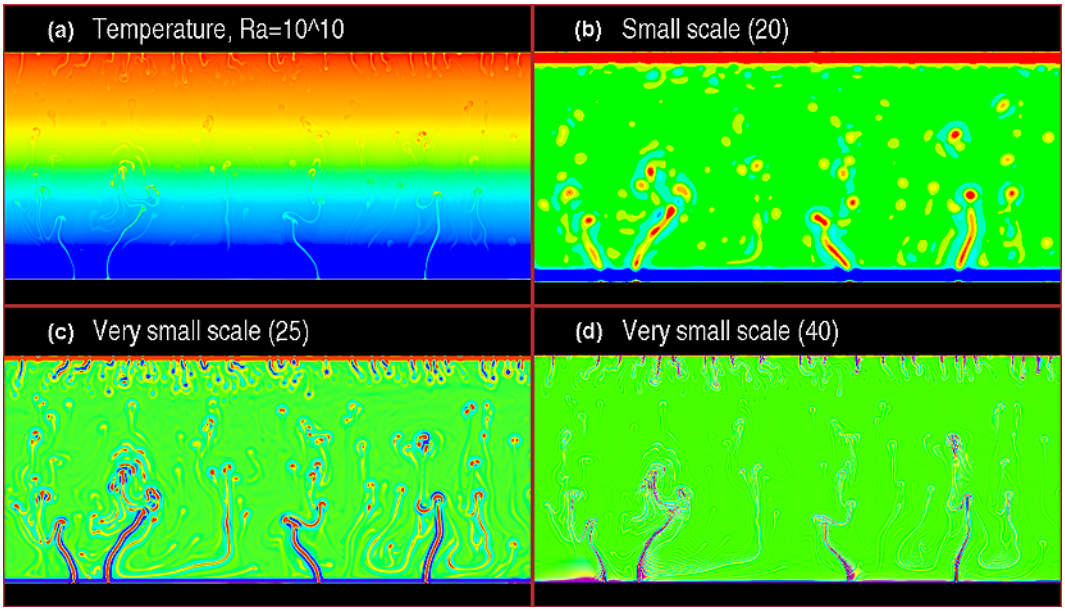

Figure 4.31. Enlargement of temperature deviation for $Ra = 10^{10}$. Colorscale same as Figure 4.28. (a) Enlargement of original temperature deviation dataset. (b-d) Enlargement of scalogram slices for three modes. Resolution of modes given in Table 4.1; modes for each slice in parentheses.

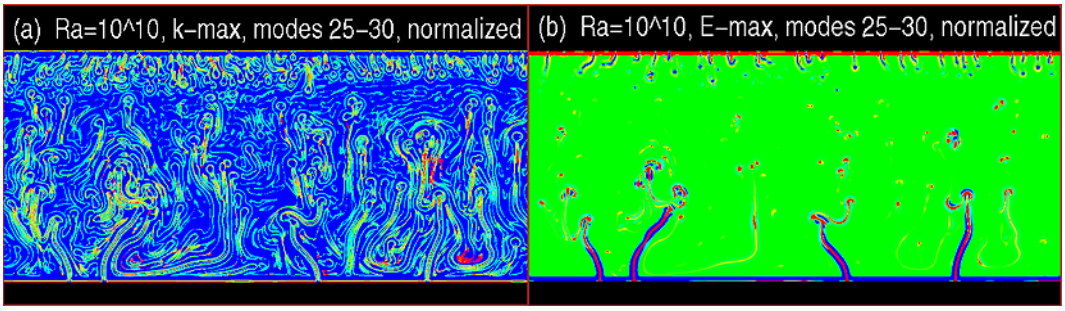

Figure 4.32. Enlargement of $E_{\max}/k_{\max}$ maps for temperature deviation for $Ra = 10^{10}$ using modes 25-30. Resolution of modes in Table 4.1. Colorscale same as Figure 4.29. (a) Enlargement of $k_{\max}$ map. (b) Enlargement of $E_{\max}$ map.

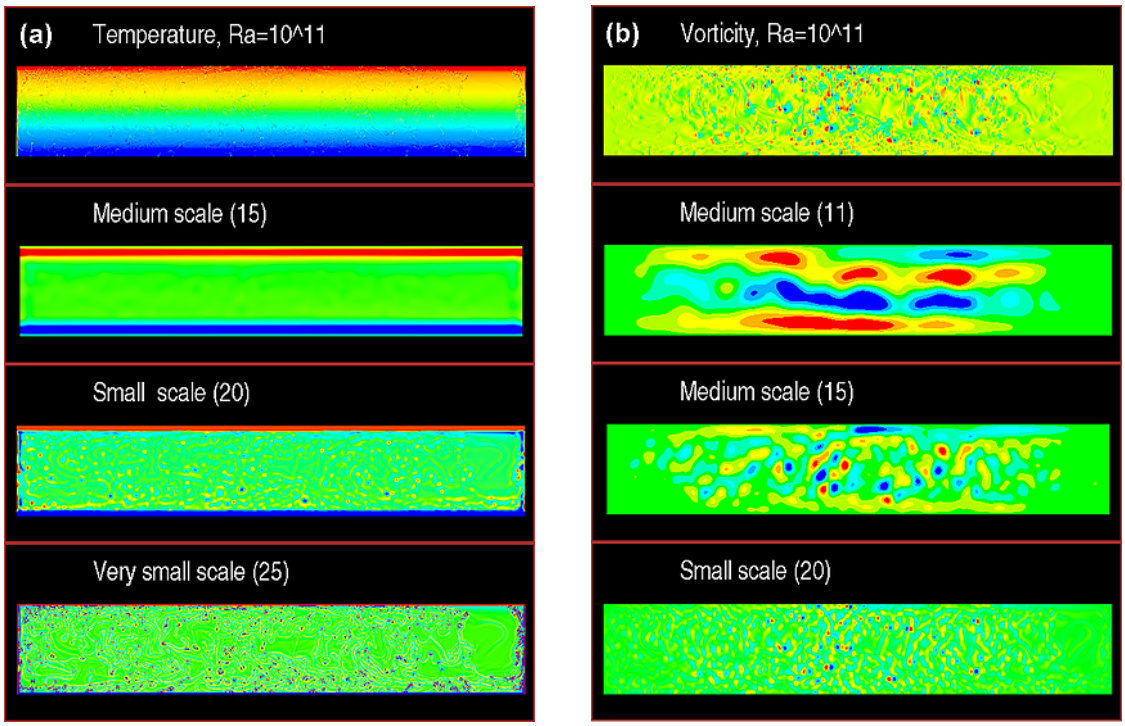

Figure 4.33. Temperature deviation and vorticity field for $Ra = 10^{11}$. Top slices are original datasets for each panel. Other slices show scalograms through three wavelet modes. Colorscale same as Figure 4.28. Resolution of the modes given in Table 4.1; modes for each slice in parentheses.

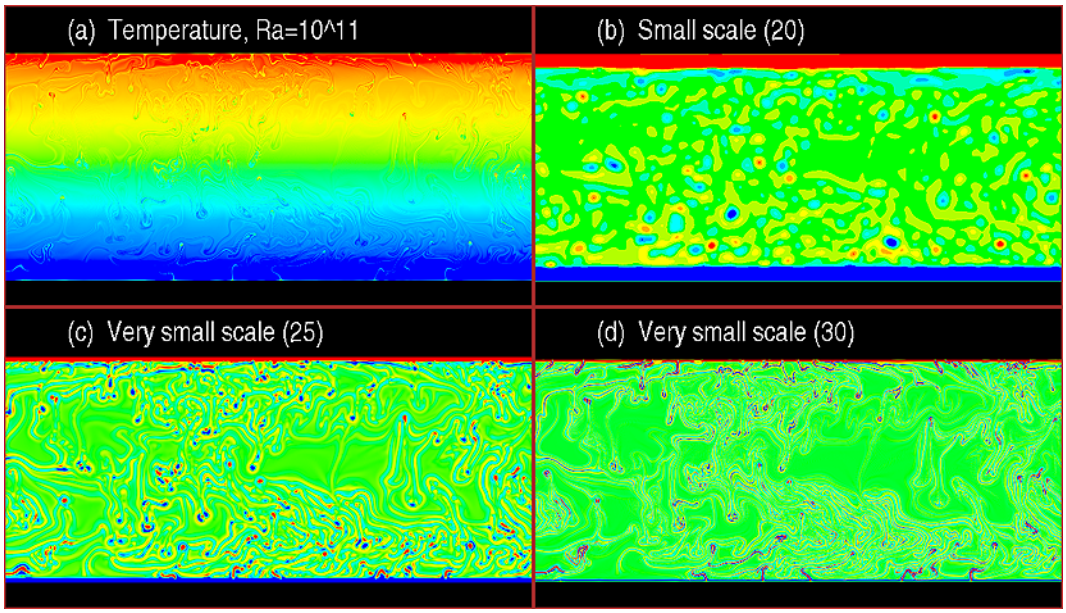

Figure 4.34. Enlargement of temperature deviation for $Ra = 10^{11}$. Colorscale same as Figure 4.28. (a) Enlargement of original temperature deviation dataset. (b-d) Enlargement of scalogram slices for three modes. Resolution of modes given in Table 4.1; modes for each slice in parentheses.

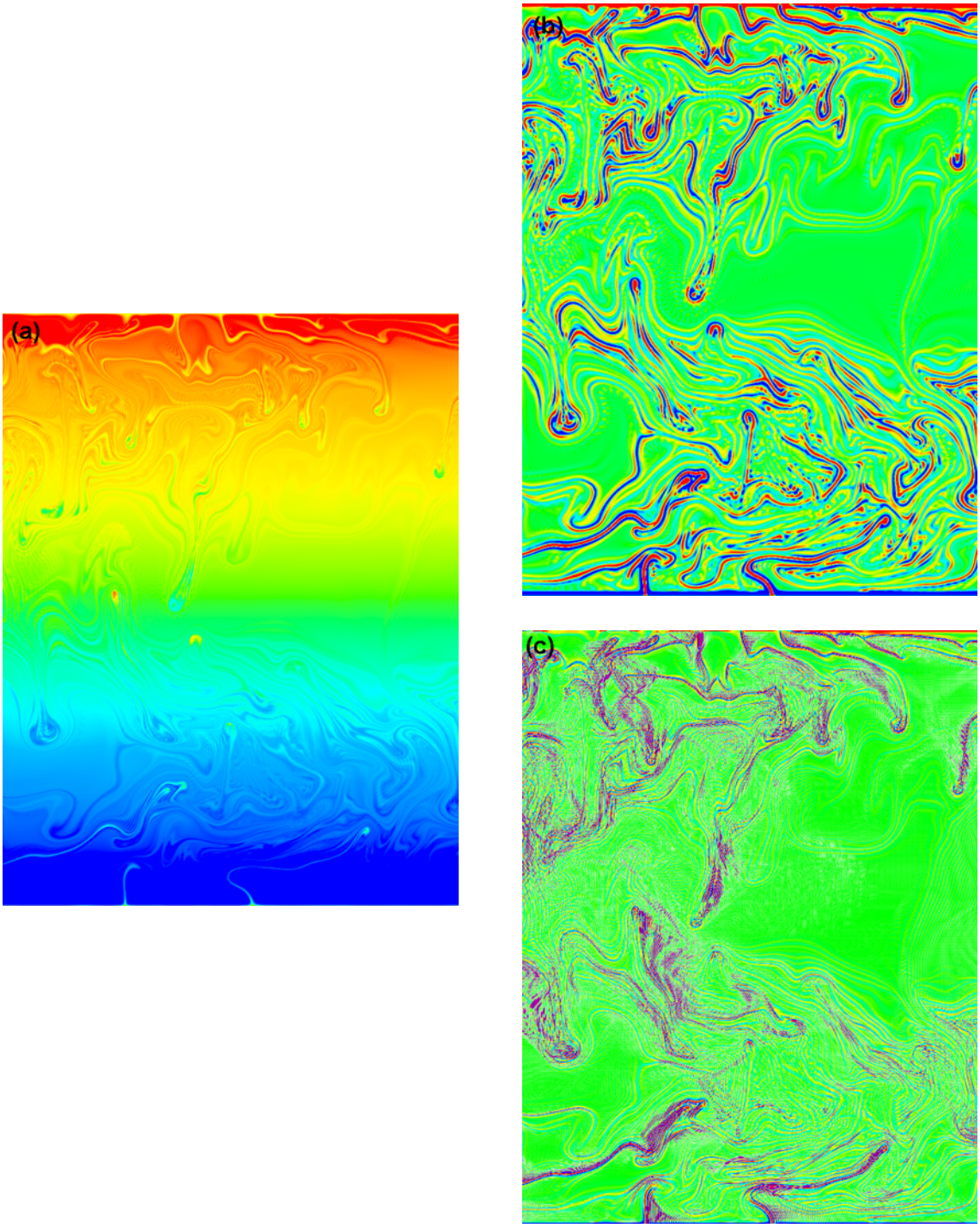

Figure 4.35. Enlargement of temperature deviation for $Ra = 10^{11}$. Colorscale same as Figure 4.28. (a) Enlargement of original temperature deviation field. (b-c) Enlargement of scalogram slices for two modes. Resolution of modes given in Table 4.1. (b) Mode 30. (c) Mode 40.

Chapter 5

Conclusions

Two main areas of research were covered by this study: application of the continuous wavelet transform to geophysical fields and study of the nonlinear system arising from thermal convection. The first area of our research (Chapter 3) was focused on the modelling of mantle convection with special emphasis on different regimes which can occur with increasing Rayleigh number (Ra), which was the only control parameter of the model. Tools from deterministic chaos theory were used to help quantify the convection regimes. As the different topics were treated in the preceding chapters, each section includes its own concluding remarks. The purpose of this chapter is to summarize the results in a clear way.

In the second area of the research, the aim of our study was to prepare continuous wavelet transforms for the time-frequency analysis of 1-D signals and for the detection of the spatial structure of 2-D geophysical fields (Chapter 2). It was followed by the application of capability, power and efficiency of the wavelets to the time-series from the thermal convection model (Chapter 3) and to the 2-D fields from the three different geophysical areas: the geoid, mixed mediums, and thermal convection (Chapter 4).

5.1 Thermal convection modelling

Numerical studies of the nonlinear system, which represents the thermal convection in classical Boussinesq approximation for infinite Prandtl number and for axisymmetrical geometry, resulted in the following conclusions :

- the convection systems for the examined interval of Rayleigh numbers $Ra = 1.7 \cdot 10^4 - 10^{11}$ can be classified into four basic regimes: the convection of low Rayleigh numbers (for Ra varying from $1.7 \cdot 10^4$ to 10^5) reaches simple attractors (steady or periodic ones); intermediate Ra convection ($Ra = 10^5 - 10^6$) still has two-cell convection structure, but secondary plumes appear; high Ra runs with Ra between 10^6 and 10^{10} exhibit complex structure with waning large-scale motion and prevailing plume interactions; finally, ultra-high Ra convection (10^{10} and more) embodies very turbulent behavior with powerful mixing;
- the low-Ra runs started from the two different initial states, tangential symmetrical and

asymmetrical ones, and finished in different steady regimes. The convection, which started from the symmetrical state, preserved symmetry for the whole computed time; in the case of higher Rayleigh numbers the symmetry was broken due to the computational errors;

- the $Ra = 1.7 \cdot 10^4$ run finished in steady regimes, a four-cell one for the symmetrical initial temperature and a two-cell one for the asymmetrical one; the run with symmetry broken by a small perturbation takes a very long time (relatively to the original run) to reach a new attractor; the approach to the new attractor occurred through two sudden changes of the system regimes;

- the symmetrical $Ra = 10^5$ run stays in a periodic attractor with two convection cells, the asymmetrical $Ra = 10^5$ run introduces a new kind of convection system: large and small convection cells together with secondary plumes rising in the large cell;

- the correlation dimension computed from the kinetic energy and Nusselt number time-series for $Ra = 10^5$, asymmetrical state, reveals complex temporal evolution of the system but is simple in physical space; the value of the dimension was determined to be approximately 13-15;

- the wavelet spectrum of the global kinetic energy ($Ra = 10^5$, asym.) is concentrated in two bands of periods, while the semi-global Nusselt number shows only one period band; the similarity of the structure in the band belonging to the surface Nusselt number and in the long-period band in the kinetic energy spectrum suggests that this band is caused by the changes in large-scale motion of the two cells; the small-period band in the kinetic energy wavelet spectrum is a product of the secondary plume evolution;

- intermediate-Ra runs remain in two-cell convection with secondary plumes in both cells; the wavelet spectra of the kinetic energy and the Nusselt number preserve the band-structure but the energy is shifted from the cell-convection (large periods) to plume-convection (small periods);

- high-Ra convection increases the number of convective cells, the 2-D wavelet analysis of the vorticity revealed two cells for $Ra = 10^6$, three cells for $Ra = 10^7$ and about five cells for $Ra = 10^8$;

- plume-convection prevails over former cell-convection in high-Ra runs, the area where these two regimes are balanced seems to be in the interval $Ra = 10^6 - 10^7$; in this interval of Rayleigh numbers, there is also the highest relative deviations of the kinetic energy and the Nusselt number values; moreover, this interval corresponds to the estimated Ra for the whole-mantle convection in the real Earth;

- the number of whole-mantle plumes remains relatively small (3-5) in high-Ra convection, the plumes remain stable for longer times even in the case of such high Rayleigh number as $Ra = 10^8$;

- strong plume evolution leads to the development of Whitehead instabilities; the development occurs under conditions of whole-mantle plumes that collide; we found an interval $10^7 - 10^9$ of the Rayleigh numbers which satisfy this condition;

- a significant change of behavior arose for $Ra = 10^{10}$ convection; the mixing is so powerful that plumes are not able to grow through the whole mantle; the 2-D wavelet spectrum of the vorticity reveals layered convection;
- power laws of the kinetic energy and the Nusselt number exist for all considered values of Ra, only the kinetic energy for $Ra = 10^{10}$ exhibits a smaller value than the expected one, which can be related to a significant change of the convection regime; the exponents in the power laws agree with those found by Christensen (1989) and Jarvis and Peltier (1982) for the convection model in the Cartesian geometry.

5.2 The power of wavelet analysis

Our experience with the application of the continuous wavelet transform (CWT) in different problems can be summarized as follows :

- the CWT proved to be a user-friendly and unpretentious tool, which allows one to search an analyzed signal in all frequencies at the same time;
- although there exists a lot of miscellaneous kinds of wavelet basis functions, features, which one can demand from the wavelet transform are well described, and they easily lead to a choice of an appropriate wavelet function; we selected the Morlet wavelet (2.9) for time-frequency analysis of 1-D signals and the isotropic 2-D Mexican-hat wavelet (2.14) for the detection of spatial structure in 2-D fields;
- we have used only the power of the wavelet spectra for visualization of the wavelet spectra (in the form of scalograms) - phase diagrams of the (generally) complex wavelet spectrum were not found to be helpful;
- the signed wavelet power (2.18) of the wavelet spectrum helps to distinguish negative and positive signs of the anomalies; while the (classical) unsigned power (2.17) can help to reveal the spatial structure of the analyzed field;
- the 2-D isotropic wavelet transform is a suitable reduction of the general definition of the 2-D CWT in cases where the polarization of the anisotropic structures need not be determined;
- large-scale analysis of the edge layers is affected by a periodic extension of the field during the FFT computation; we solve the problem by enlarging the original field with sufficiently thick zero layers;
- the graphical visualization of the results from the 2-D and higher dimensional wavelet analysis seems to be a serious problem in wavelet analysis; in the 2-D case, we found that the 2-D snapshots for several scales are the best solution - the whole wavelet spectrum is roughly surveyed, and the peripheral property of the wavelet transform related to the nature of the wavelets together with the isotropic approximation can signalize interesting features in not-visualized scales;
- the new method of $E_{\max}/k_{\max}$ maps can increase the detection ability of the wavelets in small-scale wavelet prospecting;

- the power of the 2-D wavelet transform was demonstrated on the analysis of the non-hydrostatic geoid with a resolution of 4 degrees; as the geoid large-scale structure was easily detectable right from the field and only small-scale structures needed to be revealed, the Mercator projection of the geoid followed by the 2-D Cartesian wavelet transform proved to be a better solution than the use of the spherical wavelet transform, whose computation is still complicated;

- small-scale wavelet spectrum of the geoid revealed features caused by lithospheric processes; the strongest signal originated from subduction zones (e.g., the "Ring of Fire"); weaker signals were detected along several mountain belts (the Himalayas, the Andes, and the Atlas Mts.), oceanic rifts (the Mid-Atlantic Ridge) and hotspots (Hawaii);

- $E_{\max}/k_{\max}$ maps are able to detect (at least to some extent) the plate pattern history of the Earth;

- the wavelet analysis of the mixed field helps to monitor mixing progress; we took advantage of the sensitivity of the isotropic wavelet transform to unmixed anisotropic structures in the field to detect the degree of the mixing;

- the time evolution of the global wavelet spectra (analogous to the Fourier spectra) revealed end points of rough mixed states of the medium on given scales; determination of well mixed states is more difficult due to the attracting large-scale motion of the system;

- the time similarity (the same scale and close timesteps) and the scale similarity (close scales in the same time) of the (local) wavelet spectra enables us to estimate well mixed states more precisely;

- the 2-D wavelet transform applied to the temperature and vorticity fields originated from the thermal convection model proved its ability for both small-scale and large-scale detection; small-scale wavelet analysis of the temperature revealed the complex structure of plumes in the ultra-high Ra convection; moreover, it helped to find areas of numerical instabilities. Large-scale analysis of the vorticity determined the number of convection cells;

- $E_{\max}/k_{\max}$ maps uncover not only plumes, but also their remains. In the case of layered convection for ultra-high Rayleigh number $Ra = 10^{10}$ the remains of plumes revealed by the $k_{\max}$ indicate a small-cell structure of this turbulent convection.

References

Antoine, J.P., Carrette, P., Murenzi, R. and B. Piette, Image analysis with two-dimensional continuous wavelet transform, *Signal Processing*, **31**, 241–272, 1993.

Antoine, J.P. and P. Vandergheynst, Wavelets on the n-sphere and related manifolds, *J. Math. Phys.*, **39**, 3987–4008, 1998.

Auger, F. and P. Flandrin, Improving the readability of time-frequency and time-scale representations by the reassignment method, *IEEE Trans. Signal Proc.*, **43 (5)**, 1068–1089, 1995.

Babuška, V., Plomerová, J. and M. Garnet, The deep lithosphere of the Alps: a model inferred from P residuals, *Tectonophysics*, **176**, 137–165, 1990.

Barriot, J.P., Vals, N., Balmino, G. and P. Rosenblatt, A 180th degree and order model of the Venus gravity field from Magellan line of sight residual Doppler data, *Geophys. Res. Lett.*, **25**, 3743–3746, 1998.

Bergeron, S.Y., Vincent, A.P., Yuen, D.A., Tranchant, B.J.S. and C. Tchong, Viewing seismic velocity anomalies with 3-D continuous Gaussian wavelets, *Geophys. Res. Lett.*, **26 (15)**, 2311–2314, 1999.

Bergeron, S.Y., Yuen, D.A. and A.P. Vincent, Looking at the inside of the Earth with 3-D wavelets: A pair of new glasses for geoscientists, *Electronic Geosciences, (2000) 5:3*, edited by J.D. Clements, Springer-Verlag, Heidelberg, Germany, 2000a.

Bergeron, S.Y., Yuen, D.A. and A.P. Vincent, Capabilities of 3-D wavelet transforms to detect plume-like structures from seismic tomography, *Geoph. Res. Lett.*, **27 (20)**, 3433–3436, 2000b.

Bijwaard, H. and W. Spakman, Tomographic evidence for a narrow whole mantle plume below Iceland, *Earth Planet Sci. Lett.*, **166**, 121–126, 1999.

Boehler, R., Chopelas, A. and A. Zerr, Temperature and chemistry of the core-mantle boundary, *Chemical Geology*, **120**, 199–205, 1995.

Čadek, O., Kývalová, H. and D.A. Yuen, Geodynamical implications from the correlation of surface geology and seismic tomographic structure, *Earth Planet. Sci. Lett.*, **136**, 615–627, 1995.

Čadek, O. and L. Fleitout, A global geoid model with imposed plate velocities and partial layering, *J. Geophys. Res.*, **104 (B12)**, 29,055–29,075, 1999.

Calmant, S. and A. Cazenave, Anomalous elastic thickness of the oceanic lithosphere in the south-central Pacific, *Nature*, **328**, 236–238, 1987.

Cannon, W.F., The Midcontinent rift in the Lake-Superior region with emphasis on its geodynamics evolution, *Tectonophysics*, **213**, 41–48, 1992.

Cartwright, M., *Fourier Methods for Mathematics, Scientists and Engineers*, Ellis Horwood, England, 1990.

Cazenave, A., Souriau, A. and K. Dominh, Global coupling of Earth surface topography with hotspots, geoid and mantle heterogeneities, *Nature*, **340**, 54–57, 1989.

Chandrasekhar S., *Hydrodynamic and Hydromagnetic Stability*, Clarendon Press, Oxford, 1961.

Chang, H.R. and H.N. Shirer, Transitions in shallow convection: An explanation for lateral cell expansion, *J. Atmos. Sci.*, **41**, 2334–2346, 1984.

Chase, C.G., Subduction, the geoid, and lower mantle convection, *Nature*, **282**, 464–468, 1979.

Christensen, U.R., Heat transport by variable viscosity convection and implications for the Earth's thermal convection, *Phys. Earth Planet. Int.*, **35**, 264–282, 1984.

Christensen, U.R., Heat transport by variable viscosity convection II: Pressure influence, non-Newtonian rheology and decaying heat sources, *Phys. Earth Planet. Int.*, **37**, 183–205, 1985.

Christensen, U.R., Mantle rheology, constitution, and convection in *Mantle Convection, Plate Tectonics and Global Dynamics*, ed. by W.R. Peltier, Gordon and Breach Science Publishers, 595–656, 1989.

Chu, T.Y. and R.J. Goldstein, Turbulent convection in a horizontal layer of water, *J. Fluid Mech.*, **60**, 141–150, 1973.

Claasen T.A.C.M. and W.F.G. Mecklenbräuker, The Wigner distribution, a tool for time-frequency analysis, Part I: Continuous-time signals, **35 (3)**, 217–250, Part II: Discrete-time signals, **30 (4/5)**, 276–300, Part III: Relations with other time-frequency signal transformations, **35 (6)**, 372–389, *Philips J. Res.*, 1980.

Cohen, L., Generalized phase space distribution functions, *J. Math. Phys.*, **7 (5)**, 781–786, 1966.

Cohen, L., Time-frequency distribution—A review, *Proc. IEEE*, **77**, 941–981, 1989.

Crough, S.T. and D.M. Jurdy, Subducted lithosphere, hotspots and the geoid, *Earth Planet. Sci. Lett.*, **48**, 1980.

Daubechies, I., *Ten Lectures on Wavelets*, SIAM, Phila, PA, 1992.

Drazin, P.G., *Nonlinear Systems*, Cambridge Univ. Press, 233–276, 1992.

Dritschel, D.G., Contour dynamics and contour surgery: numerical algorithms for extended, high-resolution modelling of vortex dynamics in two-dimensional, inviscid, incompressible flows, *Computer Phys. Res.*, **10**, 77–146, 1989.

ETOPO5, Data Announcement 88-MGG-02, Digital relief of the Surface of the Earth, *http://edcwww.cr.usgs.gov/glis/hyper/guide/etopo5*, NOAA, National Geophysical Data Center, Boulder, Colorado, 1988.

Farge, M., Wavelet transforms and their applications to turbulence, *Annu. Rev. Fluid Mech.*, **24**, 395–457, 1992.

Fornberg, B., *A practical Guide to Pseudospectral Methods*, Cambridge Univ. Press, 1996.

Forte, A.M. and J.X. Mitrovica, New inferences of mantle viscosity from joint inversion of long-wavelength mantle convection and post-glacial rebound data, *Geophys. Res. Lett.*, **23**, 1147–1150, 1996.

Fytikas, M.D. and N.P. Kolios, Preliminary heat flow map of Greece, from *Terrestrial Heat Flow in Europe*, Čermák, V. and L. Rybach eds., 1979.

Goes, S., Spakman, W. and H. Bijwaard, A lower mantle source for central European volcanism, *Science*, **286**, 1928–1931, 1999.

Hager, B.H., Global isostatic geoid anomalies for plate and boundary layer models of the lithosphere, *Earth Planet. Sci. Lett.*, **63**, 97–109, 1983.

Hager, B.H., Subducted slabs and the geoid: Constraints on mantle rheology and flow, *J. Geophys. Res.*, **89**, 6003–6016, 1984.

Hansen, U., Yuen, D.A., Kroening, S.E. and T.B. Larsen, Dynamical consequences of depth-dependent thermal expansivity and viscosity on mantle circulations and thermal structure, *Phys. Earth Planet. Inter.*, **77**, 205–223, 1993.

Hofmeister, A.M., Mantle values of thermal conductivity and the geotherm from phonon lifetimes, *Science*, **283**, 1699–1706, 1999.

Holschneider, M., Continuous wavelet transforms on the sphere, *J. Math. Phys.*, **37**, 4156–4165, 1996.

Hubbard, B.B, *The World According to Wavelets*, A K Peters Wellesley, Massachusetts, 1998.

Jarvis, G.T. and W.R. Peltier, Mantle convection as a boundary layer phenomenon, *Geophys. J. R. Astr. Soc.*, **68**, 389–427, 1982.

Jarvis, G.T. and W.R. Peltier, Convection models and geophysical observations in *Mantle Convection, Plate Tectonics and Global Dynamics*, ed. by W.R. Peltier, Gordon and Breach Science Publishers, 479–594, 1989.

Kaiser, G., *A Friendly Guide to Wavelets*, Birkhäuser, 1994.

Karato, S.I., Rheology of the upper mantle: A synthesis, *Science*, **260**, 771–778, 1993.

Kido, M. and O. Čadek, Inferences of viscosity from the oceanic geoid: Indication of a low viscosity zone below the 660-km discontinuity, *Earth Planet. Sci. Lett.*, **151**, 125–138, 1997.

King, S.D., Radial models of mantle viscosity: results from a genetic algorithm, *Geophys. J. Int.*, **122**, 982–990, 1995.

Kissling, E., Deep structure of the Alps–What do we really know? *Phys. Earth Planet. Inter.*, **79**, 87–112, 1993.

Larsen T.B., Yuen, D.A., Moser, J. and B. Fornberg, A high-order finite-difference method applied to large Rayleigh number mantle convection, *Geophys. Astrophys. Fluid Dyn.*, **84**, 53–83, 1997.

Le Stunff, Y. and Y. Ricard, Topography and geoid due to lithospheric mass anomalies, *Geophys. J. Int.*, **122**, 982–990, 1995.

Li, Q. and E. Nyland, Is the dynamics of the lithosphere chaotic? in *Nonlinear Dynamics and Predictability of Geophysical Phenomena*, Geophysical Monograph 83 and IUGG, **18**, W.I. Newman, A. Gabrielov and D.L. Turcotte eds., AGU, 37–42, 1994.

Li, T.H., Multiscale representation and analysis of spherical data by spherical wavelets, *SIAM, J. Sci. Comput.*, **21 (3)**, 924–953, 1999.

Lorenz, E.N., Deterministic nonperiodic flow, *J. Atmos. Sci.*, **20**, 130–141, 1963.

Malevsky, A.V. and D.A. Yuen, Characteristics-based methods applied to infinite Prandtl number thermal convection in the hard turbulent regime, *Phys. Fluids*, **9 (A3)**, 2105–2115, 1991.

Marek, M. and I. Schreiber, *Chaotic Behaviour of Deterministic Dissipative Systems*, Academia, Praha, 1991.

Margenau H. and R.N. Hill, Correlation between measurements in quantum theory, *Prog. Theor. Phys.*, **26**, 772–738, 1961.

Matyska, C., Moser, J. and D.A. Yuen, The potential influence of radiative heat transfer on the formation of megaplumes in the lower mantle, *Earth Planet. Sci. Lett.*, **125**, 255–266, 1994.

Meyers, S.D., Kelly, B.G. and J.J. O'Brien, An introduction to wavelet analysis in oceanography and meteorology: With application to the dispersion of Yanai waves, *Mon. Wea. Rev.*, **121**, 2858–2866, 1993.

Morlet, J., Sampling theory and wave propagation in *Issues on Acoustic Signal/Image Processing and Recognition*, ed. by C.H. Chen, Berlin Springer, 1983.

Moser, J., *Mantle Dynamics and Rotation of the Earth*, Ph.D. thesis, Charles University, Prague, 1994.

Murphy, M.S., Vecsey, L., Sevre, E.O. and D.A. Yuen, Secondary upwelling instabilities developed in high Rayleigh number convection: Possible applications to hot spots, *Electronic Geosciences*, **5**, Springer Berlin Heidelberg, 2000.

Newhouse, S., Ruelle, D. and F. Takens, Occurence of strange axiom - a attractors near quasi-periodic flows on T^m, $m \geq 3$, *Commun. Math. Phys.*, **64**, 35–40, 1978.

Nese, J.M., Diagnosing the structure of attractors in *Nonlinear Hydrodynamic Modeling: A Mathematical Introduction*, ed. by H.N. Shirer, Springer-Verlag, 422–424, 1987.

Oldenburg, C.M., Spera, F.J., Yuen, D.A. and G. Sewell, Dynamic mixing in magma bodies: theory, simulations and implications, *J. Geophys. Res.*, **94**, 9215–9236, 1989.

Ottino, J.M., *The Kinematics of Mixing: Stretching, Chaos, and Transport*, Cambridge texts in Applied Mathematics-Ser. No. 4, Cambridge University Press, New York, p. 375, 1989.

Piromallo, C., Vincent, A.P., Yuen D.A. and A. Morelli, Dynamics of the transition zone under Europe inferred from wavelet cross-spectra of seismic tomography, *Phys. Earth Planet. Inter.*, **125**, 125–139, 2001.

Raidl, A., *Determinism, Contingency and Predictability of Atmospheric Processes*, Ph.D. Thesis, Charles University, Prague, 1995 (in czech).

Rapp, R.H. and N.K. Paulis, The development and analysis of geopotential coefficient models to spheric harmonic degree 360, *J. Geophys. Res.*, **95**, 21885–21911, 1990.

Ricard, Y., Fleitout, L. and C. Froidevaux, Geoid heights and lithospheric stresses for a dynamic earth, *Ann. Geophys.*, **2**, 267–286, 1984.

Rossby, H.T., A study of Bénard convection with and without rotation, *J. Fluid Mech.*, **36**, 309–335, 1969.

Ruelle, D. and F. Takens, On the nature of turbulence, *Commun. Math. Phys.*, **20**, 167–192, 1971.

Sabadini, R., Doglioni, C. and D.A. Yuen, Eurstatic sea level fluctuations induced by polar wander, *Nature*, **345**, 708–710, 1990.

Sandwell, D.T. and W.H.F. Smith, Marine gravity from the Geostat and ERS-1 altimetry, *J. Geophys. Res.*, **102**, 10039–10054, 1997.

Schmalzl, J., Houseman, G.A. and U. Hansen, Mixing in vigorous, time-dependent three-dimensional convection and application to Earth's mantle, *J. Geophys. Res.*, **101**, 21,847–21,858, 1996.

Schott, B. and H. Schmeling, Delamination and detachment of a litospheric root, *Tectonophysics*, **296**, 225–247, 1998.

Simons, M., Solomon, S.C. and B.H. Hager, Localization of gravity and topography: constraints on the tectonics and mantle dynamics of Venus, *Geophys. J. Int.*, **131**, 24–44, 1997.

Simons, M. and B.H. Hager, Localization of the gravity field and the signature of glacial rebound, *Nature*, **390**, 500–504, 1997.

Skilbeck, J.N. and J.A. Whitehead, Formation of discrete islands in linear chains, *Nature*, **272**, 499–501, 1978.

Sommerscales, E.F.C. and I.W. Gazda, Thermal convection in high Prandtl number liquids at high Rayleigh numbers, *Int. J. Heat Mass Trans.*, **12**, 1491–1511, 1969.

Stewart C.A. and D.L. Turcotte, The route to chaos in thermal convection at infinite Prandtl number: 1. Some trajectories and bifurcations, *J. Geoph. Research*, **94 (B10)**, 13707–13717, 1989.

Tackley, P.J., Stevenson, D.J., Glatzmeier, G.A. and G. Schubert, Effects of an endothermic phase transition at 670 km depth on mantle convection, *Nature*, **361**, 699–704, 1993.

Ten, A., Yuen, D.A., Larsen, T.B. and A.V. Malevsky, The evolution of material surfaces in convection with variable viscosity as monitored by a characteristics-based method, *Geoph. Res. Lett.*, **23**, 2001–2004, 1996.

Ten, A., Yuen, D.A., Podladchikov, Yu.Yu., Larsen, T.B., Pachepsky, E. and A.V. Malevsky, Fractal features in mixing of non-Newtonian and Newtonian mantle convection, *Earth Planet. Sci. Lett.*, **146**, 401–414, 1997.

Ten, A., Podladchikov, Yu.Yu., Yuen, D.A., Larsen, T.B. and A.V. Malevsky, Comparision of mixing properties in convection with the particle-line method, *Geoph. Res. Lett.*, **25 (16)**, 3205–3208, 1998.

Theiler, J., Estimating fractal dimension, *J. Opt. Soc. Am. A.*, **7**, 1055–1073, 1990.

Torrence, Ch. and G.P. Compo, A practical guide to wavelet analysis, *Bull. Am. Meteorol. Soc.*, **79**, 61–78, 1998

Torresani, B., Position-frequency analysis for signals defined on spheres, *Signal Processing*, **43**, 341–346, 1995.

Turcotte, D.L. and G. Schubert, *Geodynamics: Applications of Continuum Physics to Geological Problems*, 450 pp., J. Wiley and Sons, New York, 1982.

Turcotte, D.L., *Fractals and Chaos in Geology and Geophysics*, Cambridge University Press, Cambridge, 1992.

Van den Berg, A.P., van Keken, P.E. and D.A. Yuen, The effects of a composite non-Newtonian and Newtonian rheology on mantle convection, *Geophys. J. Int.*, **115**, 62–78, 1993.

Van den Berg, J.C. (Ed.), *Wavelets in Physics*, Cambridge University Press, Cambridge, 1999.

Vecsey, L. and C. Matyska, Wavelet spectra and chaos in thermal convection modelling, *Geophys. Res. Lett.*, **28 (2)**, 395–398, 2001.

Velímský, J. and C. Matyska, The influence of adiabatic heating/cooling on magnetohydrodynamic systems, *Phys. Earth Planet. Inter.*, **117**, 197–207, 2000.

Vincent, A.P. and D.A. Yuen, Thermal attractor in chaotic convection with high-Prandtl-number fluids, *Phys. Rev. A.*, **38**, 328–334, 1989.

Vincent, A.P. and D.A. Yuen, Transition to turbulent thermal convection beyond Ra=10**10 detected in numerical simulations, *Phys. Rev. E.* **61 (5)**, 5241–5247, 2000.

Whitehead, J.A., Instabilities of fluid conduits in a flowing earth – are plates lubricated by the asthenosphere?, *Geophys. J. R. Astron. Soc.*, **70**, 415–433, 1982.

Wigner, E.P., On the quantum correction for thermodynamic equilibrium, *Phys. Rev.*, **40**, 749–759, 1932.

Yegorova, T.P., Starostenko, V.I. and V.G. Kozlenko, Large-scale 3-D gravity analysis of the inhomogeneities in the European-Mediterranean upper mantle, *Pure and Applied Geophysics*, **151**, 549–561, 1998.

Yuen, D.A., ed., *Chaotic Processes in the Geological Sciences*, Springer-Verlag, New York, 1992.